Anderson Localization of Light

Dissertation

zur Erlangung des akademischen Grades
Doktor der Naturwissenschaften (*Dr. rer. nat.*)

an der Universität Konstanz,
Mathematisch-Naturwissenschaftliche Sektion,
Fachbereich Physik,

vorgelegt von

Martin Störzer

Referenten:

Prof. Dr. Georg Maret
PD Dr. Holger Stark
Tag der mündlichen Prüfung:

17. November 2006

Contents

1 Introduction **5**

2 Theory **9**
- 2.1 Single Scattering 10
  - 2.1.1 Rayleigh Scattering 11
  - 2.1.2 Mie Scattering 13
- 2.2 The Structure Factor 14
- 2.3 Random Walk and Photon Diffusion 15
  - 2.3.1 Slab Geometry 18
- 2.4 Coherent Backscattering 22
- 2.5 Anderson Localization 28
- 2.6 Faraday Effect 32
  - 2.6.1 Faraday Effect and the Principle of Reciprocity 34
  - 2.6.2 Faraday Effect in Multiple Scattering 35

3 Experimental Setup **37**
- 3.1 Coherent Backscattering 38
  - 3.1.1 The Mechanical and Electronic Setup 40
  - 3.1.2 The Optical Setup 41
  - 3.1.3 Small Angle Coherent Backscattering 42
  - 3.1.4 Calibration and Measurement 43
- 3.2 Time Resolved Transmission 46
  - 3.2.1 The Optical Setup 46
- 3.3 Time Resolved Transmission Inside a Magnetic Field 49

4 Multiple Scattering Samples **53**
- 4.1 The Transport Mean Free Path 54
- 4.2 The Effective Refractive Index 55
  - 4.2.1 Garnett Effective Refractive Index 55
  - 4.2.2 Numerical Simulation 57
- 4.3 Sample Characterization Techniques 58
  - 4.3.1 Single Scattering Techniques 59
  - 4.3.2 Electron Microscope Imaging 61
- 4.4 Commercial Samples 63

4.5 Custom Made Samples 65
4.5.1 Titania Full-Spheres 65
4.5.2 Core-Shell Particles 68

5 Experimental Results **69**
5.1 Resonance Scattering 70
5.2 Nonclassical Diffusion 74
5.2.1 Time Resolved Transmission Measurements 75
5.2.2 Determination of the Critical Exponents 81
5.2.3 Static Transmission 86
5.3 Faraday Effect 86
5.3.1 The Faraday Active Multiple Scattering Sample 87
5.3.2 Time resolved Transmission Measurements on Faraday-Active Multiple Scattering Samples 88

6 Summary and Outlook **93**

7 Zusammenfassung und Ausblick **95**

8 List of Publication **97**

9 Danksagung **99**

Chapter 1

Introduction

The whole world we are living in is in current motion. In almost every system an exchange of energy or matter takes place. This exchange is only possible if there is a mechanism of transport. Life for example would not be possible without nutrients reaching the organism and excrements leaving it. Because this transport plays such an important role, one is interested to understand how nature solves this problem in order to use it for its purposes. Due to the huge number of different ways on which transport takes place, not just biological transport-phenomena are very complicated. Light from the sun for example needs a very long time, a few million years in fact, for a distance of 0.7 million kilometers to reach the surface of the sun, from where it takes just eight minutes to reach the earth, which is 150 million kilometers away. This is obviously due to the different transport mechanisms for photons passing through the sun and the interplanetary space respectively.

When there is no direction to the mechanism of transport in contrast to e.g. ballistic motion, the easiest model is elastic scattering of particles through a disordered system. Here a particle enters a random medium and interacts with the scatterers in a way that they are able to change just the direction of the particle. This is one of the most common mechanisms of transport on a slow time scale, e.g. in chemical reactions or biological development.

Here we will be concerned with photons inside a medium with a random fluctuations of the refractive index. The behavior of photons traveling through such a multiple scattering medium can be described as a diffusion process, which is a concept that holds for transport through every multiple scattering system. Transport that relies on diffusion leads to a transmission inversely proportional to the length of the medium known in the context of electrons in metals as Ohm's law.

Although the quantification of scattering properties for a single scatterer is a complicated theoretical problem, those properties seem to loose their importance in the limit of multiple scattering. This can be understood because photons travel through the medium on different trajectories. Considering a large number of trajectories is analogous to an average over all single scattering properties.

To this point there is no need to deal with the wave nature of light, which is expected to change the transport properties. It is surprising that the diffusion theory still allows a theoretical description of photon transport. Due to the different trajectories through the system, the phase-relation is changed but it is still not expected, that this should affect the transport properties of the system. Since the different paths are randomly distributed, one expects a random phase-relation, which, for a coherent light source, leads to a granular intensity distribution. This intensity distribution is known as speckle pattern. Averaging over all possible trajectories the speckle-pattern washes out, making it clear that the transport still follows diffusion theory leading to Ohm's law.

But this is not the whole truth, since there is one class of paths, which do not loose the phase-relation due to a trajectory average. Those are the paths, where photons are able to travel along time reversed trajectories as well. It is obvious that those paths are always in phase and that therefore photons which travel on time reversed paths always show constructive interference. This leads to an intensity which is enhanced at all positions of such a closed loop. Therefore the effect is expected to influence the amount of photons, which are transmitted through the medium. In a semi-infinite geometry it is expected that this effect can be observed by an enhancement of the intensity reflected into the direction of the illumination. The existence of this interference effect, known as coherent backscattering was shown in 1985 [1, 2]. In a finite system constructive interference on reciprocal paths is expected to lead to a small correction in transmission, known as weak localization. For an increasing amount of disorder it is expected that there is the possibility that one point of a closed loop is the origin of a second closed loop, which again contributes to another loop and so on. For a diverging sample-size, diffusion comes to rest in the one- and two dimensional case due to this increase of the number of closed loops. However in a three dimensional geometry the system needs a critical amount of disorder, which leads to a phase transition where the number of closed loops diverges, such that the transmission comes to rest. In 1985 Anderson proposed this interference effect to be the origin of Anderson localization. The theory was first presented in 1958 by Anderson in order to explain the metal-insulator transition, which earned him the Nobel-prize in 1977. However the existence of the interference effect causing this phase transition is experimentally not proven.

For a medium, which shows Anderson localization the diffusion coefficient becomes scale dependent. The transport through such a medium comes to a halt on a characteristic length-scale, the localization length. A time resolved measurement of the transmission, is expected to show the time dependence of the diffusion coefficient directly. The main advantage of this technique is that it allows to distinguish the absorption- from the localization length, which is not possible with static transmission experiments. The turbidity of the medium represented by the transport mean free path l^*, is the critical observable of the phase-transition to a localized state. Its value will be determined by a unique, custom designed coherent backscattering setup. The angular width of the enhanced backscattered intensity is inversely proportional to the value of the transport mean free path of the medium.

Therefore one needs samples which have both, a small value of l^* and a small absorption length. Furthermore the polydispersity of the samples plays an important role in order to achieve a turbid random medium of scatterers. In the theoretical section the basic concepts of single- and multiple scattering of light will be presented, such that characterization of the multiple scattering samples is possible. The experimental techniques, needed for the sample-characterization will be presented in section 4.3.

With these experimental methods we are able to present the first evidence of nonclassical diffusion in a three-dimensional random system. Systematic measurements of the effect of localization show a decrease in transport with an increasing turbidity, consistent with theoretical predictions. In particular, the time resolved transmission experiments show a scale-dependence of the diffusion coefficient which is independent of resonance scattering by the single scatterers. Moreover, measurements of time of flight distributions where the time reversal symmetry is broken by the Faraday effect provide evidence that the reduction of transport indeed relies on interference on reciprocal multiple scattering paths.

Chapter 2

Theory

In order to quantify the experimental results of this work, which is the search for Anderson localization of light, the primary thing to do is to create a solid fundament. Therefore one is interested to quantify expected deviations from a classical photon diffusion which is a multiple scattering effect. To be able to understand the multiple scattering of photons, one first needs to know the behavior of an electromagnetic wave for one single scattering event. The electromagnetic wave of a free photon can be described using Huygenss principle. This principle says that each position on the electromagnetic wavefront represents the origin of a spherical elementary wave. The envelope of those elementary waves then forms the resulting wavefront. In vacuum this results in a plain wave.

A single scatterer represents a local variation of the refractive index so that the elementary waves are distorted due to the fact that their optical paths are different. The difference in the optical length results in a phase shift, which changes the geometry of the wavefront. This change can be seen in an angular dependence of the scattered intensity called the form factor, $F(q)$, which will be introduced in the next section. The form factor can be used to characterize the geometrical and optical properties of the scatterer as presented in section 4.3.

In section 2.1 different theoretical approaches will be introduced in order to be able to understand single scattering. For an increasing density of scatterers, a single scattering approach however is not able to describe the physics properly. Therefore one has to use multiple scattering approaches which will be introduced in section 2.2. The most important measure of multiple scattering media is their turbidity represented by the value of its transport mean free path l^*. This is a characteristic length on which a photon loses the "memory" of the direction it formerly came from. As will be shown in section 2.2, the transport mean free path can be calculated using a combination of the form factor and the so called structure factor which is the Fourier transform of the spatial correlation of the scatterers forming the multiple scattering medium.

With this characteristic length one is able to describe the photon transport through a multiple scattering medium. This can be achieved by numerical methods using a random walk of photons. An analytical method relying on diffusion theory is another popular method in order to describe a multiple scattering system. Both methods give the same results in the limit where photons performed many scattering events. The analytical method of photon diffusion provides information on the broadening of a delta-pulse entering the medium. This is explained theoretically in section 2.3 to be able to describe the data recorded by the experiments described in section 3.2.

When dealing with electromagnetic waves care has to be taken due to the fact that each photon has a certain phase on its path through the multiple scattering medium. Although used in the calculation of the form factor, the wave nature is lost using just the value of l^* in order to describe multiple scattering. Due to the different phases for different path lengths the surface intensity in transmission or reflection is not homogenous anymore but shows bright an dark spots as a result from interferences of photons passing the medium on different path lengths. This complicated intensity pattern is called speckle and can be used to obtain information on the multiple scattering sample. Studying the temporal change of the speckles for instance allows one to measure the autocorrelation function in order to provide insight into the movement of the scatterers. This technique is called diffusing wave spectroscopy [3, 4].

When averaging over the different pathlengths the speckle is expected to average out to again form a homogenous intensity pattern. This however is not true since reciprocal photon paths in direct reflection have no phase difference and therefore always interfere constructively. This so called coherent backscattering was first discovered by Wolf and Maret [1] as well as vanAlbada and Lagendijk [2]. Coherent backscattering is also called weak localization to account for the fact that the theory of Anderson relies on exactly this mechanism to describe the transition from conductor to insulator of electrons in a solid for an increasing amount of disorder. The criterion for this to occur was given by Ioffe and Regel, which states that $kl^* \sim 1$ at the transition [5], where $k = 2\pi/\lambda$ is the wavevector inside the medium. As interference on reciprocal multiple scattering paths lead to an enhancement of the intensity on those paths, Abrahams et al. [6] predicted that the diffusion coefficient becomes scale dependent approaching the Ioffe-Regel criterion. At this critical amount of disorder, the number of closed loops is expected to diverge.

2.1 Single Scattering

The light scattering of an incident plain wave can be described in principle by a combination of a part that is passing the scatterer without being disturbed and an outgoing spherical wave. The ratio of these two different parts is dependent on the scattering cross section which is defined as the fraction of the scattering events in a certain time divided by the incident photon-flux.

The scattered photon flux j_{sca} through a surface element dA leads to the differential scattering crossection

$$d\sigma = \frac{j_{sca}}{|j_{inc}|} dA.$$

The surface element dA is given by

$$dA = r^2 d\Omega e_r,$$

such that the integration over the whole solid angle gives a value for the total scattering cross section:

$$\sigma = \int \frac{d\sigma}{d\Omega} d\Omega \tag{2.1}$$

By integrating (2.1) one is able to calculate the scattering behavior of a particle. This is however not a trivial problem since one needs the value of the differential crossection which has to be calculated directly from the properties of the scatterer and the scattered wave.

2.1.1 Rayleigh Scattering

For scatterers which are small compared to the wavelength of light, the incident plain wave can be considered homogenous over the size of the particle. The incident wave thus excites the scatterer to perform dipole oscillations, which have the same phase and direction with respect to the incident light. This dipole radiates intensity which is proportional to the volume V squared and to the fourth power of the incident wavevector k [7].

$$I(r) = \frac{16\pi^2 V^2 k^4}{r} \alpha^2 E_0^2 \sin^2 \vartheta. \tag{2.2}$$

The intensity is isotropic for the φ-axis as presented in Fig.2.1 and shows a $\sin^2 \theta$ behavior.

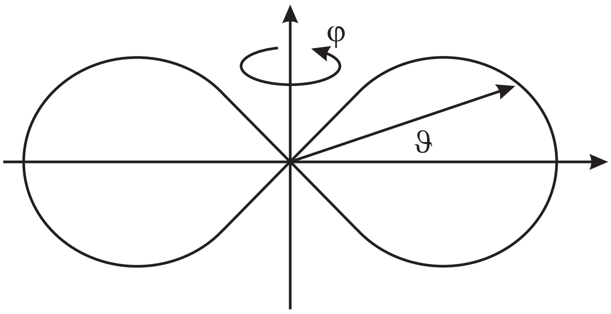

Figure 2.1: The angular intensity distribution of a rayleigh-scatterer. It shows a $\sin^2 \vartheta$ and an isotropic behavior for its φ-axis. This behavior correspond to the radiation of an electromagnetic dipole.

Rayleigh Debye Gans Scattering

Using the approach of treating scatterers as dipoles, one is able to expand the model to be able to describe bigger particles. This approach does not require a certain shape but will be presented here for spherical scatterers. The idea is to split the particle into infinitesimal volume elements that can all be considered as independent Rayleigh-scatterers. After passing the scatterer the different dipole-terms have to be added coherently in order to calculate the scattered intensity. However, the electric field inside the scatterer is assumed to be the same as that of the incident wave. This is called Born's first approximation and is quantified by the condition that

$$dk\left|\frac{n_{sc}}{n_0}-1\right| \ll 1, \tag{2.3}$$

with n_{sc} and n_0 the refractive indices of the scatterer and the incident medium respectively. As illustrated in Fig.2.2 the phase difference Δ between two scatterers having a distance r turns out to be

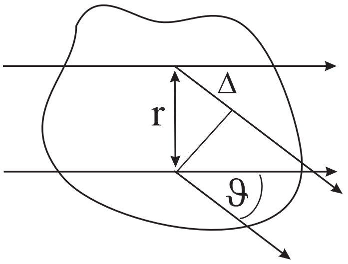

Figure 2.2: The approach to explain the scattering coming from an arbitrary shaped scatterer. The particle consists of many rayleigh scatterers which scatter the light isotropic. Due to the distance to each other the angular dependence of the scattered light is illustrated considering two scatterers with a distance of r.

$$\Delta = 2kr\sin\frac{\vartheta}{2} = \vec{q}\cdot\vec{r} \tag{2.4}$$

using the scattering vector $|q| = 2k\sin\frac{\vartheta}{2}$. Integrating the phase differences over the whole volume, one ends up with the so called form factor

$$F(q) = \frac{1}{V^2}\left|\int e^{i\vec{q}\cdot\vec{r}}dV\right|^2. \tag{2.5}$$

When dealing with spherical scatterers, this integral can be solved exactly to give a form factor of the form [8]

$$F(a) = \frac{9}{a^6}[\sin a - a\cos(a)]^2 \tag{2.6}$$

with $a = qr$ representing the size parameter of the scatterer.

However the use of Born's first approximation limits the method to particles with a low refractive index or small diameters. The single scattering on strongly scattering, large particles will briefly be explained in the following section.

2.1.2 Mie Scattering

In order to calculate the scattering properties in general, one has to solve Maxwell's equations. It is not surprising that this set of partial differential equations is not analytically solvable for arbitrarily shaped scatterers. Numerical approximations for example have to be used as presented by Schuerman [9] and Barber [10].
In a paper published in 1908, Mie [11] presented an analytical solution for the scattering of a plain monochromatic wave by a homogenous sphere having an arbitrary diameter. An equivalent solution to this problem was found by Debye [12] shortly thereafter. In his work Debye used light forces on a conducting sphere in order to end up with a solution to Maxwell's equation. The propagation of an electromagnetic wave which is represented by its wave-function $\phi(\vec{r}, t)$, can be calculated using the Helmholtz equation:

$$\bigtriangledown^2\phi(\vec{r}, t) + k^2\phi(\vec{r}, t) = 0$$

where the boundary conditions are given by

$$E^{med}_{tang} = E^{sc}_{tang} \tag{2.7}$$

$$H^{med}_{tang} = H^{sc}_{tang}, \tag{2.8}$$

which means that the tangential components of the electric and magnetic fields have to be continuous for an electromagnetic wave entering the scatterer (sc) coming from a homogenous medium (med). The solution to this differential equation is presented in various textbooks e.g. [8, 13] using slightly different techniques. The calculations end up in a scattering crossection having a nontrivial dependence on the diameter and the wavelength as presented in Fig.2.3. The following data was calculated using "Light Lab: Far Field Mie Scattering" [14]. For fixed values of those two parameters one is able to calculate the angular distribution[1] of the

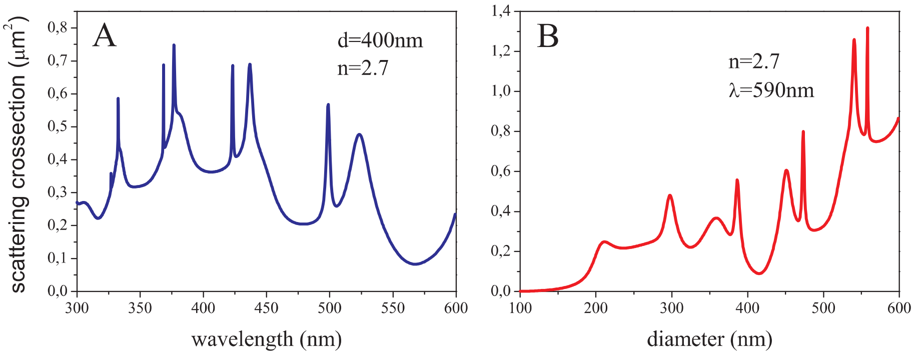

Figure 2.3: Scattering cross sections for different properties of the scatterers. The scattering cross section for Mie-scatterers shows a strong dependence on the wavelength (A) and the particle diameter (B).

---

[1] Instead of using the scattering angle θ one can also use the scattering vector $q = k_{out} - k_{in}$ to be the momentum change of the photon which calculates as $|q| = 2k\sin\theta/2$.

scattered intensity known as the form factor $F(\theta)$. The form factor shows characteristic minima as shown in Fig.2.4 for different particle diameters such that this measure can be used to characterize spherical particles as will be shown in chapter 4.3.

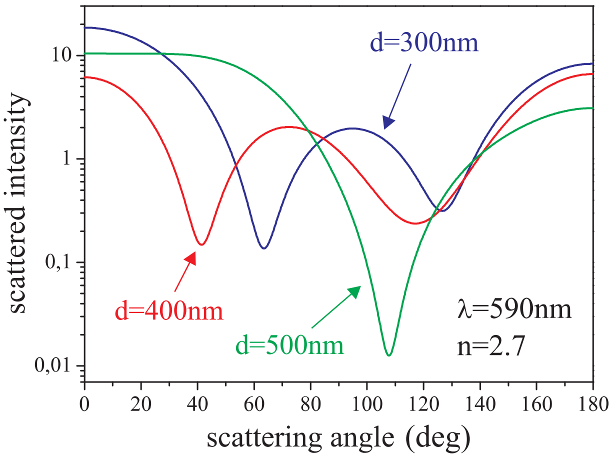

Figure 2.4: Form factor for different Mie-scatterers at fixed wavelength, $\lambda = 590nm$, and refractive index, n=2.7. There are several minima for different angles dependent on the diameter of the scatterers.

2.2 The Structure Factor

For dense systems, which will be naturally presented in the case of multiple scattering, the scattering cross section not only depends on the particle diameter. When the scatterers approach each other, i.e. their distance becomes of the order of the wavelength of the light, the scattering cross section also depends on the distribution of the scatterers. This results in the well known Bragg-peaks when the scatterers are periodically distributed. The scattering behavior is described by the so called structure factor $S(q)$. This $S(q)$ is related to the Fourier transform of the spatial pair-correlation function $g(r)$ that describes the probability to find a scatterer in the distance r to one test-particle placed at $r = 0$.

$$S(q) = 1 + \frac{N}{V}\int_V e^{-i\vec{q}\vec{r}}(g(r) - 1)d\vec{r} \tag{2.9}$$

Here N is the number of particles in a volume V. For small volume fractions, the structure factor is isotropic meaning $S(q) = 1$ and becomes angle-dependent for increasing particle density. From hard spheres, the structure factor can be calculated analytically which will briefly be presented here. Beginning with the Ornstein-Zernike equation for the correlation function, the method presented in more detail by Klein [15], one ends up with the so called Percus-Yevick [16] structure factor for particles having a diameter d compressed to a volume fraction f

as

$$S(q) = \frac{1}{1 - \frac{6f\tilde{c}(q)}{\pi d^3}}. \tag{2.10}$$

Here, $\tilde{c}(q)$ is the Fourier transform of the direct correlation function which in units of the particle diameter $x = r/d$ is given by

$$c(x) = -\frac{(1+2f)^2}{(1-f)^4} + 6f\frac{(1+f/2)^2}{(1-f^4)}x - \frac{f}{2}\frac{(1+2f)^2}{(1-f)^4}x^3. \tag{2.11}$$

The Percus Yevick structure factor $S(\theta)$ is shown in Fig.2.5 for different volume fractions f as a function of the scattering angle θ. One can see that $S(\theta)$ starts from an isotropic curve for small values of f towards a peaked one for an increasing volume fraction.

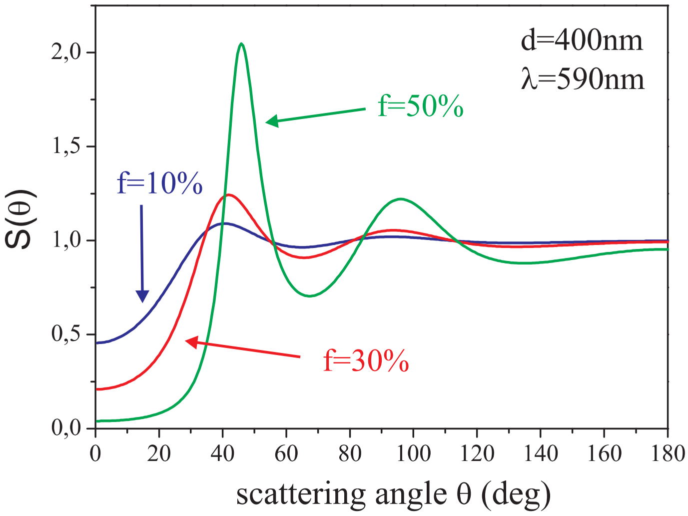

Figure 2.5: Percus Yevick structure factor for different volume fractions f for Mie-scatterers. One can see that the structure factor starts from an isotropic towards a peaked behavior for an increasing volume fraction.

2.3 Random Walk and Photon Diffusion

In order to describe the propagation of electromagnetic waves in a multiple scattering medium one has to combine both concepts, the single scattering properties of the scatterers, known as their form factor, and the effect that comes from their orientation in space, the structure factor. Scalar wave propagation in random media can then be described using the Green's function (see e.g. [17]). This function gives information about the propagation of the amplitude for a single scattering event. When averaged over the the whole disordered system one ends up with the amplitude-Green's-function [18]. The whole concept in order to describe wave propagation using this concept in presented in more detail in [19].

There is also a numerical approach that can be used in order to describe such multiple scattering systems. This is the random walk approach, where the microscopic mechanism of multiple scattering is not taken into account directly. All details of the scattering are put into the mean free path of the random walk, which depends on the scattering cross section. Due to the fact that there is an electromagnetic wave entering the multiple scattering system it is not obvious that the random walk approach is able to describe the light-transport through such systems. Fortunately, the detected light is the intensity traveled through the system and one does not have to consider the full electromagnetic wave-field but only the contribution from constructive interference of the photons that have passed the medium.

For simplicity the concept will be explained in one dimension, which can easily be expanded to three dimensions. The random walk calculates the probability to find a photon for a certain time $t_i = i\delta t$ starting with $t_{i=0} = 0$ at a position $r_i = r_0 + n\delta r$. Using discrete step-lengths given by the characteristic length scale being the transport mean free path l^* one ends up with a simple model to describe e.g. transmission experiments.

The photon starts its diffusion at $r = 0$. After a time δt the photon has performed one step δr in either the positive or the negative direction. Because the probability for both directions $\pm r$ is the same, the mean position of many photons performing such a random walk has to stay centered around $r = 0$. When one wants to know the distance that a certain number of photons have traveled after a fixed time, one needs to calculate the spread of the random walk. This can be done by considering the mean square displacement $\langle r^2(t_i)\rangle$ of all particles for the time t_i.

$$\langle r^2(t_i)\rangle = \frac{1}{N}\sum_{j=0}^{N} r_j^2(t_i) \tag{2.12}$$

Since the distance which the photon travels after δt is given by $r(t_i) = r(t_{i-1}) \pm \delta r$ one can rewrite (2.12) as

$$\langle r_j^2(t_i)\rangle = \frac{1}{N}\sum_{j=0}^{N}[r_j^2(t_{i-1}) \pm 2\delta r r_j(t_{i-1}) + \delta r^2]. \tag{2.13}$$

For a large number of photons the second term, which is linear in r, vanishes after performing an ensemble average. It is easy to understand this from the fact that the photon-cloud has to stay centered in space due to the symmetry of the random walk. Including the starting conditions that for $t = 0$ there is no displacement one obtains the expression for the mean square displacement at time t

$$\langle r_j^2(t)\rangle = \frac{t}{\delta t}\delta r^2 \tag{2.14}$$

where δt is the time a photon needs to perform one step. One can use the expression $\delta r^2/2\delta t$ to form a constant which provides a characteristic measure for the system. This measure corresponds to the diffusion coefficient D which connects the random walk approach to diffusion theory. Therefore one is able to rewrite the expression (2.3) to be

$$\langle r_j^2(t)\rangle = 2Dt. \tag{2.15}$$

The expansion to the three dimensional case is done by adding up the contributions for the independent one dimensional random walks. Doing this, one calculates a value for the mean square displacement

$$\langle r^2\rangle = \langle r_x^2\rangle + \langle r_y^2\rangle + \langle r_z^2\rangle = 6Dt. \tag{2.16}$$

To be able to calculate the diffusion equation one has to take a closer look at the number density of photons. Assuming photon conservation[2], the change of the photon density $\partial_t\rho$ in a volume-element has to be due to a flux $\vec{j}$ of photons. This behavior is described by the equation of continuity

$$\partial_t\rho = -\nabla\vec{j} \tag{2.17}$$

Taking into account that the photon flux is originating from a gradient in the photon density the temporal change can be rewritten using Fick's law $\vec{j} = D\nabla\rho$ to be

$$\partial_t\rho = D\nabla^2\rho. \tag{2.18}$$

Due to the fact that there is always absorption in real samples, one has to include this into the above diffusion equation. This term is expected to lead to an exponential decay of the photon density, so (2.18) writes as

$$\partial_t\rho = D\nabla^2\rho - \frac{1}{\tau_a}\rho, \tag{2.19}$$

introducing a characteristic absorption time τ_a that corresponds to an absorption length $l_a = c\tau_a$ with c the effective speed of light inside the medium.
In an infinite medium which is a medium without boundaries a Gaussian function with an exponential decay solves (2.19) such that the photon probability is given by

$$\rho(r,t) = \frac{N}{\sqrt{4\pi Dt}} exp\left[\frac{-r^2}{4Dt} - \frac{t}{\tau_a}\right] \tag{2.20}$$

when calculating the mean square displacement $\langle r^2\rangle$ of the Gaussian, one ends up with an expression analogous to that from the random walk, namely

$$\langle r^2\rangle = \frac{1}{N}\int r^2\rho(r,t)dr = 2Dt \tag{2.21}$$

in one dimension.
In all of the above, the determining factor is the characteristic length of the random

---

[2] When dealing with photons one cannot assume that their number is conserved. Photons will be absorbed in every material a multiple scattering sample is made of. However this absorption will be left out for the moment and included afterwards for sake of completeness.

walk, called scattering mean free path l_s. This length takes into account the details of the scattering process via the scattering cross section σ and the density of the scatterers ρ_{sc} via

$$l_s = \frac{1}{\rho_{sc}\sigma}, \tag{2.22}$$

if the individual scattering events are uncorrelated. This scattering mean free path is the length on which the orientational correlation is lost due to scattering. Considering again the concept of a random walk through a multiple scattering medium while assuming an exponential path length distribution the mean square displacement $\langle r^2 \rangle$ for a dimensionality d turns out to be

$$\langle r^2 \rangle = \frac{2sl_s}{d}, \tag{2.23}$$

where $s = ml_s$ for the photon pathlength after m steps. Combining (2.21) and (2.23) one ends up with an expression for the diffusion coefficient

$$D = \frac{v_E l_s}{d} \tag{2.24}$$

When dealing with scatterers with diameters comparable to the wavelength, one has to use Mie-theory in order to describe the angular scattering behavior. The anisotropy has to be taken into account when one wants to calculate the transport mean free path for such samples. This is due to the fact that Mie-scatterers have enhanced scattering in forward direction. Therefore one has to take into account that there is a correlation in the directions of photon transport. This can be included into the formalism introduced so far by calculating the anisotropy factor

$$\langle \cos\theta \rangle = \frac{\int \cos\theta\sigma(\theta)d\Omega}{\int \sigma(\theta)d\Omega}, \tag{2.25}$$

which for Rayleigh-scatterers is zero. The scattering mean free path l_s for Mie-scatterers then has to be replaced by the transport mean free path

$$l^* = \frac{l_s}{1 - \langle \cos\theta \rangle} \tag{2.26}$$

in order to be able to describe the new system with the same formalism [19].

2.3.1 Slab Geometry

As already mentioned, after a certain number of scattering events the photon transport can be treated as a diffusion of photons which gives an analytical expression for the transport properties. However this diffusion approach describes the spread of a delta peak assuming an infinite geometry to spread. Obviously this geometry cannot be achieved experimentally, such that one has to find a way of including

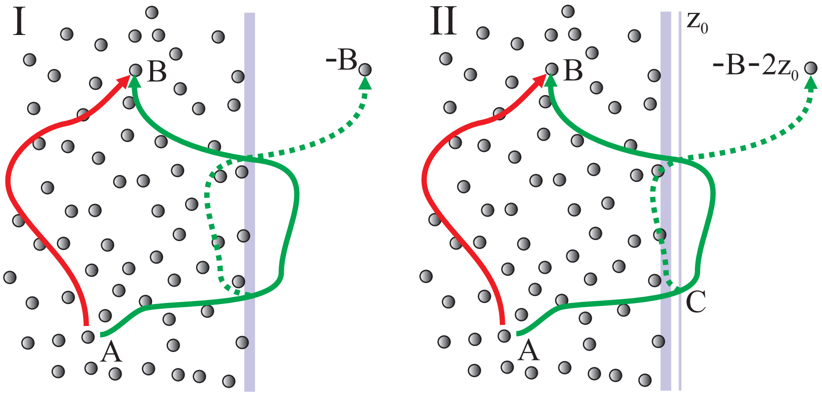

Figure 2.6: Illustration of the image point method for the two different cases, the reflecting I and the transparent II boundary. For a reflecting surface all paths that would reach -B are reflected back into the medium and end at the point B. However for a transparent surface all paths that would end at B and cross the surface have to be subtracted. However due to the fact that there are scatterers forming the sample there is no sharp boundary in order to cut off the paths. Therefore one has to subtract all paths from A to z_0 that go to B.

boundaries in order to describe samples having a finite size. Therefore one has to use radiative-transfer theory, which allows the treatment of the boundaries over the Milne-parameter. This for instance is done by Lenke et al. [19] using the so called image point method. As illustrated in Fig.2.6 the probability $\rho(A \to B)$ that a photon travels from a point A to a point B in the vicinity of a boundary has to be considered. The probability is given by the sum of all paths leading to that point. However for a finite size of the sample, one always finds paths that are outside the sample. For such paths there are two possibilities:
For a sample with a fully reflecting surface one has to add all paths that start at the point A and end at $-B$ to the probability

$$\rho_{refl}(A \to B) = \rho(A \to B) + \rho(A \to -B) \tag{2.27}$$

because they are reflected into the sample again. This is illustrated in Fig.2.6I.
The transmitting surface, as presented in Fig.2.6II, is more complicated to consider. The photons that cross the surface are able to leave the sample. This transparent case writes as

$$\rho_{trans}(A \to B) = \rho(A \to B) - \rho(A \to -B), \tag{2.28}$$

where all paths leaving the sample have to be subtracted. Those are the paths that meet the point C that lies on the surface of the sample. A random walk beginning at this point turns out to have the same probability to end at the points B and $-B$. When looking closer at (2.28) one sees that there is a discontinuity in photon density when leaving the sample. The density drops from a finite number inside the sample to zero at the border, which is unphysical. However due to the fact that there are scatterers forming the sample there is no sharp boundary in order to cut off the paths. Therefore one has to subtract all paths from A to z_0 that go to B. One has to rewrite (2.28) in order to take this into account.

$$\rho_{trans}(A \rightarrow B) = \rho(A \rightarrow B) - \sum_{n=1}^{m} \rho(A \rightarrow z_0; n)\rho(z \rightarrow B; m-n) \tag{2.29}$$

Here ρ_{trans} is the probability that a photon travels from A to B in m steps. The sum can be rewritten as an integral using the fact that the probability to get from A to B is the same than from A to $-B - 2z_0$ as presented in Fig.2.6.

$$\rho_{trans}(A \rightarrow B) = \rho(A \rightarrow B) - \int_0^\infty p(z)\rho(A \rightarrow -B - z_0)dz \tag{2.30}$$

Here $p(z)$ is the probability distribution of the values of z_0 which can e.g. be assumed to be a step-function or an exponential decay.

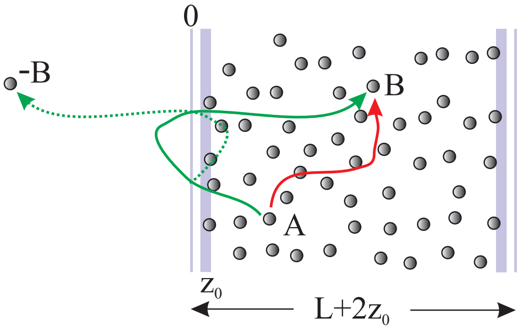

Figure 2.7: Schematics on the transmission of a finite sample size. The reflected paths have to be added to the photon-density whereas the transmitted photons have to be subtracted. There is an infinite number of image points because every surface has to be imaged into the opposing one. This concept allows to use diffusion theory to describe the photon transport for finite sample sizes.

This result can now be used to describe a finite sample with two boundaries, i.e. a slab geometry. This is illustrated in Fig. 2.7 where the surfaces are transparent. This leads to an infinite number of image points because every surface has to be imaged into the opposing one. Doing this for every surface one ends up with a photon density of

$$\begin{aligned} \rho_{trans}(A \rightarrow B) &= \rho_\infty(A \rightarrow B) - [\rho_\infty(A \rightarrow -B^0) \\ &- [\rho_\infty(A \rightarrow -B^{0L'}) - [\rho_\infty(A \rightarrow -B^{0L'0}) \ldots]]] \\ &- [\rho_\infty(A \rightarrow -B^{L'}) \\ &- [\rho_\infty(A \rightarrow -B^{L'0}) - [\rho_\infty(A \rightarrow -B^{L'0L'}) \ldots]]] \end{aligned} \tag{2.31}$$

where $B^0 = -B$ and $B^{L'} = 2L' - B$ are the image points with respect to the surfaces at $z = 0$ and $z = L' = L + 2z_0$ and so on. Keeping this in mind one is able to rewrite (2.31) using $\rho_\infty(X \to Y)$ the photon density to diffuse from X to Y in an infinite space, as an infinite series

$$\rho_{trans} = \sum_{m=-\infty}^{\infty} \rho_\infty(A \to B + 2mL') - \rho_\infty(A \to -B + 2mL'). \tag{2.32}$$

Assuming the geometry to be a slab where the x and y dimensions can be considered infinite, they can be described using free diffusion

$$\rho_\infty(x,t) = \frac{1}{\sqrt{4\pi Dt}} e^{\frac{-x^2}{4Dt}} e^{\frac{-t}{\tau_a}} \tag{2.33}$$

with τ_a the absorption time and D the diffusion coefficient and the above discussion needs only to be applied to the z-direction. Thus inserting (2.33) into (2.32) the photon density in the z-direction is given by

$$\rho_{trans}^z = \frac{e^{-t/\tau_a}}{\sqrt{4\pi Dt}} \sum_{-\infty}^{\infty} \left[\exp - \frac{(z_B + 2mL' - z_A)^2}{4Dt} - \exp - \frac{(2mL' - z_B - z_A)^2}{4Dt} \right]. \tag{2.34}$$

Using the Poisson sum formula[3] (2.34) can be rewritten as

$$\rho_{trans}^z(A \to B, t) = \frac{2e^{-t/\tau_a}}{L'} \sum_{n=1}^{\infty} \exp\left(-\frac{n^2\pi^2}{L'^2} Dt\right) \sin\left(\frac{n\pi}{L'} z_A\right) \sin\left(\frac{n\pi}{L'} z_B\right). \tag{2.35}$$

In order to compare theoretical calculations with measurements a more interesting quantity than the photon density is the transmitted intensity through the slab. This value can be calculated using Fick's law which connects the photon-density with the photon-current:

$$I_{trans}(t) = -D\frac{\partial \rho}{\partial z} = -\frac{2De^{-t/\tau_a}}{L'} \sum_{n=1}^{\infty} \exp\left(-\frac{n^2\pi^2}{L'^2} Dt\right) \frac{n\pi}{L'} \sin\left(\frac{n\pi}{L'} z_A\right) \cos\left(\frac{n\pi}{L'} z_B\right) \tag{2.36}$$

Considering that z_B is comparable to L' the cosine can be replaced by $(-1)^n$. Furthermore, $z_A \approx z_0 \ll L'$ such that the sine can be replaced by its argument (z_A can be approximated by the value of the transport mean free path l^*). This leads to a transmitted intensity

$$I(t) = -2De^{-\frac{t}{\tau_a}} \sum_{n=1}^{\infty} (-1)^n \exp\left[-\frac{n^2\pi^2}{L'^2} Dt\right] \left(\frac{n\pi}{L'}\right)^2 \frac{l^*}{L'}. \tag{2.37}$$

This formula can now be used to theoretically characterize time resolved transmission data which will be presented in section 5.2 in detail.

---

[3] $\sum_{n=1}^{\infty} f(n) = \sum_{m=-\infty}^{\infty} \int_{-\infty}^{\infty} e^{-2\pi mia} f(a) da$

2.4 Coherent Backscattering

The mathematical description that has been developed so far is able to explain the transport of particles through a scattering medium. Although this approach is able to explain most cases of photon transport, the wave-nature of light has not been implemented so far. For an increasing coherence of the incident light one is able to see the so called speckle-pattern both in transmission and reflection. This is an intensity pattern which looks granular. The origin of this pattern is the interference of photons on different paths through the sample, leading to a phase-difference at the positions where they leave the medium. The speckle-pattern cannot be seen for moving scatterers. This is due to the fact that the phase differences are very sensitive to the movement of the scatterers, which results in a change of the pathlengths of the photons that end on a certain point of the medium. This again results in a different phase and changes the intensity at this particular point.

Measuring the autocorrelation of a fluctuating speckle, one is thus able to collect information of the movement of the scatterers. This technique is called diffusing wave spectroscopy and can be used to characterize a flow of scatterers as explained in [20]. Even the flow of scatterers deep inside a turbid medium can be recorded using this method as shown by Heckmeier [21].

All samples that are expected to show a sign of localization of photons however consist of non moving scatterers, meaning that their speckle pattern is stationary. When averaging over the various speckles[4] one ends up with the diffusion equation for the photon transport as derived in the previous section, which described the surface intensity. In back-reflection this leads to Lambert's law, which states that the angular dependence of the back-reflected intensity is proportional to the cosine of the angle.

Coherent Backscattering

As already mentioned above, the averaging over an ensemble of photon paths in the multiple scattering medium "washes out" the speckle-pattern. However one interference effect survives this averaging. It is the constructive interference on so called "time reversed paths" in direct back-reflection. Here, every path has a counterpart corresponding to the same path travels in the opposite direction as shown in Fig.2.8. Thus, both of the paths have the same phase and will interfere constructively. Those paths cannot be averaged out by a movement of the scatterers or the whole sample, which does wash out all speckle spots. This means that there is always a twofold enhancement of the intensity in direct back-reflection. This effect was first measured by Wolf and Maret [1] as well as van Albada and Lagendjik [2]. This was experimental evidence that there is an interference on

---

[4] The brownian motion of the scatterers in a solvent causes such an averaging over the different speckle patterns. For a static- or frozen speckle the averaging can be achieved by moving or rotating the sample.

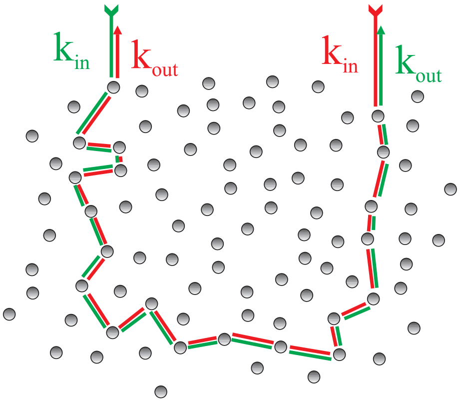

Figure 2.8: All paths in backreflection have a time reversed path with the same length. Photons traveling on such time reversed paths are always in phase even when the scatterers are in motion as long as the transit time of photons is much shorter than the phase coherence time. Therefore one gets constructive interference in reflection for photons even for an ensemble average on different paths the photons travel that averages over the so called speckle patterns.

time reversed paths inside the sample which was expected to be the mechanism behind Anderson localization. Therefore one calls this coherent backscattering effect weak localization. Coherent backscattering can be used as a tool for sample characterization which will briefly be presented here. It is discussed in full detail in [19]. In order to calculate the coherent intensity one has to sum up the ratio of the coherent and non-coherent light paths.

$$CBE(\vec{q},\vec{r}) = \frac{|E_1^2 + E_2^2|}{|E_1^2| + |E_2^2|} \tag{2.38}$$

As shown in [19] the phase-difference oscillates for a fixed distance R on the surface of the sample for different detection angles. This effect is illustrated in Fig.2.9 and has an analogy to a double-slit experiment. For a very large number of contributions with different surface distances R, each having a different period, one ends up with an angular dependence of the intensity starting at twice the illuminated intensity and showing a decay which is determined by the transport mean free path of the medium. When a photon performs just one scattering event there is no corresponding counter propagating path and therefore those photons do not contribute to the enhancement in direct backreflection. The twofold enhancement factor in backreflection thus has to be corrected according to

$$CBE(\vec{q} = 0) = 1 + \frac{I_m}{I_m + I_s} = 1 + C_0 \tag{2.39}$$

where I_m is the intensity that is scattered multiple times whereas I_s represents the Intensity coming from the reflected light at the surface that is singly scattered. The value of C_0 represents the amount of coherence leading to an enhancement in direct back-reflection. This measure is dependent on polarization and the scattering

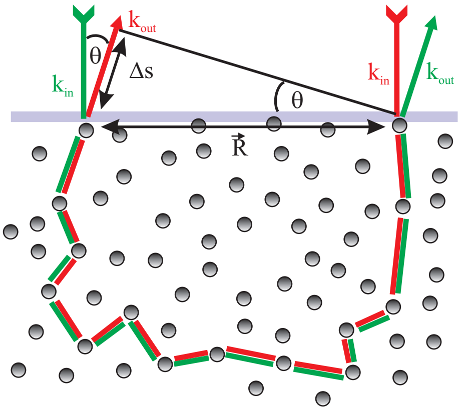

Figure 2.9: The angular dependance of the backscattered intensity can be understood by looking on the phase-shift for a fixed distance R the photons travel in respect to the surface of the sample. This construction reminds on a double-slit experiment. The phase-shift comes from the different paths-lengths $\delta s = R \sin\theta$ the counter propagating photons travel.

anisotropy and varies between 1 (circular polarization) and 0.7 (linear polarization using Rayleigh-scatterers).

In order to calculate the angular dependence, the problem of calculating the phase-shifts can be simplified by making some assumptions:

1. Almost normal incidence of the light. This can be achieved experimentally without any problem.
2. The scattering angle θ_b can be treated as very small. This is an assumption which can cause problems for samples having a very small value of the transport mean free path l^* as will be derived in the following discussion.
3. The distance $\vec{R}$ lies in the xy-plain. This is valid for almost every multiple scattering medium since for a turbid sample having high volume-fraction the photon paths end within a depth δz being of the order of the transport mean free path l^*

When taking those assumptions into account, the reversed path is longer than the original path by

$$\delta s = R \sin\theta \approx R\theta. \tag{2.40}$$

This corresponds to a phase-shift of $k_0\theta R \approx qR$ using the second assumption. Here $k_0 = 2\pi/\lambda$ is the wave vector in the incident medium which is generally air. Averaging over all possible distances R of photon paths, which can be done by an integration over the radial intensity distribution around the central point of illumination one obtains

$$CBE(\vec{q}) = 1 + \frac{1}{I_m + I_s}\int_{\lambda}^{\infty} I(\vec{R})\cos(\vec{q}\vec{R})d^3\vec{R} \tag{2.41}$$

using $I_m = \int_\lambda^\infty = I(\vec{R})d^3\vec{R}$ for the multiply scattered and $I_s = \int_0^\lambda = I(\vec{R})d^3\vec{R}$ as an expression for the singly scattered intensity.

One can see that (2.41) is nothing else than the real part of the Fourier transform of the surface intensity which is not surprising since the mechanism of interference on time reversed paths is similar to a double slit experiment. The surface intensity of the diffusion ansatz for a path length s is simply a Gaussian as discussed in the previous section

$$I(\vec{R}, s) = \frac{3}{4\pi s l^*} \exp\left(-\frac{3\vec{R}^2}{4sl^*}\right). \tag{2.42}$$

This is easily Fourier-transformed and then has to be averaged over all path-lengths to be put into (2.41) which yields

$$CBE(\vec{q}) = 1 + C_0 \int_s^\infty p(s) exp\left(-\frac{sl^*q^2}{3}\right) ds, \tag{2.43}$$

using the normalized path length distribution $p(s)$. The problem now is to calculate the integral over the path lengths. This has been done by Wolf and Akkermans et al. [22, 23] leading to an expression for the enhancement to be

$$CBE(q) = 1 + C_0 \frac{1 - \exp\left(-2(1+\gamma)l^*\sqrt{q^2}\right)}{2(1+\gamma)l^*\sqrt{q^2}}. \tag{2.44}$$

In this expression the so called Milne-parameter γ is used. As noted before, this parameter can be derived from the solution of the radiative transfer equation [24, 7] and describes the intensity balance of a mesoscopic volume element. One obtains $\gamma = 0.7104$ for Rayleigh- and $\gamma = 0.7182$ for Mie-scatterers. Expanding (2.44) for small values of q the coherent backscattering intensity writes as

$$CBE(q) = (1 + C_0) - C_0(1+\gamma)|q|l^* + O[q]^2. \tag{2.45}$$

The full width at half maximum of the coherent backscattering enhancement is then very close to the inverse of kl^* which allows a simple measurement on this property by analyzing the backscattered light.

As mentioned above, this concept is valid for scalar waves where no polarization effects are taken into account. Furthermore there is no absorption included, which would correspond to a cut-off of the path lengths in $p(s)$. For an increasing amount of absorption the tip of the cone becomes round where the enhancement stays the same. This is because absorption affects both the original and the counter-propagating lightpaths such that the coherence is not influenced by absorption at all.

Fig. 2.10 shows the coherent backscattering cone for different values of kl^* assuming an enhancement factor $C_0 = 1$. One can see that the cone-width increases for a decreasing value of the transport mean free path.

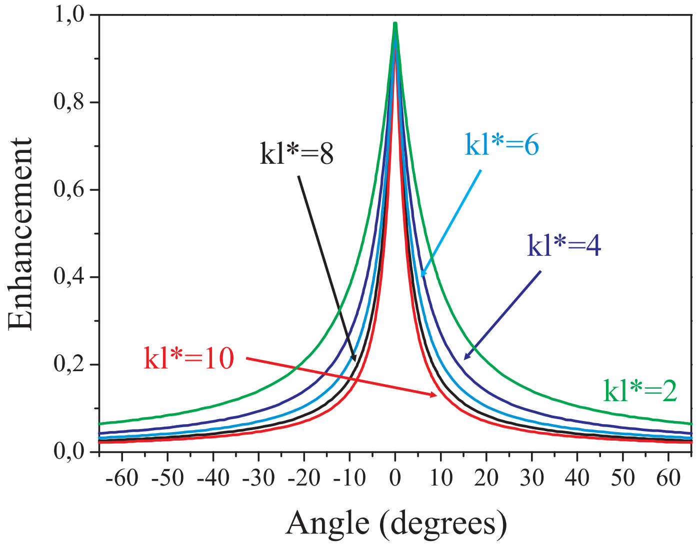

Figure 2.10: Dependence of the conewidth on the value of kl^*. The enhancement represented by the value of C_0 is set equal to unity. The with of the coherent backsscattering signal is inversely proportional to the value of the transport mean free path times the wavevector kl^*.

Internal Reflections

Knowing that the angular width of the backreflected light is the Fourier transform of the surface intensity, it is not surprising that the reflectivity of the surface has to be taken into account properly. When photons inside the sample are reflected back into the multiple scattering medium the width of the surface intensity will be increased. An increasing surface intensity causes the cone width to decrease which leads to an overestimation of the value of l^*. This is illustrated in Fig. 2.11, where photons near the surface are reflected back into the sample causing a broadening of the diffuse intensity on the surface of the sample. Therefore one has to correct (2.44) using the reflection R' of the sample in order to be able to get information on the value of $(kl^*)_{refl}$ the . The surface reflection can be calculated using energy-density coherent potential approximation (ECPA) theory [26] which provides a value of the mean refractive index of the medium. Knowing the reflectivity of the multiple scattering medium one can correct the FWHM according to Zhu et al. [25] who calculate the correction of kl^* as a function of the sample reflectivity R' into (2.44).

$$(kl^*)_{refl} = \left[1 + \left[\frac{2(1+R')}{3(1-R')}\right]\right](kl^*)_{fit} \tag{2.46}$$

Fig.2.12 shows the coherent backscattering cone of a compressed TiO_2 powder (Du Pont R700). The fit to the measured data gives a value of $kl^* = 8.5$, which is bigger than the real value which turned out to be 2.5 when the surface reflections are taken into account. The value of the averaged refractive index using ECPA defines the reflectivity R' of the surface. When corrected by the formula presented

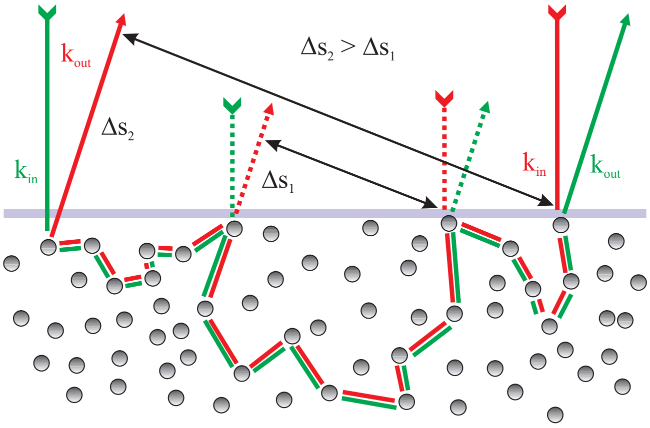

Figure 2.11: Illustration of the effect of the surface reflection of a multiple scattering sample on the coherent backscattering cone. The surface reflection increases the surface intensity which affects the coherent backscattering cone. The width of the measured cone decreases which leads to an overestimation of the value of kl^*.

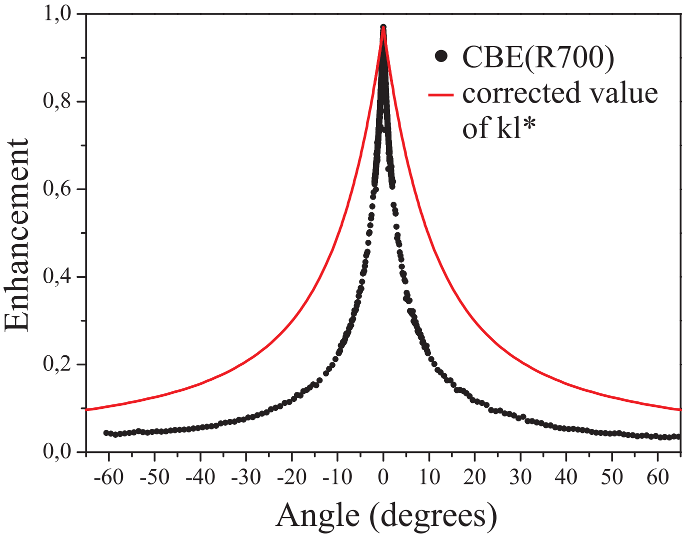

Figure 2.12: Measurement of the coherent backscattering of compressed TiO_2 powder. The direct theoretical fit to the data would correspond to a value of $kl^* = 8.5$. However due to the fact that the reflection on the sample surface is not taken into account this fit is an overestimation of this value. The corrected coherent backscattering data where reflection on the surface is included follows the red curve corresponding to a value of $kl^* = 2.5$.

in [25] the cone would follow the red curve in the figure. One can see that the measured data clearly overestimate the transport mean free path of the multiple scattering medium.

2.5 Anderson Localization

In 1958 Anderson [27] presented a theory which suggests the origin of the metal-insulator transition to be due to the scattering of electrons inside a metallic medium. He claimed that for increasing turbidity of the medium there is a transition from a conducting into an insulating phase. As shown in the previous section, constructive interference increases the probability that an electron or photon returns to a scatterer that it has passed already. This leads to a reduction in the electron transport because the electrons stay inside the medium longer than expected considering diffusion alone. An increasing number of those closed loops, Anderson claimed, would lead to a phase-transition where the electron-diffusion completely disappears. This would cause the mean-square displacement, $\langle r^2 \rangle$, which is a measure for the spread of an electron cloud to become constant. Furthermore it is expected to lead to a scale-dependence of the diffusion coefficient which will be explained in the following section.

First one has to be aware of the experimental difficulties in order to be able to observe this strong- or Anderson localization transition. If one wants to measure strong localization of electrons, the transmission through the scattering medium plays an important role. Classical electron diffusion is well understood and known as Ohm's law which states that the transmission through a certain medium is proportional to the inverse of its thickness. All deviations from this behavior should be due to Anderson localization. Unfortunately this is not the case since electrons are charged and therefore interact with each other, which has an influence on their transport behavior. Furthermore, they can interact with the atoms, which means that there is a possibility that they form bound states which also reduces the diffusion of the electrons. Aware of this problem, Anderson suggested [28] to search for the localization transition using photons. Photons have the advantage that they are not charged and therefore do not interact with each other. In addition there are no bound states for photons.

The experimental discovery of coherent backscattering of photons was a very important success for the possibility to provide information in order to proof the existence of Anderson localization. The fact that interference on time reversed paths occurs in multiple scattering samples provided evidence that the mechanism, which is expected to lead to Anderson localization really exists.

Renormalized Diffusion

As already mentioned, interference on time reversed paths leads to an enhanced probability to return to the position of one scatterer lying on a closed loop. This fact does not seem very intuitive, but can be easily explained with the help of coherent backscattering. As presented in Fig. 2.13A and explained in detail in the previous section the intensity in direct back-direction of a multiple scattering sample is enhanced by a factor of two. The scattering geometry is a semi infinite half-space which is not really needed for the mechanism but important in order to measure the effect.

Let us now consider a closed loop inside a multiple scattering medium as shown in Fig. 2.13B. Taking one point out of such a loop, one can easily see that due to interference with the counter-propagating photon there is an enhanced intensity at that position. The fact that this is valid for each scatterer where a closed loop is possible means that the intensity on paths which are able to form a closed loop is enhanced. This however affects the photon-transport because there are photons stored inside the scattering medium when they are able to form a closed loop. Thus, interference on time reversed paths leads to a reduction of the diffusion coefficient. When the turbidity increases further, the density of closed loops increase, such that every scatterer can be the starting point for a different closed loop as illustrated in Fig. 2.14. Thus the reduction of the diffusion coefficient introduced above depends on how many closed loops are taken into account and hence on the size of the sample.

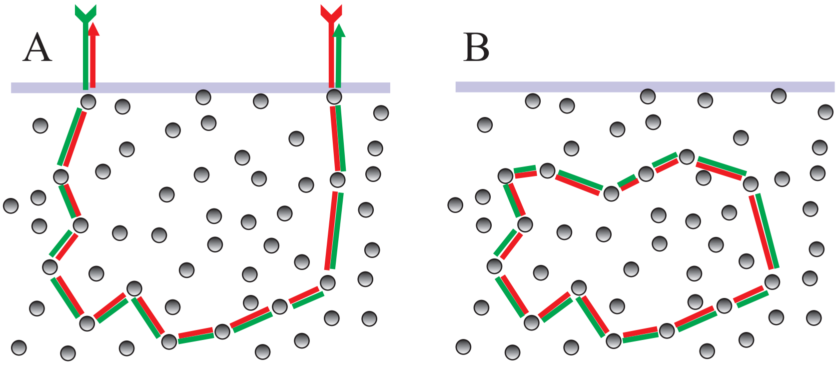

Figure 2.13: The coherent backscattering schematics A shows the construction of time reversed paths that explains the twofold enhancement in direct back reflection. As illustrated in B there is another way for constructive interference on time reversed paths to occur. This happens if the multiple scattering paths turns back on itself, forming a closed loop. Here, there is always constructive interference and therefore the intensity is enhanced by a factor of two on every particle scattering the photon.

Before going into details what the diffusion coefficient is going to look like, we have to discuss under which conditions such a macroscopic population of the closed loops is expected to occur. First of all, one needs strong scattering in a random medium in order to observe localization. Another very important factor to consider is the dimensionality of the system. It turned out that the dimension where photon-diffusion takes place is crucial in order to be able to observe the effect. Abrahams et al. [6] treated the role of the dimensionality for localization and found out that in the one-dimensional case an infinitesimal amount of disorder is sufficient in order to bring diffusion to rest. The two-dimensional case turned out to show localization for each infinite medium meaning that the localization lengths[5] is fi-

---

[5] The localization length is the path length on which the photons start to macroscopically form closed loops. This macroscopic population is expected to reduce the photon-transport.

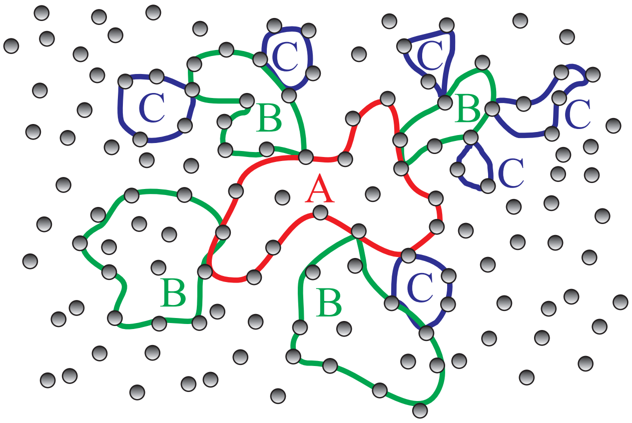

Figure 2.14: Photons on closed loops reduce the photon-transport expected by diffusion theory because of the enhanced intensity due to constructive interference. The fact that one scatterer not only corresponds to one closed loop allows the possibility of a macroscopic population of those closed loops. This is expected to be the mechanism which causes a scale dependance of the diffusion coefficient.

nite. Both in the one- and the two-dimensional case therefore the photon diffusion is reduced due to this effect, meaning that there is no phase-transition between a classical and a localized state.

Considering the three-dimensional case, Abrahams and Licciardello [6, 29] claimed that there has to be a certain amount of disorder in the system causing the photon diffusion to be reduced. This critical amount of disorder can be expressed by the so called Ioffe-Regel criterion [5]

$$kl^* \approx 1 \tag{2.47}$$

meaning that the wavelength $\lambda = 2\pi/k$ has to be of the same order of magnitude as l^* inside the sample. This however means that the electromagnetic wave cannot be considered to be a plain wave since it is scattered again before the electromagnetic fields form such a plain wave. Therefore the diffusion-picture should no longer hold if one wants to describe Anderson localization in full detail. In their work Abrahams et al. [6] also calculated the behavior of two- and one dimensional systems. Here the conductivity σ together with the length L of the medium can be put together which leads to the conductance $G = \sigma L^{d-2}$ where d represents the dimensionality of the system. This conductance can be normalized using the so called "Thouless number" which leads to

$$g(L) = G(L)\frac{\hbar}{e^2} \tag{2.48}$$

Plotting the value of $\beta = \frac{d \ln g}{d \ln L}$ over the normalized conductivity $\ln g$ for the different dimensions one ends up with the curves presented in Fig.2.15. Here one can see that the value of β is always negative for $d < 3$ meaning that the conductance decreases with increasing values of L. In the three-dimensional case the curve crosses the x-axis meaning that there is a regime where the conductance increases

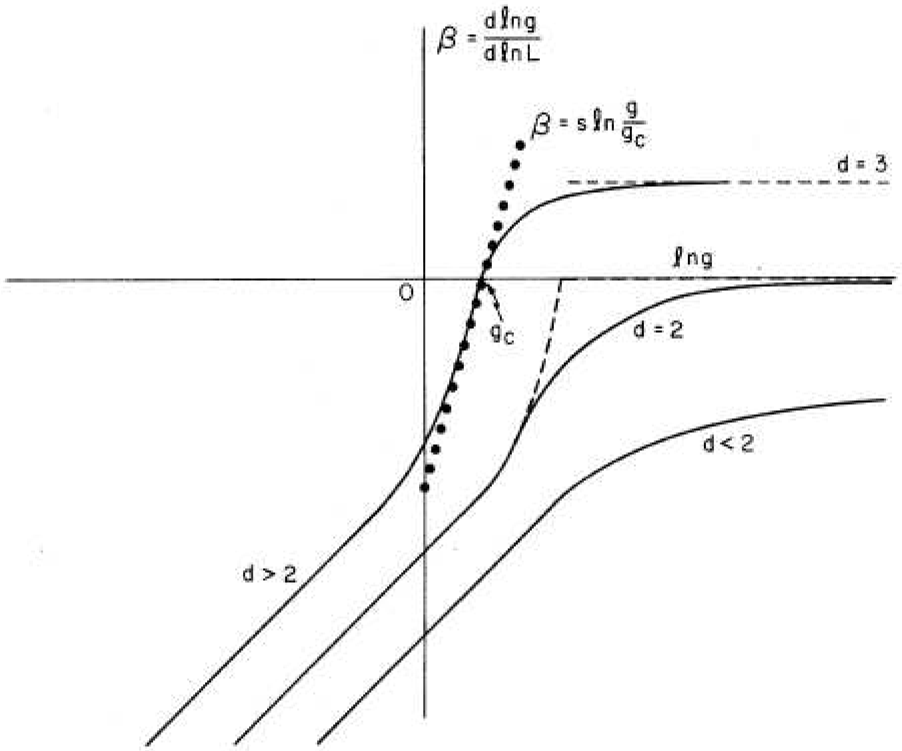

Figure 2.15: Plot of $\beta(g)$ versus $\ln g$ for different dimensions. Performing an extrapolation of β for big and small values of $\ln g$ one obtains a localizing behavior for the one- and two-dimensional case. Considering a three-dimensional medium Abrahams et al. obtained a transition from a localizing to a conducting behavior. From the slope at $\beta = 0$ one is able to get the critical exponent s of the localization length.

with size. The point where this curve crosses zero is the transition point from a localized state to one characterized by classical transport. The inverse of the slope s at this point represents the critical exponent of the localization length at the transition to strong localization.

Since one is interested in describing the critical regime towards strong localization, diffusion theory can still be used in order to search for differences to the classical diffusion of photons. Doing so, van Tiggelen et al. [30] present a self consistent approach that ends up in a rescaled diffusion coefficient that can be written as

$$D = D_B \left(1 - \frac{\mu}{(kl^*)^2}\right) \tag{2.49}$$

with D_B being the classical, Boltzmann, diffusion coefficient. The parameter μ is needed to remove short paths that do not contribute to the closed loop from the return probability. This means at the point where the Ioffe-Regel criterion is fulfilled, the value of μ becomes unity, such that no matter how short the path is, there is always a counter-propagating part in order to show constructive interference. This is consistent with a macroscopic population of closed loops as predicted by Anderson.

The same theory was applied to open, finite systems by Skipetrov and van Tiggelen [31, 32]. In the first instance this was done for a quasi one-dimensional geometry [31] in order to explain measurements of multiple scattering of microwaves through a tube filled with metallic spheres. The used formalism was then generalized in order to describe the three dimensional case [32]. This self consistent ansatz is reported to be an improved version of the original self consistent theory of localization done by Vollhardt and Wölfle [33, 34]. The improvement is to allow a position dependence of the renormalized diffusion coefficient which is important in order to describe the boundaries of the sample where photons are able to leak out of the system. Doing so, Skipetrov and van Tiggelen calculate a position- and frequency-dependent diffusion coefficient

$$\frac{1}{D(r,\omega)} = \frac{1}{D_B} + \frac{12\pi}{k^2 l^{*2}} C(\vec{r},\vec{r},\theta) \tag{2.50}$$

using the Green's function that can be calculated by solving the diffusion equation self consistently

$$\left[-i\theta - \nabla D(\vec{r},\theta)\nabla\right] C(\vec{r},\vec{r'},\theta) = \delta(\vec{r}-\vec{r'}). \tag{2.51}$$

This work provides information on the time resolved transmission of photons through a localizing sample as can be seen in Fig.2.16. Here different graphs for the time dependent transmission coefficient are plotted in the same graph. The different curves for $kl^* = 0.7$ and 0.6 are shifted upwards for clarity. Those curves can be compared with experimental data obtained by time resolved transmission experiments.

Skipetrov calculated the time dependent diffusion coefficient in the long time limit (i.e. for $t \gg t_D$)

$$\frac{D(t)}{D_B} \sim \frac{t_D}{t}, \tag{2.52}$$

which can be compared with time resolved transmission measurements. However up to now there is no data available in order to compare the full curve presented in Fig.2.16 with measurements. The problem is that computer simulations for multiple scattering samples that will be presented in section 5.2 exceed the required computer-power because there are too many steps to be calculated. At this point a lot of effort is taken in order to improve the numerical method in order to compare the theoretical calculations with experimental data which will be introduced in the experimental section of this work.

2.6 Faraday Effect

For a medium which shows the signs of localization introduced in the last sections, such that the diffusion of photons comes to rest, it can still be questioned if this

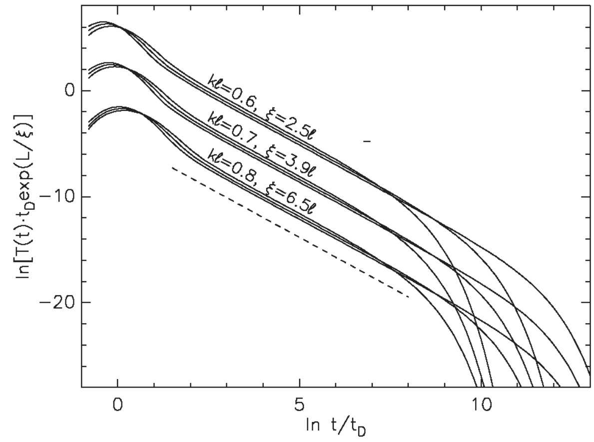

Figure 2.16: Time dependent transmission coefficient T(t) of a 3D disordered system in slab geometry. The curves were calculated using a self consistend approach done by Skipetrov. The curves for $kl^* = 0.7$ and 0.6 are shifted upwards. The parameter ξ corresponds to the localization length of the system.

behavior has its origin in constructive interference on time reversed paths. In order to obtain information on the origin of the non-classicality one is interested to suppress constructive interference on time reversed paths. This can theoretically be achieved by inelastic scattering, relativistic effects or magneto-optic Faraday-rotation. The first two possibilities cannot be realized since the scattering in all cases of the presented work has to be elastic, and relativistic effects are not achievable in a common laboratory.

It has however been shown [35, 36] that the Faraday-effect is able to reduce the enhancement of the backscattering cone. The Faraday-effect leads to a rotation of the polarization of the photons in a certain direction, such that the counter propagating polarizations are rotated out of phase. This is possible, because the theorem of reciprocity does not hold in the case of Faraday-rotation of linearly polarized light.

In principle one can understand the Faraday-effect as a magnetically induced birefringence for circularly polarized light along the direction of a magnetic field $\vec{r}$. This leads to different refractive indices for different helicities of the light parallel to the magnetic field which creates a phase-shift α. The phase-shift is linear in the magnetic field and proportional to a material specific constant V, the Verdet constant. The phase-shift for circularly polarized light with the helicity $\sigma = \pm 1$ then calculates as

$$\alpha = \sigma V \vec{B} \cdot \vec{r}. \tag{2.53}$$

2.6.1 Faraday Effect and the Principle of Reciprocity

In order to obtain (2.53), a method following Bequerel will be introduced. For a more detailed description and a microscopic explanation of this effect one can refer to [37, 38].

A external magnetic field has an effect on the electronic orbits, such that the frequency is changed by the Larmor frequency $\omega_L = e/2mB$. In a rotating coordinate system a circularly polarized light "sees" a frequency $\omega \pm \omega_L$. Using Lorentz's model this difference in frequencies leads to different dielectric constants for different helicities σ of the light wave.

Let us now consider a linearly polarized light wave inside a Faraday-active material. With a magnetic field B along the axis of the wavevector the light can be separated into two circularly polarized waves. As explained before the two waves experience a different refractive index which leads to a rotation of the linear polarization inside the medium. Since the rotation is due to the magnetically induced differences of refractive indices the principle of reciprocity no longer holds. This can be understood from the fact that the medium looses its invariance with respect to the direction of the external magnetic field. This behavior is illustrated in Fig.2.17 using linearly polarized light, which is reflected by a mirror. The angle of the linear polarization is α after passing the Faraday-active medium. The reflection on the mirror changes the direction of the wavevector and the lightwave enters the medium again. The change of the wavevector also changes the helicity of the lightwave, such that the angle of rotation is increased to 2α after the medium. This concept can be used to create an optical diode, which for example is used to protect optical equipment from reflected light.

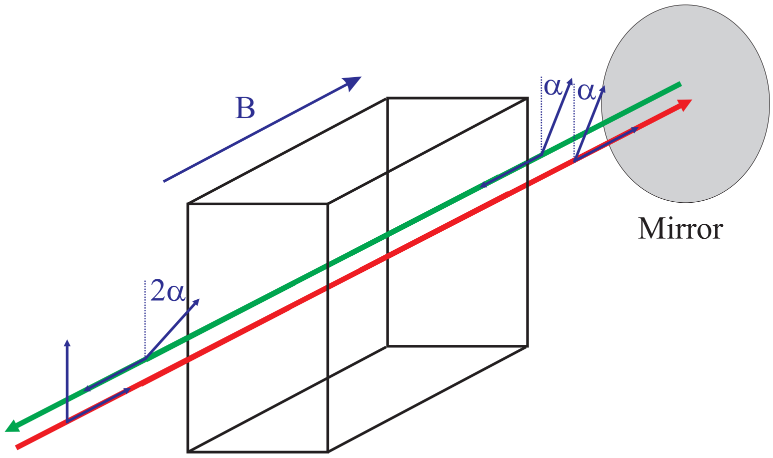

Figure 2.17: The linearly polarized light passes the Faraday-active material which lead to a rotation of the polarization of α. The wavevector of the light changes when reflected on the mirror. This changes the helicity of the light. Therefore the polarization is turned further away in respect to its original direction leading to a net rotation of 2α after passing the material again.

2.6.2 Faraday Effect in Multiple Scattering

The principle of reciprocity plays a crucial role in order to achieve a twofold enhancement in the origin of the coherent backscattering cone. It has been shown that the Faraday-effect can be used to destroy the coherent backscattering cone due to the break of the time reversal symmetry [36, 39]. The simplest theoretical approach in order to explain this effect on the coherent backscattering enhancement is the spin-flip model introduced by John and Mackintosh [35]. This model is able to explain the effect qualitatively. For a more precise treatment of the Faraday-effect on multiple scattering media one has to calculate the scattering matrices using Mie-theory, which is time consuming. Since the aim here is to observe a possible reduction of a localization effect, the spin-flip model is able to deliver the right order of magnitude if this reduction is observable.

Now consider a righthanded, circularly polarized light-wave entering a multiple scattering Faraday-active material. In analogy to the optical diode the light is detected in backscattering direction with the same helicity. Along a scattering channel γ the helicity is able to perform an uncorrelated jump to its opposite value i.e performing a spin-flip. The coherence between the path γ and $-\gamma$ is conserved. If the magnetic field is parallel to the incident beam, the light is affected by Faraday-rotation between the uncorrelated spin-flips which leads to random phase shifts between the scattering events. After n scattering events, the phase difference can then be obtained to be

$$\begin{aligned} \Delta\alpha_F &= \sum_i^n l_i \left[\sigma_i V\vec{B}\cdot\vec{e_i} - \sigma_i V\vec{B}\cdot(-\vec{e_i})\right] && (2.54) \\ &= 2VB\sum_i^N l_i\sigma_i\cos(\theta_i). && (2.55) \end{aligned}$$

The unit vector $\vec{e_i}$ points in the direction of the wavevector of the light. An average over all the n scattering events in one path is analogous to a projection of the unit vector on the magnetic field $\vec{B}$ given by $\langle\cos(\theta)\rangle$. For a large value of N one obtains $\langle\Delta\alpha\rangle = 0$ meaning there is no mean rotation of the polarization.

The mean square difference of the rotation, $\langle\Delta\alpha^2\rangle$, however is finite and given by:

$$\langle\Delta\alpha^2\rangle = \frac{2}{3}NV^2B^2\langle l_i^2\rangle. \tag{2.56}$$

For large N and for simplicity's sake the scattering was assumed to be isotropic, such that

$$\langle\cos^2(\theta)\rangle = \frac{1}{4\pi}\int\cos^2(\theta)d\Omega = \frac{1}{3}. \tag{2.57}$$

In order to calculate the value of the mean square of the step lengths an exponential distribution of path lengths $P(l) = 1/l_f^*\exp(-l/l_f^*)$ will be assumed with a new measure l_f^*, which is the correlation length of the Faraday-effect. It can be shown that $\langle l_i^2\rangle = 2l_f^*$ [40]. Although l_f^* is of the same order of magnitude as the transport

mean free path l^*, correlations between the Faraday-effect and a random walk make a difference between those two measures. This becomes important when one wants to study the effect of a magnetic field on multiple scattering quantitatively. Here we try to find out whether the Faraday-effect is able to destroy the effect of nonclassical diffusion. Thus, we only need an order of magnitude estimate of l_f^*, which can be obtained from the experimentally determined l^*.
The mean square of α is then given by

$$\langle \Delta\alpha^2 \rangle = \frac{4}{3} V^2 B^2 s l_f^*, \tag{2.58}$$

where $s = N l_f^*$ is the total pathlength of the photons. One can interpret this formula as follows: The light traveling on two counterpropagating paths with a length s has a phasedifference of $\sqrt{\langle \Delta\alpha^2 \rangle}$ due to the Faraday-effect. This means that one is now able to introduce a characteristic length s_f on which the time-reversal paths loose their ability to interfere constructively. This length calculates as

$$s_f = \frac{3}{l_f^*} \frac{1}{(2VB)^2}. \tag{2.59}$$

This formula gives the order of magnitude of the maximum path length at which the destruction of the localization effect will be observed. It is obvious that for small value of l_f^*, which corresponds to small values of l^* the cut in the coherence of path length needs a very high magnetic field on order of 20-30 Tesla to be able to reduce the coherent backscattering enhancement. However, by performing time resolved transmission measurements the resolvable path lengths are much longer, such that the magnetic fields available are strong enough to destroy the coherence for paths having lengths of the order of one meter. This will be presented in section 5.3 for the samples used here.

Chapter 3

Experimental Setup

As motivated in the chapters above, one has to have a maximum in turbidity in order to fulfill the Ioffe Regel criterion $kl^* \sim 1$. This can be achieved using densely packed scatterers with a high refractive index. As will be shown in chapter 4, the best candidates are compressed dry powders of TiO_2. In order to measure the turbidity, one needs to have a method to characterize the sample. Detecting the angular dependance of the backscattered light is a powerful tool for this purpose. Section 3.1 presents the necessary methods to investigate multiple scattering samples. In order to measure the very small value of their transport mean free path l^*, a new coherent backscattering setup had to be built. This setup allows a precise measurement of the angular dependence of the backscattered light for angles up to 60° with a sufficient resolution at small angles. In order to measure in direct backreflection and to increase the resolution for very small angles close to 0° a CCD method is used in addition, as will be explained in see 3.1.3. A combination of both techniques is able to resolve the coherent backscattering cone with a resolution of $0.02° < 2°$, $0.14° < 10°$ and $1° < 65°$ in both directions.

In order to measure a localization effect there were several attempts that turned out to be unsatisfying. One method was the measurement of the static transmission presented by Wiersma et al. [41]. The decrease in transport due to localization should of course lead to deviations from Ohm's law. In fact Anderson Localization predicts an exponential decay of the transmitted intensity in contrast to the prediction of Ohm's law with a decrease of the intensity as $1/L$ where L represents the sample-length[1]

In addition, van Tiggelen et al. [42] predicted a rounding of the coherent backscattering cone due to a cutoff for long paths coming from photon localization. Unfortunately both static transmission and coherent backscattering techniques are principally not able to distinguish a possible localization effect from the absorption of the sample. In terms of total numbers, both effects simply lead to a reduction of transmitted photons. Since all samples have a certain amount of absorption no matter how pure they are, those methods all failed to unequivocally prove the

---

[1] Here the other dimensions were taken to be infinity.

existence of strong localization.

A method that *is* able to distinguish between localization and absorption is time resolved transmission. As introduced in chapter 2.5 the photon diffusion coefficient D has to be rescaled due to Anderson localization. This means that D is no longer a constant, but is dependent on the length of a photon path inside the sample. A time resolved transmission experiment therefore allows to measure directly the rescaling of the diffusion coefficient. The experimental way to measure of time resolved transmission will be presented in 3.2. A large number of single photon time of flight measurements result in a photon path length distribution allowing to obtain a value for their diffusion coefficient by using diffusion theory. This can be done by fitting a curve relying on diffusion theory to the measurement. Here one has to put in the values of the diffusion coefficient D and the absorption length. Those two parameters can be used relatively independently since the time of flight distribution is dominated by D for small times whereas in the long time limit the value of the absorption length l_a determines the data. Furthermore deviations from that fit can be studied in order to experimentally prove the existence of a critical regime towards Anderson Localization[2].

By combining both measurement techniques one is able to get a value of the energy transport velocity v_e by dividing the diffusion coefficient $D_0 = v_e l^*/3$ through the value of the transport mean free path l^* recorded with the coherent backscattering method. With the use of this, one is able to measure resonance scattering of scatterers having the right dimensions to act as a resonator for photons inside the sample. Resonance scattering as introduced in 5.1 is expected to reduce v_e for the right diameters of the scatterers.

3.1 Coherent Backscattering

As shown in see 2.4 the angular dependence of the reflected light gives direct information on the turbidity of a multiple scattering sample. This is important since one needs to know how close to the Ioffe-Regel criterion[3] the sample is to be able to quantify deviations from classical diffusion of photons. However, existing setups are not capable of resolveing angles high enough to characterize samples approaching the Ioffe-Regel criterion. For samples with $kl^* = 1$, the FWHM of their coherent backscattering cone would be 60° neglecting reflectivity and localization effects that may have an additional effect on the cone shape.

Methods using a beamsplitter and a CCD-camera as first used by van Albada and Lagendjik [2] have a high angular resolution of about 0.01° but a very limited field

---

[2] The technique however is not designed to be able to measure a sample where the most photons are localized. This is due to the fact that the transmission is expected to decrease drastically so that time resolved transmission measurements are not expected to have a signal to noise ratio big enough for an investigation of such samples.

[3] The Ioffe Regel criterion was introduced in 2.5 and predicts a phase transition to a localized state for a transport mean free path to be of the order of the wavelength of the photons.

of view of up to 3°. This limitation is due to the fact that the used beamsplitter and the lens are limited in their aperture. Another method done by Wolf et al. [1] is one that uses a mirror to illuminate the sample whereas the detection is done either by a CCD camera in analogy to the beamsplitter-method or a one channel photo detector moving around the sample scanning the angular distribution of the reflected light. Again the diameter of the lens that images the surface intensity to the far field limits the angular acceptance. If one were to increase the diameters of the problematic optical parts, there would still be a problem concerning the polarization of the incomming light. As presented in 2.4 the highest enhancements of the backscattering cones can be achieved with circularly polarized light. Unfortunately the reflected light would need to pass the polarization optics in a different angle which would change their state of polarization. This leads to a gradient in the polarization state of the detected light which would result in a distortion of the cone shape. To circumvent this problem one would have to use bendable or curved polarization optics.

In order to be able to measure such high angles using circular polarization a scanning technique was chosen and described by Tweer and Lenke et al. [43, 44]. The backscattered light is picked up by a single mode fiber and carried to a photomultiplier. The polarization optics is put in front of the detector assuring it to be perpendicular to the direction in which the light is recorded for all scanning steps. Here the problem is the illumination of the sample, which would have to be mapped with the detection in direct backscattering direction. Approaching this angle of 0°, the illumination is blocked by the detection fiber making it impossible to record the tip of the cone. However we know that the tip is important in order to determine the enhancement factor and therefore the FWHM of the backscattering cone. With Tweer's setup one is able to measure the backscattered light in a range of 0.1° to 35° in one direction only.

A scanning method using a beamsplitter and a photomultiplier was used by Wiersma et al. [45], where both components are rotated off-center while the sample rotation is compensated. This setup is able to measure the cone width to angles ranging from $-6°$ to 20° resolving the cone shape in direct backreflection. The disadvantage of all scanning methods however is the time they need to record the data. The scanning times lie all above 20 minutes. This makes the alignment lengthy because one needs to run the whole measurement in order to perform the next step of alignment. Further problems can arise due to laser drifts during the scanning period or hysteresis in the scanning device itself.

Taking the advantages and disadvantages of the various techniques presented above into account, we decided to develop a new device to be able to resolve the backscattering cone to angles as high as 65° with sufficient angular resolution. The setup should be capable of performing one shot measurements in order to ensure a good calibration in a reasonable time and to circumvent laser drifts during the measuring periods. Furthermore the setup should be able to measure in both directions in order to assure that the cone which is expected to be symmetric around 0° is recorded correctly. Therefore we decided to put a large number of

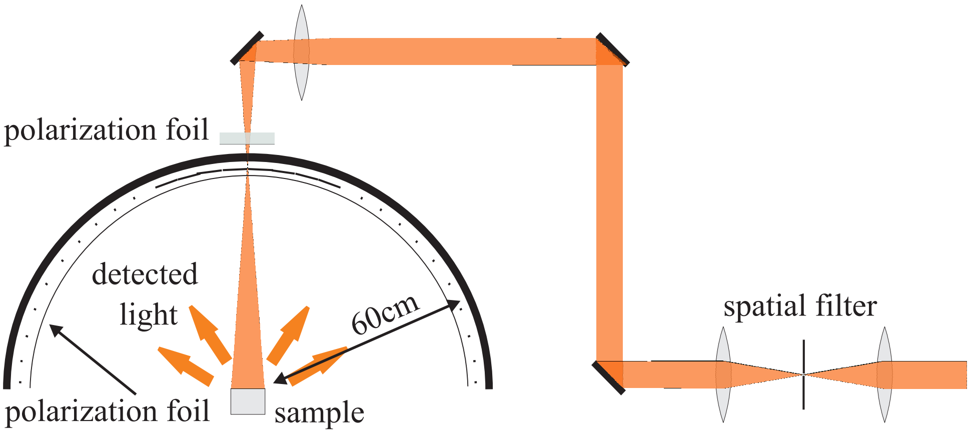

Figure 3.1: Schematic drawing of the custom made setup to measure coherent backscattering. The laser beam coming from a dye laser passes a spatial filter resulting in a gaussian beam profile with a diameter of 1cm. After passing three mirrors the light is focused through a hole drilled in the detection arc in order to illuminate the sample underneath it. The reflected light is collected by 256 photo detectors placed around the arc providing angular resolved information of the backscattered intensity. In order to get rid of light reflected on the sample surface, circular polarization of the incident light is needed. Since such a reflection changes the helicity of reflected light, one is interested in recording photons scattered in polarization conserving channels. Therefore a circular polarization foil consisting of a combination of a linear polarizer and a quarter wave plate, is put in front of the detectors after the incident light is polarized by the same foil.

photo detectors onto an arc placed around the sample illuminated by a focussed laser beam. The setup explained in the following sections is illustrated in Fig.3.1. For more detailed technical information, especially about the electronics and the data processing part of the setup, see the diploma-thesis of P. Gross [46].

3.1.1 The Mechanical and Electronic Setup

The setup consists of 256 photodiodes attached to an arc with a diameter of 1.2 m in order to provide both enough resolution and sufficient light power to be recorded by the photodiodes. The detectors are attached at different distances with respect to each other in order to provide a better resolution for small angles where the gradient of the backscattering signal is bigger compared to high angles where just the incoherent signal is left. For angles ranging from 0.15° to 9.75° photodiode arrays (Hamamatsu S5668) were placed on the arc to be able to maximize the angular resolution. The photodiodes forming one array are 1.5mm apart from each other which leads to an angular resolution of 0.14° close to the backscattering direction. For bigger angles, single photodiodes (Hamamatsu S4011) provide sufficient angular resolution at 1°. Both devices were chosen because of their low dark current in order to maximize the signal to noise ratio. The setup was designed to be able to produce a photocurrent of 0.5μW in each channel when 500mW is shone onto

the sample[4]. Each photocurrent has to be amplified for further processing. This amplification and processing is done using custom designed circuits by M. Clausen [47] for each channel.
The electronics work as follows: A switched integrator (Texas Instruments IVC192) amplifies the photocurrent that is digitized by different AD-converters (Texas Instruments ADS8345 or ADS8344) for the two types of detectors. The digital signal is then collected by an 8-bit microcontroller (ATMEL AT89S8252) and stored. Furthermore the measurement algorithm is running on the microcontroller, allowing communication between the electronics and a personal computer. This computer runs a measurement program to assure the right timing for each channel recording and reading out the data. This parallel method reduces the time to collect the data for one coherent backscattering cone to approximately one second. Because of the short time of a measurement, the setup is comfortable to align since many test-shots can be performed to check and improve the alignment. More importantly, the setup is capable of measuring many more samples in a certain time and makes measurements independent on slowly varying sources of errors like laser- or mechanical drifts of the setup.
In order to average over the speckles produced by the static conformation of scatterers, the sample is rotated. This rotation has to be fast enough, such that the measurement takes much longer than the period of rotation of the sample. For a measurement time of about one second this is easily achieved using an ordinary 12V electro-motor to rotate the sample.

3.1.2 The Optical Setup

As already explained in 2.4 the use of a certain polarization is important in order to be able to measure backscattering cones with a high enhancement factors of nearly two. Therefore one needs to run the experiments using circularly polarized light. Illuminating the sample with this polarization and detecting the light in reflection, where photons pass the same polarization optics again, one is able to suppress photons that are singly scattered on the surface of the sample. Because those photons have no counter-propagating path, they do not contribute to the cone which would lead to an overestimation of the background reducing the enhancement of the tip of the cone. In order to prevent singly scattered light of being detected one has to use a combination of a linear polarizer and a quarter wave plate. When tilting the optical axis of the quarter wave plate 45° with respect to the linear polarizer, circularly polarized light is produced. Reflecting this light on a surface, the helicity changes sign. The quarter wave plate again converts it to linearly polarized light, which however now is perpendicular to the original direction such that this light is suppressed by the linear polarizer. Because of the large number of photo detectors used in this setup one would need to have many linear polarizers and quarter wave plates making the setup very hard to

---

[4] The albedo of the TiO_2 samples is expected to be 99.999%

align and incredibly expensive. This problem however can be circumvented using a circular polarization foil (J53-333, 3M) that was designed to suppress reflection of e.g. a computer monitor. The foil is bendable and combines a linear polarizer with a quarter wave plate as needed for our purpose. It has a transparency of 37% and an astonishingly high wavelength acceptance compared to usual quarter wave plates. The polarizer is able to suppress the reflected light by $> 97\%$ in a wavelength window ranging from 580nm to 620nm which is the window in which our dye laser system is working. The polarization foil was put in front of the 256 photodiodes over the whole detection range so that the optical axis has the same direction for all channels. Doing so, the only parameter that has to be aligned is the polarization of the incoming beam relative to the optical axis of the detection foil.

The setup presented in Fig.3.1 is illuminated by a laser beam with a diameter of 1cm having a gaussian TEM00 mode achieved by using a spatial filter. The light is then guided over three mirrors to the top of the arc where it is focussed through a hole drilled in the metal to illuminate the sample below it. In order to be able to measure a good cone, one has to get the focal point of the light to lie on the plain of the photodiodes, such that the cone is focused back to that area. Due to the active detection area of the photodiodes this focus has an acceptance of 0.5mm, which corresponds to a tolerance of 3cm before defocused light should reduce the quality of the measurements. This is the distance to which the lens should be moved in order to perform measurements maximizing the enhancement of the backscattering cone.

Replacing the sample by a mirror and reducing the laser power drastically one is able to align the optical axes of the polarizing foil placed in front of the hole in the arc parallel to the one in front of the detectors. This is done by tilting the polarizer step by step and minimizing the intensity[5] until a maximum of 97% suppression is reached.

3.1.3 Small Angle Coherent Backscattering

Although the new setup combines many advantages of existing setups it is not free of disadvantages. One major point is the fact that due to the illumination there is no data for angles smaller than 0.15°. This problem however can be solved using an additional beam splitter setup where the light is detected by a CCD camera as presented in ref. [2]. This setup is schematically shown in Fig.3.2 and is able to measure the tip of the same sample up to an angle at 3° with a resolution of 0.02°. The tip can then be manually attached to the measurement at large angles because there is enough overlap of both data-sets within a range of 0.15° to 3°. Combining this technique with the method introduced above, our setup is able to measure the backscattered light with high precision in a range of $-65°$ to $65°$ which makes it a unique tool to characterize multiple scattering samples.

---

[5] This is done by using a very sensitive power meter (Laser Check, Coherent).

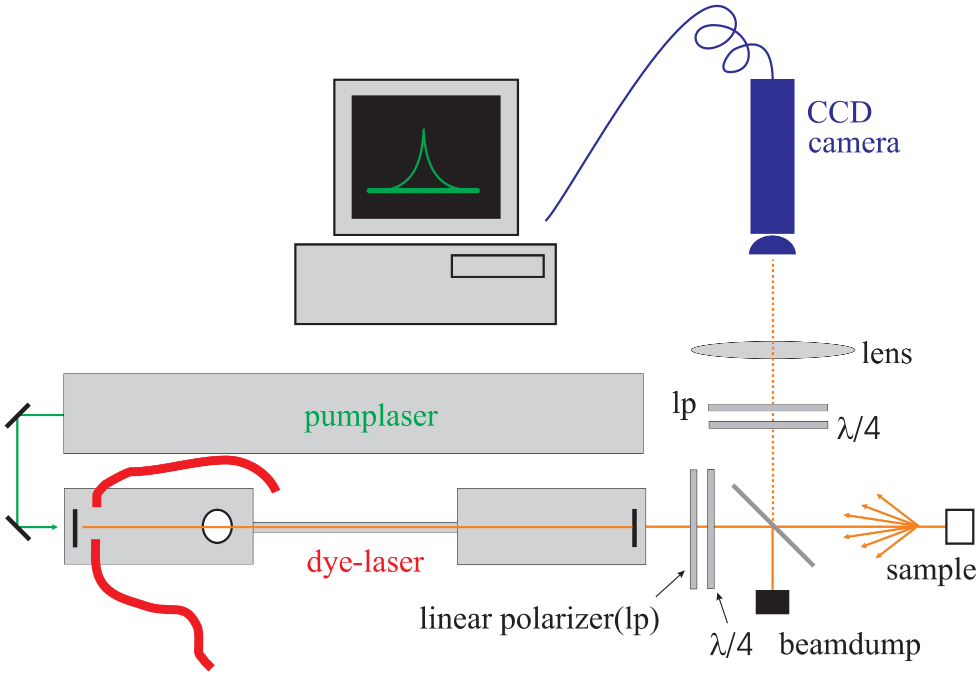

Figure 3.2: Schematic setup to measure coherent backscattering for angles smaller than 3°. The multiple scattering sample is illuminated by a circular polarized laser beam. The light in backscattering crosses a beam splitter and polarization optics in order to get rid of the light reflected at the surface of the sample. This surface intensity is focused to a CCD camera producing a far field image of it. The method allows to add data points to wide angle measurements in order to study turbid samples with excellent resolution.

3.1.4 Calibration and Measurement

Calibration

Using such a large number of photodiodes that are individually connected to different electronic devices it is obvious that there has to be an intensity calibration in order to get channels providing comparable signals. This is done using the backscattered light from a teflon block as a reference. The used teflon block has a value of l^* of about 200μm resulting in a cone with of 0.03° at a wavelength of 590nm. With the wide angle setup the backscattering cone thus cannot be resolved such that only the incoherent signal is recorded. Performing backscattering measurements on this teflon block for 15 different illumination intensities one gets a response curve for every channel independently. These characteristic response curves are shown in Fig.3.3, as can be seen they have a quite linear behavior over the whole intensity range. In order to calibrate each channel a polynomial of second order[6] is fitted to each curve which is then used in further measurements. In

---

[6] The second order polynomial turned out to be precise enough to fit all curves. Fits using a polynomial up to the fourth order did not show any better results so that all reference measurements were performed using the second order fit procedure.

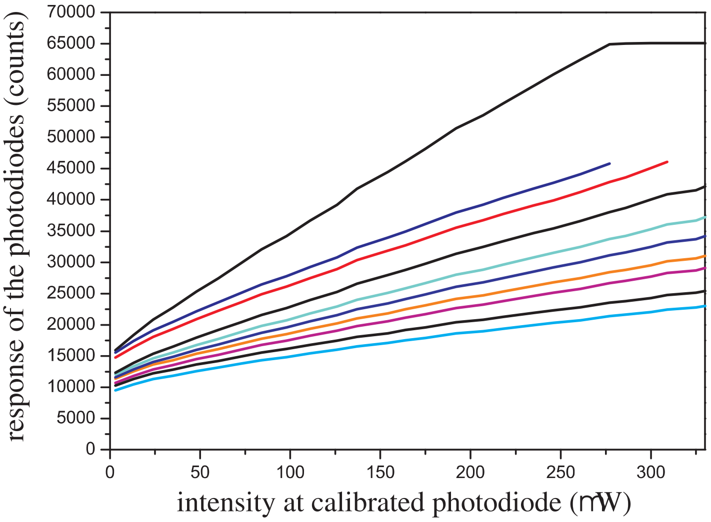

Figure 3.3: Response curves for representative single photo detection channels. Nearly all curves follow the same trend. By fitting a polynomial of second order to the curves one is able to calibrate each channel separately for each channel. There are five curves to differ from the overall behavior. Those channels rely on bad electronics so that those channels had to be ignored in further data acquisition steps.

addition, this method allows a calibration that explicitly takes into account the variation of the integrated background, which is known as Lambert-Beer's law.

Measurements

After the setup is aligned well and the laser works stably, one is able to record data. For each set of data a reference measurement with the same teflon block used in the calibration is taken. This allows to subtract the incoherent background more precisely. In order to maximize the precision of the coherent backscattering cone determination however, the different albedos of the sample and the reference have to be taken into account as well. In both cases, absorption should be negligible, so the difference in albedo will arise from a small residual transmission through the sample (or reference) due to its finite extent. The dimensions of the teflon reference sample are roughly 100 × 100 × 200 in units of l^*. This implies that about 3% of the incoming intensity are lost leading to an albedo of 97%. Our samples typically have dimensions of $10^5 \times 10^5 \times 10^4$ in units of l^*, such that they have an albedo of 99.99%. The difference of 3% in the reference would lead to an overestimation of the incoherent background in the sample by these 3%, which is therefore subtracted manually.
It turned out that averaging over 10 single measurements with an integration time of 800ms delivers good results for all measurements. After recording the reference data the teflon-block is replaced by the sample formed by compressed TiO_2 as will be introduced in section 4. The sample holder, consisting of a cylindrical container

where another cylinder is put in, is designed to allow transmission and reflection measurements. Usually the sample is compressed between two glass plates, one of which can be removed for coherent backscattering measurements. The main reason why the glass plate should be removed is that it leads to reflections of the incident laser light which could damage the detectors. Also due to the different optical thickness of the glass for different angles the reflected light passes the glass plate the cone shape would be distorted due to interference. The cone would have to be corrected for this distortion.

After again averaging over 10 measurements of the coherent backscattering cone this data is divided by the reference data recorded in the first step. In Fig.3.4A the raw-data recorded by the wide angle setup is presented. The blue curve corresponds to the teflon reference sample with an expected cone width of 0.03° which cannot be resolved by the setup. The raw data of the coherent backscattering of a TiO_2 sample (Aldrich) corresponds to the red curve in this graph. There are large variations in the data, since no calibration is done so far at this point. As can be seen, most fluctuations are the same between the sample and the reference, such that a calibration should take care of them. Furthermore the channels are plotted on the x-axes in terms of diode-number and not the corresponding angle. Sorting the channels and taking the intensity calibration into account, one obtains the coherent backscattering cone shown in Fig.3.4B. One can see that the enhancement reaches a value of C_0 =0.95 meaning that the singly scattered light is suppressed very well by the polarizing foil and a very small amount of background light[7] is

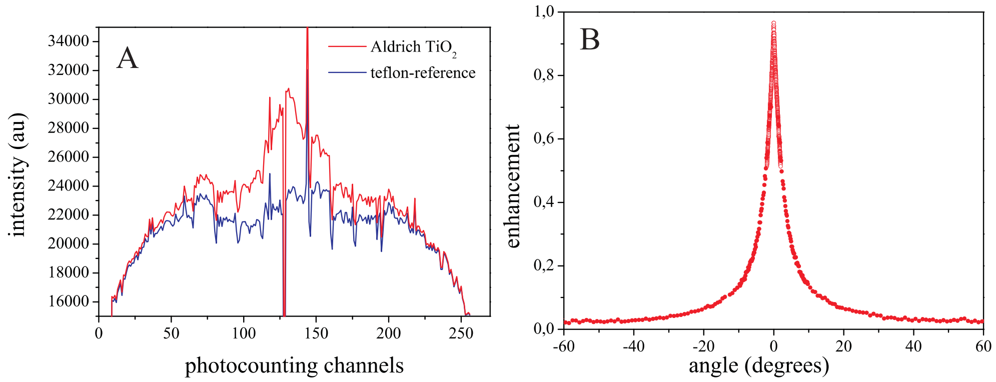

Figure 3.4: A typical measurement of a coherent backscattering cone. A shows the raw data recorded by the 256 photodiodes. The blue curve corresponds to the incoherent background of a teflon sample. Here the FWHM of the coherent backscattering cone is expected to be 0.02° so that it cannot be angular resolved by the wide angle setup. The red curve is the signal of a TiO_2 sample (Aldrich). The raw data has to be processed using an intensity and angle calibration in order to show the right shape of the coherent backscattering signal. Dividing the calibrated TiO_2-curve by the reference measurement one gets the coherent backscattering cone as presented in B.

---

[7] This light is expected to come from the illumination of the laboratory or the stray light coming from reflection and scattering on optical components.

collected by the photodiodes.

3.2 Time Resolved Transmission

In order to search for a deviation from classical diffusion which is expected to be a sign for a localization of photons one needs a method where the different photon path lengths are recorded. The first sign of a deviation from classical diffusion is expected to occur for long photon paths inside a sample. As already mentioned in 2.3 those paths correspond to very small angles in the coherent backscattering cone making it very hard to unambiguously identify any effect on the shape of the cone by those paths. To be able to measure a path length distribution on our multiple scattering samples we use a single photon counting method [48, 49].

3.2.1 The Optical Setup

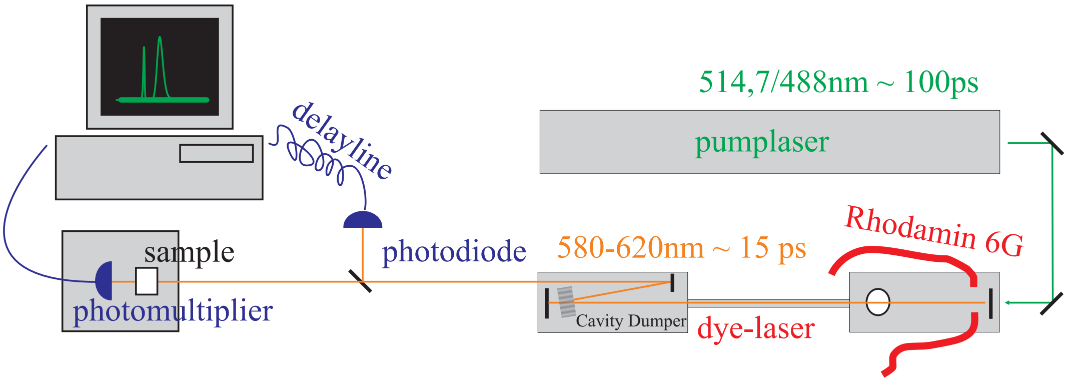

Figure 3.5: Schematic drawing of the time resolved transmission experiment. The dye-laser is pumped by an Ar^+ laser in order to produce pulses having a width of about 20ps. The cavity dumper is able to release pulses with a repetition rate of up to 10MHz. The pulse illuminates the sample placed in front of a photomultiplier which creates a signal to start a time measurement. This measurement is then stopped by a small intensity of the same pulse illuminating a reference photodiode. In order to be stopped by the same pulse a delay line had to be put after the reference diode. By recording a large number of those single photon measurements one gets a time of flight distribution corresponding to the path length distribution of the photons traveling through the multiple scattering sample.

The setup presented in Fig.3.5 consists of a picosecond laser system and a single photon detection part. The laser system can be separated in two parts a Rhodamin6G dye laser (Coherent 699) pumped by an Ar^+-laser (Coherent Inova400). In order to produce picosecond pulses the pump laser was modified with a mode locker crystal (APE Berlin). The cavity of the dye laser had to be enlarged so that both cavities have exactly the same length which is necessary to achieve a synchronization of both lasers in order to produce sub millimeter (picosecond) pulses. The enlargement also includes a cavity dumper (APE Berlin) which is needed to release the picosecond light pulse from the laser cavity. Aligned properly, the dye laser system is capable to produce pulses of a width of about 20ps with a repetition rate of up to 10MHz in a wavelength window ranging from 580nm to 620nm. For measurements using smaller wavelengths, the light of the pump laser can be used. Doing this, one is able to measure at 514nm and 488nm which are laser lines for the Ar^+-laser where pulses with a a width of ∼100ps are still good enough to perform measurements.

About 98% of the light pulse are used to illuminate the sample placed in front of a photomultiplying tube (H5784,Hamamatsu) capable of measuring single photons. The samples have to be turbid[8] and thick enough so that not more than every tenth pulse triggers a counting event inside the photomultiplier, which is important in order to avoid bias in the time of flight distribution. It assures that only one photon is detected during every measurement cycle and dead times of the detector do nor lead to the missing of counts at late times. Setting the cavity dumper to a repetition rate of usually 1MHz the count rate should not exceed 10^5 counts per second which is easy to achieve since one is interested in very thick and turbid samples. Considering this, the thicknesses of the samples are chosen in order to be characterized in a reasonable time so that typical count rates of 10^3 to 10^4 were realized. Using the signal of a counting event a computer starts a time measurement, which then is stopped by a reference signal from a photodiode. This photodiode is illuminated by $\sim 2\%$ of the laser power extracted by a beamsplitter. In order to circumvent errors that may come from small deviations in the time the cavity dumper releases the pulses there is a delay line after the photodiode such that each single photon measurement is started and stopped by the same pulse. Using this technique one is able to measure the pathlength distribution with a temporal resolution of down to 100ps.

In order to be able to measure with high precision for times corresponding to long photon paths one needs to get rid of an artificial broadening of the pulse due to the used electronics and the limited suppression of the afterpulses by the cavity dumper. This device is able to suppress afterpulses up to a factor of 200 which means that their signal is still far above the noise level of the measurement being usually a factor of 10^4 lower than the signal as shown in Fig.3.6A. In order to distinguish both effects and make the measured pathlength distribution comparable to diffusion theory one needs to deconvolute the time of flight signal with a time distribution where the photons do not pass a multiple scattering sample. An illustration of a typical measurement and the data processing is presented in Fig.3.6. First of all a time of flight measurement in absence of a sample is done to obtain information about the pulse shape which the laser is capable of producing in order to have a reference measurement shown in Fig.3.6A. Then the grey filter that

---

[8] The turbidity represented by the l^* as explained in 2.4 is a bulk property that cannot be changed within a large range by the sample preparation. However by compressing the powder one is able to avoid cracks and short circuits for photons. Those would lead to a tremendous increase in the transmission of the sample and change the optical properties by a high amount making it impossible to perform reproducible measurements on them.

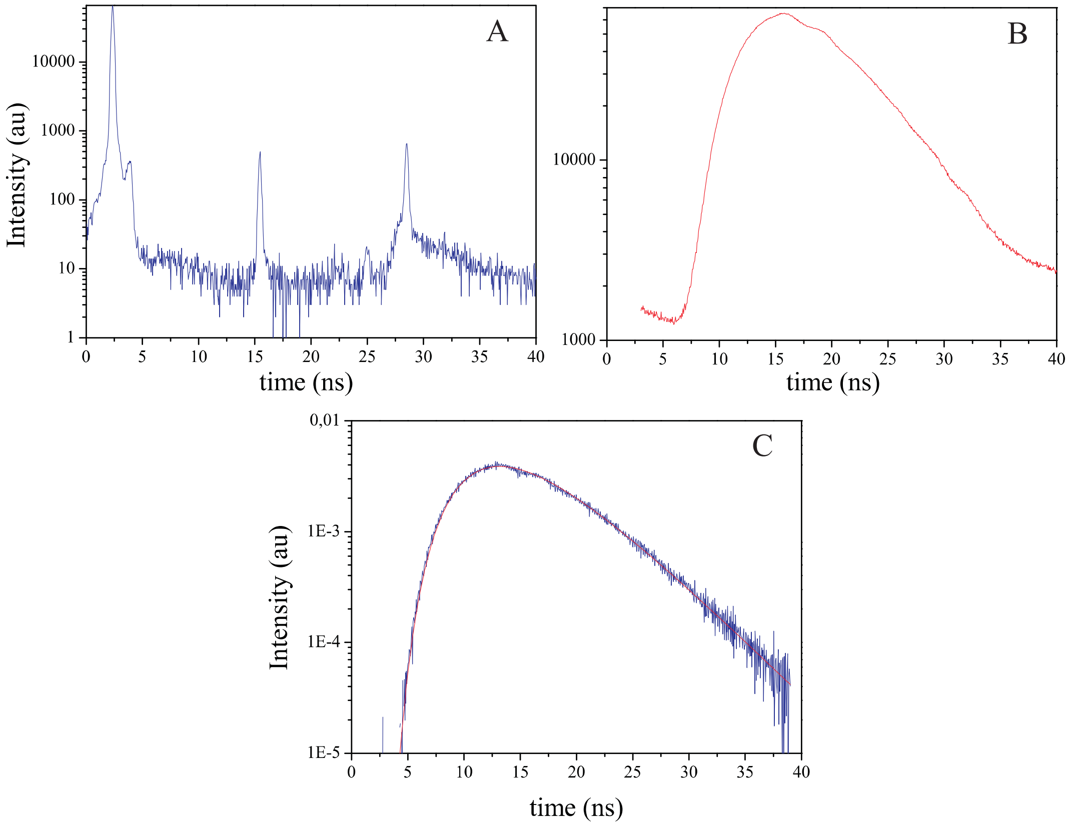

Figure 3.6: Illustration on how the raw data resented in A is processed to end up as a time of flight distribution. One can see two curves in A the red one is the reference measurement in absence of a sample. The red curve is the time of flight measurement with a sample put in front of the photomultiplier. The baseline of the time of flight is two orders of magnitude above the noise limit of the reference measurement. This results because both curves correspond to different integration times. The measurement is stopped when one channel of the 1024 has more counts than 65000. Therefore the broadened pulse measurement corresponds to a longer integration time explaining the higher noise level. The time of flight measurement is bumpy due to fact that the incident light is not a delta pulse. Deconvoluting the measurement with the reference run one is able to get rid of the effects of the illumination in order to investigate the optical properties of the sample using diffusion theory.

prevents the photomultiplier from getting too much intensity is replaced by the sample in front of the photomultiplier. The time of flight distribution (Fig.3.6B) is recorded until the statistics are good enough. Looking closer at the time of flight raw data one immediately sees a noise level that is about a factor of 100 above the one recorded in the reference measurement. This is because the recording software is counting until one channel reaches its maximum which is 65536 counts. Due to the fact that the recording time with a sample in front of the detector is about 100 times longer the higher noise level is not surprising anymore. This measurement usually takes up to three hours which means that about 10^8 single photon measurements contribute to such an experiment assuming a typical count rate of 10^{-2}MHz. In a further step the data and the reference pulse are transformed into Fourier space and the time of flight data is divided by the reference data and transformed back. This data then can be compared with diffusion theory as shown by the solid line in Fig.3.6C which. The fit parameters of the theoretical curve give information about the diffusion coefficient and the absorption length of the sample.

3.3 Time Resolved Transmission Inside a Magnetic Field

To measure the effect of the Faraday-rotation on time resolved transmission one needs to perform the measurement-technique introduced in the previous section inside a magnetic field. Due to the fact that it was not clear at the time when this experiment was planned how big the needed magnetic field would be we decided to use a super-conducting magnet (OXFORD Instuments) which is able to create fields up to 20T. The required field-strength to destroy the localization effect is dependent on both the path length on which the coherence has to be destroyed, and the Verdet constant of the multiple scattering medium. Another quantity, which is not known exactly is the Faraday transport mean path l_f^* which can however be estimated to be of the order of the transport mean free path l^*. Taking all of these uncertainties into account, the required magnetic field calculated following (2.59) has to be between one and ten Tesla.

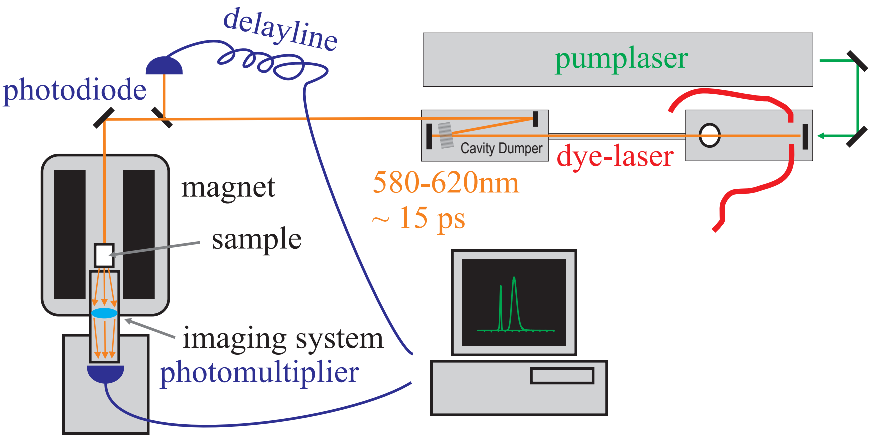

Figure 3.7: Experimental setup for time resolved transmission inside a magnet. The sample is put into the bore of a super-conducting magnet which has a diameter of 40mm. The detector is placed 0.5m behind the sample to reduce the effect of stray-fields on the photomultiplier. Because of the loss of signal due to the distance, the surface intensity at the backside of the sample is imaged onto the light sensitive area of the photomultiplier.

The schematic setup is shown in Fig.3.7 which is basically the same setup presented

in the previous section. The light that comes from the pulsed dye-laser-system discussed in section 3.2.1 illuminates the sample inside the magnet which is accessible through a cylindrical bore with a diameter of 40mm. The detector is positioned underneath the coil in a distance of 0.5m to keep the stray field at its position as low as possible. The photomultiplier is placed inside a black box to shield it from the background light of the laboratory. The box is connected to the bore of the magnet by a brass cylinder. In order to maximize the intensity incident on the detector an imaging lens was put in this cylinder. The lens creates a 1:1 image of the surface intensity onto the light sensitive area of the photomultiplier at the back of the sample.
With a distance of 0.5m away from the highest magnetic field, the stray-field at the position of the photomultiplier is still 50mT (at a magnetic field of 18T). This affects the performance drastically. Therefore one has to shield the detector from the stray-field using a combination of iron and μ-metal foil. Both materials have advantages which can be combined to achieve a maximum of shielding. The iron foil has a large hysteresis, which means that a relatively large magnetic field is needed to achieve saturation, whereas the μ-metal has a very high permeability μ_r, meaning that the field-lines are guided inside the material very well. Therefore the shielding was designed with a double cylinder of a diameter of 50mm made out of iron and a μ-metal case, which directly surrounds the photomultiplier. The schematic of the shielding can be seen in Fig.3.8.

In order to quantify the effectiveness of the shielding, the photomultiplier was put in the magnetic field and illuminated by the laser without a sample. It turned out that the pulse shape is not affected by the presence of the magnetic field, but the count rate of the photomultiplier is. For an increasing magnetic field the count rate of the detector strongly decreased. The behavior of the photomultiplier is illustrated in Fig.3.9. The green curve shows a very fast decay of the measured signal in the absence of the shielding. It that case, at a magnetic field of six tesla

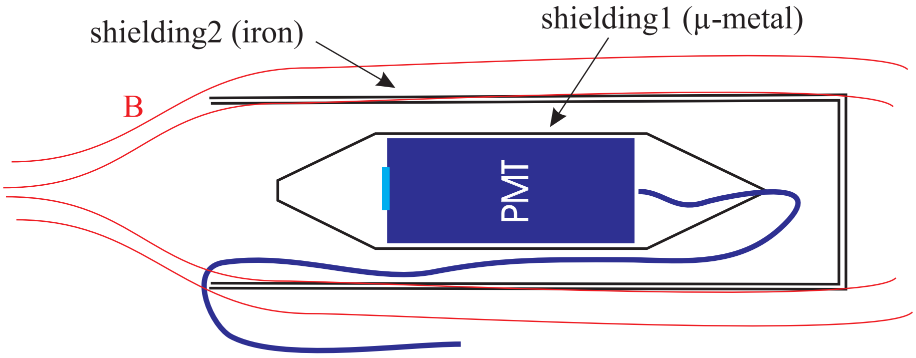

Figure 3.8: The detector has to be shielded from the strayfield of the magnet. Therefore a twofold shielding is practicable. There are two iron cylinders, which have a high saturation-field. In order to reduce the field inside the cylinders they are closed on their backside. The remaining magentic field is shielded by a μ-metal case placed directly around the photomultiplier.

the count rate is decreased by a factor of three. With such a low count rate measurements are unfeasible because the whole detector is placed 0.5m away from the sample which already decreases the intensity at the photomultiplier by a factor of 10. When shielded, the decrease starts relatively flat for small magnetic fields and approaches the behavior of the unshielded case at higher fields. Therefore one still has 80% of the count rate compared to zero tesla for a doubly shielded detector at a magnetic field of six tesla before the decrease starts. One can see that for very high magnetic fields the doubly-shielded case leads to a smaller countrate as in the unshielded case. This can be understood by considering the fact that both, the iron and the μ-metal are saturated in that case, leading to an increase of the magnetic field near the detector. With this setup one is able to perform measurements of the Faraday-effect on time resolved transmission using magnetic fields up to six tesla in order to have enough signal required for good quality measurements. Those measurements will be presented in section 5.3. Calculations presented there will also show that a magnetic field ranging between one and two tesla should be enough in order to destroy the coherence on the path-lengths that show non-classical diffusion. The sample will be the commercial TiO_2 powder R700 mixed with CeF_3-Particles having a diameter of 10nm, such that they are able to fill the space between the larger TiO_2 pigments. For more details on the sample and the first preliminary experiments on the influence of the Faraday-effect on localizing

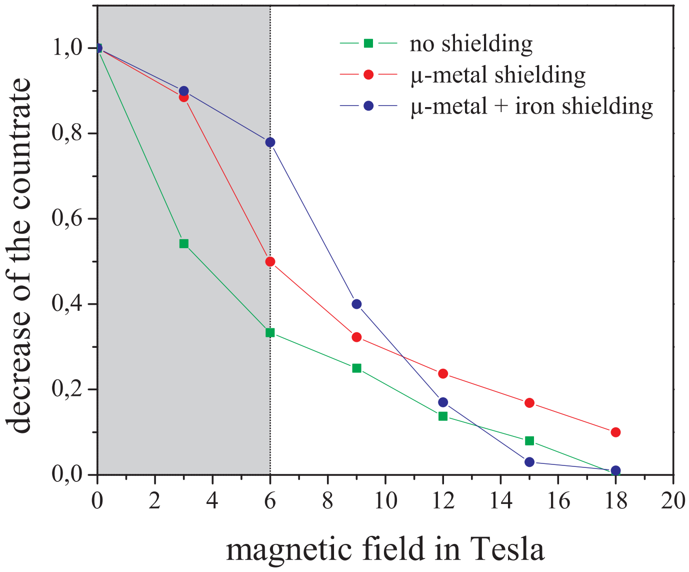

Figure 3.9: Measurements qualifying the shielding. Here the photomultiplier was illuminated by the laser without a multiple scattering sample in front. The green curve represents the relative countrate as a function of the magnetic field in the absence of the shielding. One can see that it is decreasing very fast. Using the μ-metal casing alone, the strong decrease starts to occur at a higher magnetic field. A combination of an iron cylinder and the μ-metal casing leads to a shift of the strong decrease to higher magnetic fields. Considering the loss in countrate, with this double-shielding it is expected that measurements up to six tesla are feasible.

samples see section 5.3.

Chapter 4

Multiple Scattering Samples

The choice of the right samples is very important in order to search for localization of photons. A simple criterion for the transition to localization is given by Ioffe and Regel as already explained in section 2.5. For independent scatterers l^* is simply given by $(\sigma\rho)^{-1}$, where σ is the scattering cross-section and ρ the particle density. Thus l^* can be minimized by using a sample that consists of single particles with a very high refractive index packed closely together. For the close packing necessary to achieve very small l^* however, the independent scatterer approximation no longer holds such that correlation effects need to be taken into account as well. This will be explained in this section in detail as well as effects of resonances in the scattering cross-section which influence the choice of particle sizes. Because one expects a deviation from classical diffusion to occur for long paths the samples also need to have very large absorption lengths. One therefore also has to minimize the amount of impurities in the scatterers. The absorption length corresponds to a distance on which the probability to detect a photon decreases by a factor of 1/e.

In 4.1 the concept of using Mie-resonances is introduced in order to reach a maximum in turbidity for a multiple scattering sample. For very dense samples the right particle-size combined with a certain volume fraction leads to an decrease of the transport mean free path such that both, the values of the form factor $F(q)$ and the structure factor $S(q)$ have to be taken into account. A very important measure of a sample in order to achieve the maximum turbidity is to know the effective refractive index of the medium including the scatterers. However, at volume fractions exceeding 50%, scattering would take place at the holes rather than the particles, such that this limits the usability of increasing the volume fraction to certainly below 50%. In section 4.2.1 Garnett's approach in order to calculate this refractive index will be introduced. This is an analytical approach valid for scatterers with a diameter much smaller than the wavelength of the photons. Using the formulae introduced in 4.1 the best candidates for a small value of l^* are Mie-scatterers due to their achievable form- and structure factors. In order to be able to calculate the refractive index of the matrix surrounding the particles, a numerical method has to be used. This energy-density coherent potential approximation (ECPA) relies on a work by Busch and Soukoulis [53] and is explained in section 4.2.2.

In order to control these important properties of the samples experimentally, it is necessary to be able to perform a characterization of the particles. The most accurate measurements in order to obtain the diameters of the scatterers can be achieved using optical methods. In section 4.3, a combination of static- and dynamic light scattering will be introduced. Due to the fact that scatterers we use here are not spherical, show a large polydispersity and tend to agglomerate, these methods however turned out to have disadvantages to characterize our samples. For the multiple scattering properties of the samples, the polydispersity, non-sphericity and conglomeration do not matter. They simply make a theoretical determination of l^* difficult. Unfortunately since the analysis of the single particle light scattering proportion strongly depends on these parameters, a determination of sample properties with these methods is very difficult. To circumvent this problem a characterization method using an electron microscope is used. The size of the scatterers and its distribution can be measured by analyzing microscope images.

In this work the used samples can be put in two categories. The first species of samples are commercially available powders consisting of ground TiO_2. As will be presented in 4.4 these particles are non-spherical and show a rather large polydispersity. The second species are custom made TiO_2 spheres. Using the results of theoretical calculations the idea is to be able to synthesize even more turbid samples with the right parameters of particle size and volume fraction. Their synthesis and characterization will be explained in 4.5. The last section deals with an idea to use core-shell particles or hollow spheres in order to maximize the turbidity of a multiple scattering sample. However it turned out that although the custom made particles tend to have diameters inside the interesting range in order to maximize the turbidity it is very hard to produce them in the needed amounts. Another problem arises from the absorption which is too large in order to achieve photon paths long enough to show a localization effect.

4.1 The Transport Mean Free Path

As already explained in Section 2.2 the scattering mean free path can be calculated as $l_s \sim (\rho\sigma)^{-1}$ where ρ is the volume density and σ the scattering cross-section of the scatterers. Including the Volume V_p and the filling fraction f of the particles, obtains

$$l_s = \frac{V_p}{f \cdot \sigma}.$$

Since V_p and f are independent values and therefore easy to control experimentally the complicated property is the transport cross section σ. Its value is dependant on the single scattering behavior as represented by the form factor $F(q)$ and the way the scatterers are placed described by the structure factor $S(q)$ [7, 87]

$$\sigma = \frac{\pi}{k^2} \int_0^\pi F(\theta) S(\theta) \sin(\theta) d\theta. \tag{4.1}$$

When dealing with Mie-scatterers one has to take the anisotropy parameter $\langle \cos(\theta) \rangle$ into account as well. This parameter writes as

$$\langle \cos(\theta) \rangle = \frac{\int_0^\pi \cos(\theta) F(\theta) S(\theta) \sin(\theta) d\theta}{\int_0^\pi F(\theta) S(\theta) \sin(\theta) d\theta}. \tag{4.2}$$

Combining both relations one ends up with a transport mean free path

$$l^* = \frac{l_s}{1 - \langle \cos(\theta) \rangle} = \frac{4\pi}{3} \frac{R^3}{f\sigma(1 - \langle \cos(\theta) \rangle)}. \tag{4.3}$$

Both the form- and structure factor are dependent on the wavelength of light. Furthermore the wavelength is changed by an effective refractive index that has to be taken into account when scatterers approach each other. At this point the refractive index of the matrix becomes higher which makes it important to include this effect into the calculations as will be shown in the next sections.

4.2 The Effective Refractive Index

As motivated above, the effective refractive index of a multiple scattering sample affects the values of both the form- and the structure factor which determines the transport mean free path. Thus this property has to be taken into account as well. Furthermore, the reflectivity of the surface of the scattering medium is influenced by the refractive index. For time resolved transmission measurements this medium is glass, whereas for coherent backscattering experiments there is air in front of the sample. This reflectivity is expected to have an effect on the backscattering signal as explained in 2.4 which has to be taken into account in a data processing step.

One simple approach is to linearly interpolate the refractive indices between the scatterers n_{sc} and the one of the matrix n_m surrounding the scatterers using the boundary conditions that for a volume fraction of $f = 0\%$ $n_{eff} = n_m$ whereas for $f = 100\%$ $n_{eff} = n_{sc}$. This leads to an effective refractive index of $n_{eff} = f n_{sc} + (1 - f) n_m$ for the effective medium. This is however a very rough estimate. An approach that gives better results for scatterers will be introduced in the following section.

4.2.1 Garnett Effective Refractive Index

In order to obtain a better estimate for the effective refractive index between the scatterers one can to use Garnett's theory [52], which is an analytical approach valid for small particles or small mismatch of refractive indices. It is able to describe the effective refractive index for Rayleigh-scatterers. This technique is explained in more detail in [8] and calculates the electric fields inside and outside the scatterers with the assumption that the fields are connected linearly. Doing so, one ends up with an expression for the dielectric constant

$$\epsilon_{eff} = \frac{(1-f)\epsilon_m + f\beta\epsilon_{sc}}{1-f+f\beta} \tag{4.4}$$

where β is a term that includes the effects of the different geometries of the scatterers. For spherical scatterers this value is $\beta = 3\epsilon_m/(\epsilon_{sc}+2\epsilon_m)$ which changes (4.4) to

$$\epsilon_{eff} = \epsilon_m \left(1 + \frac{3f\frac{\epsilon_{sc}-\epsilon_m}{\epsilon_{sc}+2\epsilon_m}}{1-f\left(\frac{\epsilon_{sc}-\epsilon_m}{\epsilon_{sc}+2\epsilon_m}\right)}\right). \tag{4.5}$$

Comparing the Garnett effective refractive index with the linear approach shows

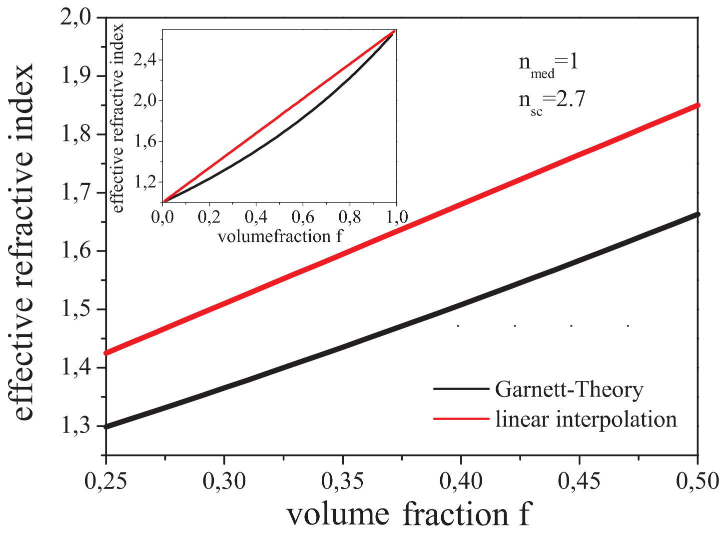

Figure 4.1: Theoretical calculations of Garnett compared to the extrapolation of the effective refractive index of a multiple scattering medium. One can see that Garnett's theory yields smaller values inside the important range of the volume fractions f between 0.25 and 0.5.

that the Garnett values are always below the values obtained from a linear extrapolation. As shown in Fig. 4.1 the biggest differences occur within a range of $25-50\%$ volume fraction. This however is the range where a random packing of hard spheres can be achieved in order to maximize the turbidity of a sample. As mentioned above, the transport mean free path l^* is dependent on the effective refractive index affecting both terms the form- and the structure factor in (4.2). In order to maximize turbidity, one is interested in using the so called Mie-resonances where high values for $F(q)$ (and $S(q)$) for a certain scattering vector q leads to a high transport cross section. Therefore one has to know the effective refractive index very well. However as the Garnett theory is just an analytical approximation valid for small scatterers compared to the wavelength it is not able to give information on densely packed high index Mie-scatterers. In order to calculate the effective refractive index for those types of scatterers, numerical methods have been developed.

4.2.2 Numerical Simulation

As already mentioned in the section above, one wants to use closely packed Mie-scatterers to realize a sample that shows deviations from classical diffusion of photons which is expected to be an indication of Anderson localization. Garnett's approach however is not capable to give information on such samples. In order to be able to theoretically study such objects, numerical simulation techniques have been developed by Busch and Soukoulis [53, 26].
The approach is called Coherent Potential Approximation. In order to calculate the effective refractive index one puts a "testscatterer" out of the sample and calculates its scattering cross section as a function of the dielectric constant ϵ_m of its surrounding. Using the value of the scattering cross-section one is able to calculate a new value for the dielectric constant of the matrix. This represents a self consistent approach that converges to a certain value for the dielectric constant providing information about the effective refractive index of the matrix. The theory however failed to describe media having a small volume fraction. It turned out that the value of the effective dielectric constant would lead to a photon velocity exceeding its speed in vacuum.
In order to describe photons traveling through a multiple scattering medium, the interesting parameter is the speed with which the energy of the photons is transported. Therefore it is self-evident that for the approach described above the energy has to be taken into account instead of the scattering cross-section. This was done by Busch [54, 55] and will be explained in the following section.

Energy Coherent Potential Approximation

The idea of the Energy Coherent Potential Approximation is to pick out one scatterer of the multiple scattering medium and put it into a homogenous medium described by a dielectric constant ϵ_m. This can be done with randomly positioned scatterers as long as they do not overlap[1]. The idea leading to a self consistent technique is to assume that the energy-density is the same for a volume containing a scatterer compared to one without scatterers inside.
This can be written as

$$\int_0^R \rho_{sc} \vec{r} d^3 r = \int_0^R \rho_{eff} \vec{r} d^3 r \tag{4.6}$$

where ρ_{sc} is the energy density of the volume with the scatterer inside and ρ_{eff} the one without the scatterer. The energy-density on the right side of 4.6 can be

---

[1] This assumption is valid because the scatterers used can be considered as hard spheres.

calculated using

$$\rho = \frac{1}{2}\left(\epsilon(r)|E(r)|^2 + \mu|H(r)|^2\right) \tag{4.7}$$

whereas the left hand side of 4.6 is more complicated. For this term one has to take into account that the energy-density consists of two parts: the energy inside the scatterer and the scattered energy in the surrounding matrix. For these two parts one has to solve the problem in full Mie theory explained in detail in [54]. Calculating the Mie coefficients allows one to get a value of the energy density that can be compared to the value affected from (4.7). By changing ϵ_{eff} in order to minimize the differences of both energy-densities this method converges to a value of the effective dielectric constant corresponding to an effective refractive index of the medium.

This Energy Coherent Potential Approximation provides an algorithm to numerically calculate n_{eff} for different samples. The software was programmed by Tweer [43] using C_{++}. It allows a variation of the diameter, the volume fraction and the refractive index of the scatterers. Because the values of the Mie-coefficients have to be calculated in order to get a value of the effective refractive index the programm could be expanded to be able to calculate the expected transport mean free path using the concepts presented in 4.1.

4.3 Sample Characterization Techniques

Apart from these theoretical methods it is also possible to use experimental techniques to characterize multiple scattering samples. One important characteristic to know is the diameters of the scatterers defining the form factor which has a crucial effect on l^* as shown above. The static and dynamic light scattering techniques which will be introduced in the next section use single scattering of photons in order to get information on the size of the scatterers and their size-distribution. Static light scattering measures the angular distribution of the scattered light. This property corresponds to the form factor and provides information on the diameters of the scatterers. Dynamic light scattering uses the fluctuations of the scattered light at a certain angle. These fluctuations can be used to measure the time autocorrelation function which allows one to calculate the diffusion constant of the particles in solution. The diffusion coefficient can then be used in order to calculate the diameter for a given viscosity of the solvent and its temperature. The setup that will be presented in the following section was designed to combine both measurements in one cycle. These optical methods have the disadvantage that they require spherical scatterers where single particles can be kept in solution. When the particles tend to stick together (as is the case for our samples), images using an electron microscope turned out to provide better results in order to record the size of the particles and their distribution.

4.3.1 Single Scattering Techniques

There are two different single scattering techniques. Static light scattering measures the total intensity at different angles, i.e.the form factor. Dynamic light scattering on the other hand uses the fluctuations of the scattered intensity. In order to be able to use such techniques, one needs to ensure that each detected photon was scattered only once. Therefore one needs a very dilute sample to prevent the photons from scattering multiple times. The experimental setup is shown in Fig.4.2, where the sample is illuminated by a focussed laser beam. In order to detect the angular dependance of the scattered intensity, a single mode fiber can be rotated around the sample within a range of 5° to 150°. The light is measured by a photomultiplier placed behind the fiber. This allows a measurement of static light scattering in order to provide information about the form factor of the particles. The setup additionally allows a measurement of the temporal fluctuations of the detected light resulting in the autocorrelation function. This is directly coupled

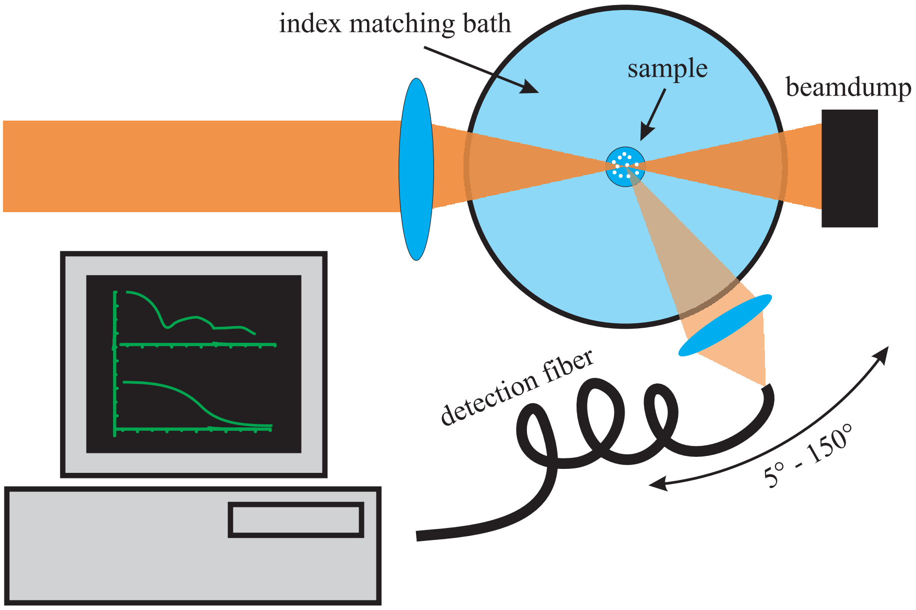

Figure 4.2: Light scattering setup to characterize dilute samples. The illumination is achieved by a laser beam focussed onto a cuvette centered in an index matching bath. The scattered intensity is collected by a single mode fiber. This fiber can be rotated around the sample with a goniometer. The measurement covers an angular range from 5° to 150°. For smaller angels, the divergent laser beam would be detected causing damage to the photomultiplier whereas for larger angles than 150° the detector would block the incident laser beam. Collecting the singly scattered intensity for different angles one obtains a value for the form factor $F(q)$. Parallel to this static intensity measurement, the setup is able to measure the autocorrelation function. Performing a cumulant fit to the autocorrelation function one gets a value of the diffusion coefficient which allows to calculate the diameters of the scatterers. These diameters can be used to fit the form factor recorded in the first step using Mie-theory. A combination of those two techniques is expected to be a good way in order to characterize the scatterers.

to the dynamical light scattering of the particles. Assuming Brownian motion, one is able to obtain a diffusion coefficient of the scatterers, which can then be used to calculate their diameters with the use of the Stokes-Einstein relation. A detailed theoretical introduction to dynamic light scattering can be found in [56]. Combining both static and dynamic light scattering one is able to measure the size and the size-distribution of the particles.

The measurements of static and dynamic light scattering can be done in one run with the ALV TCDLS spectrometer. Cumulant fits on the autocorrelation function using the built in software (ALV-5000) directly give a value for the mean diameter. The cumulant-fit needs an autocorrelation function with good quality. For sufficient accuracy and a good quality autocorrelation function, a certain number of measurements with integration times between 20s and 120s needs to be done.

The data of static light scattering can be analyzed using a program written in MATLAB in order to do a fit to the data using Mie-theory. The software fits the form factor for a size-distribution of scatterers to the experimental curve. Here one can choose various distributions. In order to characterize the custom made samples the most probable size-distribution is a Gaussian as shown in Fig. 4.3B. The technique presented by Bryant et al. [57] was developed to measure particle diameters and their polydispersity used for making colloidal crystals. A measurement of the form factor of a custom made sample is presented in the upper graph of Fig. 4.3. The solid line represents a fit using Mie-Theory with the diameters and a polydispersity as fit parameters. The software also allows a comparison of dynamic light scattering with static measurements for different angles. This is done by taking the diameters obtained by the cumulant fits for different angles. Because the form factor minima occur at different angles for different diameters, one obtains an angular dependence of the diameter as shown in [57]. This combination is a powerful tool which improves quality of the measurement for a small amount of polydispersity. Due to the fact that the polydispersity of the samples that has to be characterized exceeds 10% this possibility is not expected to improve the quality of the measurement. Therefore the measurement will not be presented in Fig.4.3. However, it turned out that this characterization is very complicated in terms of sample preparation. For a measurement presented above, the total integration time was seven hours for an acceptable quality of the data. In addition, not every sample can be prepared well enough for this kind of characterization. The main problem in order to perform light scattering measurements for the characterization is the problem to disperse single particles in a solvent[2]. The scatterers tend to stick together forming clusters which produce unwanted data. Fortunately the clusters tend to sediment to the bottom of the cuvette after a certain time. So it usually takes several hours until the sample is ready to be measured. Reducing the integration time and increasing the number of measurements for each angle turned out to be practical in order to get rid of the data produced by scattering

---

[2] As a good solvent for TiO_2, ethanol or millipore water can be used. Ethanol seems to disperse the particles a bit better, such that in the experiments done mainly ethanol was used

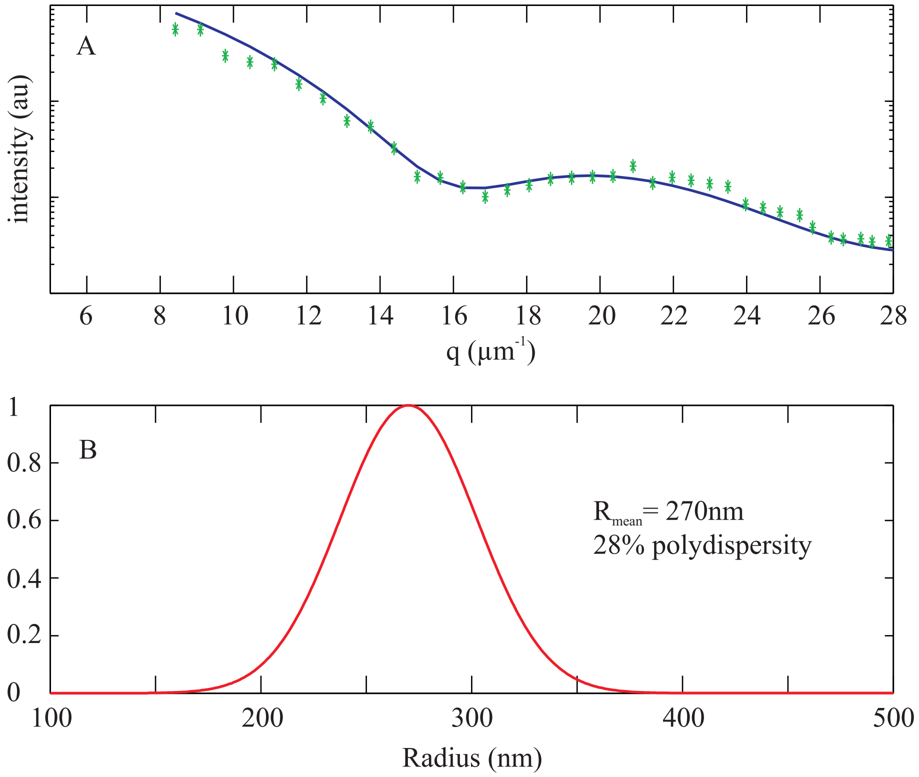

Figure 4.3: Light scattering measurements on custom made particles. The upper graph (A) shows the static light scattering resulting in the form factor $F(q)$. The solid line corresponds to a fit using Mie theory. The lower graph (B) shows the diameters used in the form factor fit. Here, a Gaussian size distribution is assumed.

on the remaining clusters. Unfortunately the reduction of integration time makes it impossible to record a dynamic signal with sufficient statistics in order to be able to perform a cumulant fit.

Another problem that affects the quality of the technique presented above is the fact that for non-spherical particles the form factor cannot be calculated using Mie-theory. Therefore the theoretical fit is just a rough estimate for the real diameter of the particles. As can be seen in the following sections, most particles do not fulfill the criterion of being spherical at all. Because the complicated and time consuming measurement is not expected to improve the quality of the measurements this technique had to be replaced by a characterization using an electron microscope method.

4.3.2 Electron Microscope Imaging

Because of the problems of single-scattering techniques explained above, a scanning electron microscope was used to image the particles and determine their diameters and distribution. The electron microscope is able to make pictures of the surface of a sample that can be used to perform a particle sizing. The main advantage here lies in the fact that the sample-preparation is easy and does not take much time. There is no constraint on the sample in order to collect information of the scatterers.

To increase contrast of the picture by avoiding charge building in the sample one has to cover the surface of the sample with a metallic film. Here the metallic cover on top of the particles is an approximately 10nm thick gold film. This film is put on top of the sample using a gas discharge sputter technique (Scancoat SIX, Edwards). The sample is put on a conducting pad glued on top of a glass slide. This pad has glue on both sides such that the particles stick to it. This glass-slide with the sample on top is now placed under a gas discharge inside a vacuum chamber. The vacuum inside the chamber has to be good enough in order to realize laminar flow resulting in a homogenous gold film. Therefore the pressure inside the chamber is reduced to a value of 1.2 mbar. For a thickness of 10nm one needs to run the discharge for about 40s. After venting the chamber the sample can be taken out and built in the electron microscope. The used device (XL Scanning Electron Microscope, Phillips) focusses an electron beam onto the sample, recording the current of an electron detector in order to measure one point of the picture. Doing this for a large number of points one obtains a surface plot of the sample by scanning the whole area. This method provides a spatial resolution of up to 50nm corresponding to a magnification of $\sim 20000\times$. As an example, Fig. 4.4A shows an electron microscope image of a commercial sample consisting of TiO_2 (DuPont R700) particles. One can easily see that the scatterers are far from being spherical. Measuring the diameters of about 150-200 single particles one obtains the histogram of the diameters of the scatterers presented

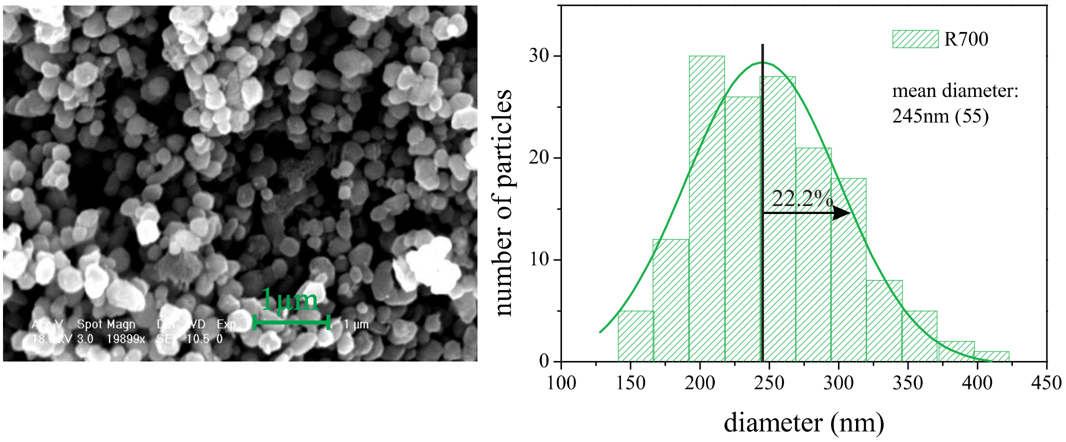

Figure 4.4: The left picture shows a scanning electron microscope image of a commercial TiO_2 powder (DuPont R700). One can see that the particles are non-spherical with a large polydisperstiy. The diameters are plotted in a histogram presented in the right graph. A gaussian fit to this histogram shows the mean diameter of the scatterers to be 245nm with a polydispersity of 22.2% ($\sigma = 55nm$) for this sample.

in Fig. 4.4B. Repeating this measurement for different samples, one is able to collect the desired information having an accuracy not lower than compared to light scattering techinques[3].

4.4 Commercial Samples

Nowadays titanium-oxide is an important material used for different purposes. It is chemically inert and absorbs ultraviolet light. Therefore it is used in sun-blockers. In the visible spectrum it has a huge refractive index, which is why the pigments of white paint consist manly of TiO_2. This material can also be found in toothpaste where the small particles act like grinding stones because of their high degree of hardness.

The pigments are produced form naturally occurring TiO_2 in Australia, USA, India and South Africa. It can also be obtained from ilmenite ($FeTiO_3$), which is more generally accessible for ready extraction with a suction type dredge. These dredges are directly connected to floating wet mills, where the slurry is treated further and the heavy minerals are extracted. The wet mill produces up to 80% heavy minerals with a TiO_2 recovery of 78%. After three spiral stages inside a wet mill, the product is pumped to a land-based stock pile in order to be shipped to a dry mill. Before passing through the dry mill the product is scrubbed using sodium hydroxide, which removes surface coatings of organic and clays from the particles. In the dry mill, the ilmenite is separated using the conductivity of the titanium minerals in high-tension treatment and the higher magnetic susceptibility of the ilmenite. In the end, the dry mill produces ilmenite with a TiO_2 recovery rate of 97%. The final product is cleaned using the so called chloride process. The reaction yields titanium tetrachloride, $TiCl_4$, and the chlorides of all the impurities present. The reaction is exothermic, and accurate temperature control is essential. The mixed chlorides are cooled and the low-volatile chloride impurities (e.g. iron, manganese and chromium) are separated by condensation and removed from the gas stream with any un-reacted solid starting materials. The $TiCl_4$ vapor is condensed to a liquid, followed by fractional distillation to produce an extremely pure, colorless, mobile liquid $TiCl_4$ intermediate product. The second critical stage in the chloride process is the oxidation of $TiCl_4$ to TiO_2 pigment particles. Pure $TiCl_4$ is reacted with oxygen in an exothermic reaction to form TiO_2 and liberate chlorine, which is recycled to the chlorination stage. The high temperature ensures that only the rutile crystal form is produced. After cooling, the gas stream passes through a separator to collect the pigment particles, which are treated to remove adsorbed chlorine from the pigment. The reactor controls the efficiency of the conversion of

---

[3] As already presented in the sections above, the accuracy of single scattering techniques is expected to be orders of magnitudes above the electron microscope. However for the used particles that are not spherical at all and which form clusters, the form factor or the autocorrelation function fitted to the data cannot be calculated with Mie theory. Therefore this light scattering is actually not capable of providing better information than an electron microscope image.

$TiCl_4$ to TiO_2 as well as the particle size and distribution.

The particles produced as explained above fulfill the requirements on samples in order to have a very small transport mean free path together with a very small amount of absorption. They have a high scattering cross-section which can be increased by using scatterers with a high refractive index relative to the matrix surrounding. For our experiments we use pigments from DuPont and Aldrich which they kindly made available. Those TiO_2-particles have a refractive index of 2.7 in their rutile structure. The different types of particles differ in diameter ranging from 230nm to 540nm. This is the range where small values of their transport mean free path are expected when closely packed. As already presented in Fig. 4.4 the scatterers are non-spherical and their polydispersity ranges from 20% to 25%. In Fig. 4.5 there is a table showing the diameter and polydispersities for all our commercially available samples. The data was measured by analyzing electron microscope images as explained above. The commercial powders consist of separate particles and can therefore be compressed to the desired volume fractions rather easily. Another important advantage is the fact that this pigment is a mass product such that we have one kilogram of each pigment available to do experiments with. The amount of material for one measurement is dependent on the transport mean free path and the absorption length and ranges from 0.5 to 1 gram. Thus, there is enough material to perform many test-shots in order to prepare a good sample without having to use the same sample twice. Otherwise one would have to recycle the sample after an unsatisfactory try. This recycling of a sample however implies that a compressed powder has to be dispersed and then compressed again. The particles can either be dissolved in ethanol or water and dried. This method however is very time consuming and would make it unfeasible to greatly vary the values of sample thickness and volume-fraction experimentally in order to find ideal parameters. In addition, there is the danger of getting impurities into the sample while dissolving and drying it. This would lead to a decrease in the absorption length and therefore a loss of reproducability.

	Diameter (nm)	Poydispersity (%)
R101	286	22
R104	311	10
R700	245	22
R706	230	23
R900	359	29
R902	279	38
Aldrich	54	37

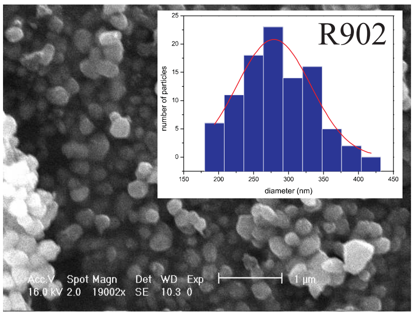

Figure 4.5: Table of the used commercial samples. The particle diameter was obtained by measuring single particle diameters on an electron microscope image as presented on the right hand side. The resulting size distribution was calculated by fitting a gaussian to the histogram of the diameters.

4.5 Custom Made Samples

Although the commercial samples presented above combine many advantages, a lot of effort went into producing samples with custom designed scattering properties. To be able to reduce the value of the transport mean free path one is interested in producing high-index spherical particles with a certain diameter and a small polydispersity.

Another idea to produce particles with even better scattering properties is to use core-shell particles. There, a particle with a low refractive index is covered with a shell having a high refractive index. Computer simulations [43] showed that for the right combinations of core and shell diameters, extremely turbid samples can be achieved. In the next section a method that describes how such particles can be produced is presented. However since the synthesis is quite complicated and time consuming the quality of the scatterers was not better compared to commercially available particles. Especially the amount of absorption was not small enough compared to commercially available powders. Futhermore, it was not possible to grow the shell to the theoretically calculated thickness, such that the scattering cross-section could not be maximized.

4.5.1 Titania Full-Spheres

Titania full-spheres are synthesized by controlled hydrolysis of titanium tetraethoxide in ethanol-salt solution. The concentration of the salt is used as a control parameter in order to tune the size of the nano-particles. The basic idea how to synthesize particles within a range of diameters of 300nm to 700nm was first presented by Barringer et al. [58]. This method however was difficult in terms of its reproducibility. The particles synthesized first showed a very broad size distribution, which could be decreased by adding salt (NaCl or KCl) to the synthesis process [59, 60]. With this method, particle diameters between 800nm and 1200nm could be produced dependent on the salt concentration. Other techniques using polymers [61] or hydroxypropylcellulose [62, 63, 64] in order to stabilize the growth of the particles and prevent agglomeration have been developed. The synthesis of monodisperse TiO_2 nano-particles however turned out to be more difficult compared to latex or silica colloids. Finally S. Eiden and J. Widoniak [65, 66] parallel to Xia et al. [67] managed to produce titania particles having a well defined diameter and a small polydispersity compared to commercial particles.

The reaction is a stepwise hydrolysis of titanium tetraalkoxide to produce titanium tetrahydroxide which undergoes condensation. This eliminated water and leaves titanium dioxide.

$$\mathrm{Ti(OR)_4{+}4H_2O \rightarrow Ti(OH)_4{+}4ROH} \tag{4.8}$$

$$\mathrm{Ti(OH)_4 \rightarrow TiO_2\ xH_2O + (2\text{-}x)\ H_2O} \tag{4.9}$$

with R=Ethyl resulting in

$$\mathrm{Ti(OR)_4{+}4H_2O \rightarrow TiO_2{+}\ 2H_2O\ {+}4ROH.} \tag{4.10}$$

Theoretical calculations using the energy coherent potential approximation expected a particle diameter around 300nm to be interesting in order to achieve a small transport mean free path. Having the right concentrations of the reactants it turned out that a production of such particles is possible. By using 1.25ml of a 0.1M solution of KCl in 250ml Ethanol adding 4.25ml titanium tetraethoxide the synthesized colloids should result in the desired diameters. The salt charges them so that electrostatic repulsion separates the single particles in order to prevent conglomeration resulting in a small polydisperstiy. For a more detailed description about the production of TiO_2 particles we refer to the thesis of Johanna Widoniak [68], where one can get information on how the salt concentration has to be varied in order to produce different sizes of colloids.

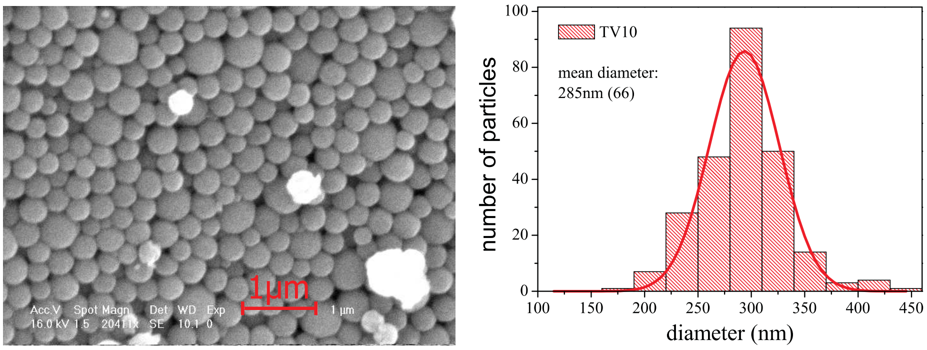

Figure 4.6: The left picture shows a scanning electron microscope image of a typical custom made TiO_2 powder (TV10). The particles are spherical with a small polydisperstiy. The diameters are plotted in a histogram presented on the right-hand side. A gaussian fit to this histogram shows a mean diameter of the scatterers to be 294nm with a polydisperseity of 21% for this sample.

In order to achive a good multiple scattering sample one has to produce about one gram of the colloids. Therefore one needs to do one synthesis twice or three times in order to have enough material. The different syntheses have to be characterized separately before they can be put together.

An important point in order to achieve maximum turbidity besides the diameter is the refractive index of the particles. The colloids formed by the above reaction are in an amorphous phase right after synthesis, corresponding to a refractive index of about 2.4. This value is not high enough for our purpose. The colloids have to be heated up to 1000°C in order to show a phase transition to its rutile crystalline phase where the mean refractive index is 2.8.

Fig. 4.7 (A) shows custom made TiO_2 particles before this calcination process in the amorphous phase. After heating them up, the surface shows a structure formed by crystallites as presented in (B) for the same sample. The size of those crystallites turned out to be another problem in order to produce highly scattering particles. This can be seen in (C) and (D), where smaller particles are shown after having been heated up. The size of the crystallites is about 30nm which is the

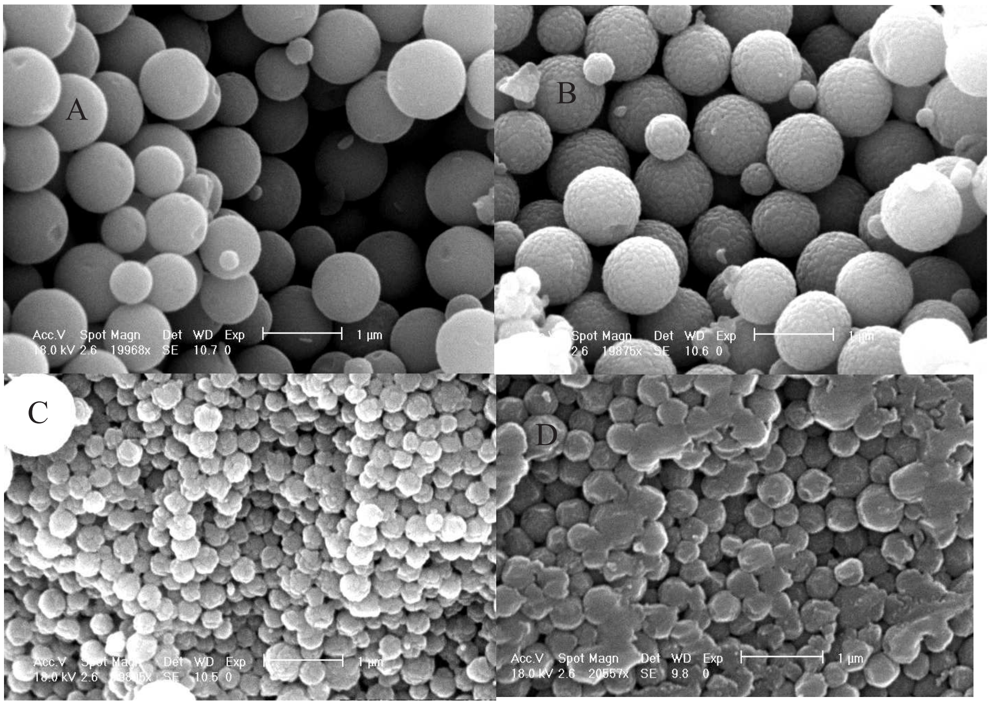

Figure 4.7: Electron microscope image of different custom made TiO_2 particles. (A) shows amorphous TiO_2 spheres that show a surface structure after the calcination process as presented in (B). The crystallite size becomes important for smaller particles, as presented in (C) and (D). Here the particles grow together during crystallization. Those particles cannot be dispersed in a solvent or compressed to the desired volume fractions.

size of $\sim 1/10$ of the whole particle for ideal particle size. This can lead to a conglomeration of the particles. After the calcination process some particles grew together due to the crystallization process as clearly shown in (C) and (D) . This conglomeration does not necessarily have a large effect on the optical properties of the sample. However, such a sponge-like structure cannot be compressed to the needed volume fractions anymore. Thus the transport mean free path could not be reduced to the value expected by theoretical calculations.

Another problem resulting from the heating is the occurrence of an increasing absorption of the particles. Although not fully understood, this absorption is likely to occur when impurities are particular burned due to the high temperature leaving the particles grey. This effect can be reduced by flushing the oven with oxygen. The oxygen is expected to burn away all impurities. It turned out that the absorption could be reduced but there was still some absorption left. Efforts in order to wash away the grey cover by dissolving them in ethanol or water also failed. This is a major disadvantage since a deviation of classical photon-diffusion is expected to occur on the longest paths. Absorption however cuts off those paths, such that the effect is no longer observable.

A lot of effort went into producing good samples using this promising method.

However in spite of this the custom made samples were not able to deliver better results than the commercial powders.

4.5.2 Core-Shell Particles

Another idea in order to produce particles having defined scattering properties is to use so called core-shell particles. Calculations using the ECPA showed that the transport mean free path could be reduced by a factor of three compared to the full spheres. The basic idea is to cover a core having a low refractive index with a high index material.

The synthesis of core-shell particles relies on the work done by Matijevic et al. [69] where silica particles were coated with a TiO_2 layer. Another advantage of this procedure was that the silica cores can be produced with a smaller polydispersity which also reduces the one of the coated particle. This is because the size distribution is dominated by the growth of the particles in an early state of the synthesis. In order to produce those cores a procedure based on Stoeber et al. [70] has been used. The resulting particles were covered by TiO_2 using the same protocol needed for the full spheres with the difference that the silica-cores were put into the ethanol first. The resulting core-shell particles were calcinated to come into the rutile crystalline phase. The problem using this method was the limit in the thickness of the TiO_2-shell around the silica core. For shells thicker than 50nm one had to do the synthesis in two steps. This however turned out to increase the polydispersity and to be difficult in order to achieve thick shells because the thickness increase by one further step became smaller and smaller. Unfortunately there was no significant increase in diameter after three steps. Therefore the ideal diameter calculated using energy coherent potential approximation could not be achieved in both cases.

It turned out that the work to produce such samples is very time consuming and difficult. The synthesis of the cores needs 24 hours in order to grow to the required diameter. Putting the shell around and letting the sample dry took another 12 to 24 hours. The same time is needed for the oven to slowly heat up to 1000°C and down again. Although the oven was flushed with oxygen, which is expected to burn all carbon which might be the origin of the increasing absorption, the custom made particles still turned out to be darker compared to the commercial ones.

Chapter 5

Experimental Results

In the following chapter the experimental results of various measurements on multiple scattering samples will be presented. The used techniques are explained in detail in the chapter 3.

A combination of coherent backscattering on compressed TiO_2 powders with time resolved transmission measurements provides information on the effective speed the photons have on their way through a very turbid multiple scattering medium. For different particle sizes it is expected that there are minima due to resonances in the scattering cross sections which will be explained in section 5.1. It is unclear, if those resonances are needed to achieve values of kl^* small enough, to be able to observe the transition towards Anderson localization.

Time of flight measurements on samples consisting of particles introduced in section 4 turned out to show a deviation from classical diffusion in their long time limit. Those long times correspond to long photon paths on which localization is expected to begin to occur. This is because it is more probable for long paths to form closed loops on which photons are trapped due to interference. This deviation from classical diffusion is larger for samples with a smaller value of kl^* which will be presented in section 5.2. This is consistent with the Ioffe-Regel criterion which demands the value of kl^* to be unity for a transition to strong localization. The measured data allow systematic study of the diffusion coefficient which shows a time-dependence as expected by simple theoretical considerations. With those measurements one is able to calculate the critical exponent of the localization length as well as the critical parameter of the turbidity represented by its value kl^*.

The experimental techniques allow us to independently quantify the value of the absorption- and the localization lengths. Therefore we are able to quantitatively study static transmission. In former experiments one could not make any satisfying conclusion relying on such measurements because absorption and localization were not quantified independently. With our setup we are able to compare static transmission data to theoretical curves without any adjustable parameters.

Finally section 5.3 presents time resolved transmission measurements in a magnetic field in order to prove that the nonclassical diffusion originates from an interference

effect on closed loops. Therefore the sample was mixed with small CeF_3 particles which show a strong Faraday effect and put in a magnetic field. Measurements showed that the deviations vanish with an increasing magnetic field.
A combination of the measurements presented in this chapter represents the first experimental evidence for strong localization of photons. It allows the conclusion that Anderson localization exists and that it is an interference effect which can be distinguished from Mie-resonances.

5.1 Resonance Scattering

The consequences of resonance-scattering on a particle were first investigated by Wigner [73] in 1955. He calculated the scattering properties of a quantum particle in a potential where its wavelengths have the same order of magnitude on the extend of the potential well. He concluded that for this resonant scattering there is an increased dwell time. His theoretical approach is still an object of interest from an experimental point of view. Since the laser became a standard tool, many measurements using photons as scattering particles were performed. For instance using scattering of photons on cold atomic gases Hau et al. [74] and Labeyrie et al. [75] found a reduction in light transport of many orders of magnitude. Other experiments analyzed the resonances of single spheres which are expected to act like a cavity for the resonant photons. Doing this [76], it was possible to create cavities with Q-factors of up to 10^{10} [77, 78]. There are many applications for those cavities like lasers [79] or biological sensing, where spherical cavities are used [80]. Another very important application using a resonance effect would be the realization of photonic crystals [81], where photon-transport comes to a halt due to a band gap in analogy to the behavior of electron in semiconductors. Those photonic band gap materials are expected to revolutionize the photon transport, replacing electronics by photonic devices [82, 83].
When one deals with photon transport through a turbid medium however, it is not clear if one will be able to separate effects of resonance scattering from the signal of multiple scattering. The photons passing the medium can be described by a random walk having a step-length which is given by their transport mean free path l^*. As explained above, the transport can also be treated as a diffusion of photons. It is obvious that the dwell-time induces a reduction of the energy transport velocity v_T no matter if the particles are close together or not [84]. However, resonant Mie-scattering leads to an increased scattering cross section, which lowers the value of the transport mean free path. Small values of l^* again change the transport properties of the multiple scattering medium. When the value of kl^* approaches unity a phase-transition to a localizing state is expected to occur, where photon transport comes to rest. This means that both effects, the dwell-time and non-classical diffusion are expected to reduce photon transport through the medium. The separation of those effects can be difficult but essential in order to be able to

find experimental evidence for the existence of Anderson localization[1].

Time resolved transmission measurements by Drake and Genack [49] reported anomalously low values of the diffusion coefficient D, which were interpreted to be the onset of strong localization. Theoretical calculations done by the Amsterdam Group [85, 86] showed however that resonance scattering indeed is able to decrease the value of the diffusion coefficient by a factor of up to seven. They concluded that the reduction of D measured by Drake and Genack is more likely due to resonance scattering than an indication of strong localization of photons. Furthermore van Albada et al. [84] presented measurements on a single sample showing a reduction in v_T. However, a clear demonstration of the resonances is still lacking. This could be achieved by systematic measurements of the transport velocity v_T as a function of the effective particle size. The effective particle size here means the diameter of the scatterer normalized to the wavelength of the photons inside the scatterer. As already mentioned above, as the particle diameters become of the order of the wavelength, one also approaches the Ioffe-Regel criterion of strong localization.

In order to distinguish the possible onset of strong localization and resonance scattering, a combination of two measurements on the same sample will be presented. In a first step we used the angular dependence of the enhancement of the coherently backscattered light to determine the transport mean free path. The width of this enhancement is inversely proportional to the value of $k_0 l^*$ where $k_0 = 2\pi/\lambda$ is the wavevector of the photons in air, thus providing a direct measurement of l^*. The setup we used for this purpose is presented in section 3.1. In a second step we used time resolved transmission measurements as presented in section 3.5. Such a time of flight measurement which determines the broadening of a picosecond pulse provides information on the diffusion coefficient $D = v_T l^*/3$ inside the sample. Due to the fact that the D and l^* are measured independently it is then easy to obtain the value for the transport velocity v_T. A typical set of both measurements performed on a sample consisting of Ti-Pure (Aldrich) particles is presented in Fig.5.1. On the left hand side the angular resolved reflection is plotted. From a fit to the curve using the theory of Akkermans et al. [23] one obtains a value of $k_0 l^* = 6.3$. This fit has to be corrected for internal reflections on the surface of the sample as already explained in section 2.4. The correction can be calculated using the energy coherent potential approximation [26] in order to obtain a value for the effective refractive index of the medium. The jump in the indices of air and medium correspond to a reflectivity which can then be taken into account.

The right hand side presents a time of flight measurement through the same sample, which had a thickness of 2.21mm. A fit to the data provides information on the important scattering properties like the diffusion coefficient D and the absorption length l_a. The peak of the curve allows a determination of the value of the diffusion coefficient $D = 22\frac{m^2}{s}$ whereas the long time limit is dominated by the absorption length $l_a = 2.6m$. The measurements presented above can be repeated

---

[1] The effect of Anderson localization will be treated in the next section

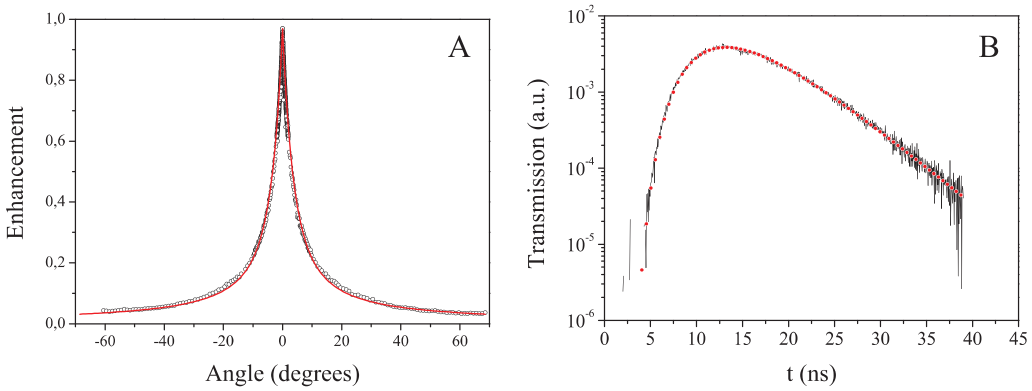

Figure 5.1: On the left hand side (A) there is a plot of the angular dependence of the coherent backscattering from a sample with a length of $L = 2.21$mm consisting of Aldrich's TiPure particles. From the full width at half maximum the value of kl^* can be determined. At the used wavelength of 590nm a theoretical fit including the effect of the surface reflectivity yields $kl^* = 6.3$. The right hand side (B) a time resolved transmission measurement an the same sample is shown. The dotted curve is a fit to the data using diffusion theory. The peak position as well as the behavior for long times allow a determination of both the diffusion coefficient $D = 22\frac{m^2}{s}$ and the absorption length $l_a = 2.6m$ almost independently.

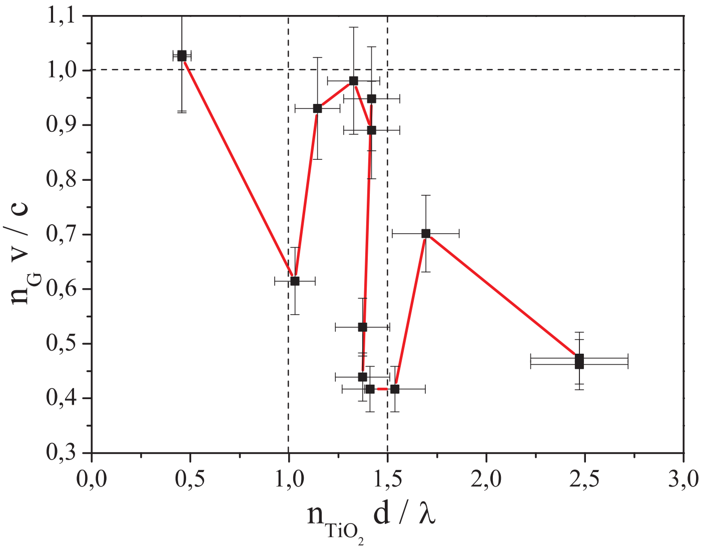

Figure 5.2: Measurement of the normalized transport velocity $n_G v_T / c$ in the effective medium as a function of the effective particle size. Here the effective refractive index was obtained using Garnett's approach. For multiple of half the wavelength the effective transport velocity shows minima which are consistent with the simple geometrical picture of a standing light wave inside the particle.

for different effective particle diameters d/λ, both by using different species of particles and changing the wavelength of the light. Doing so, one obtains a dependence of the relative transport velocity v_T on the effective particle diameters, presented in Fig.5.2. In order to study the effect of resonance scattering the effective speed of light was multiplied by the corresponding effective refractive index n_G calculated using Garnett's theory. When resonance scattering doesn't occur the value of $n_G v_T / c$ is expected to be unity independent on the effective particle size. The curve in Fig.5.2 shows such a behavior for some values whereas there is a clear decrease of the transport velocity for effective diameters at multiples of half the wavelength. The graph is plotted in a way, such that one can understand the reduction of v_T due to resonance scattering by a simple geometrical picture when a standing wave is formed inside a particle for the right particle diameters. Due to the polydispersity of the samples[2] one cannot expect sharply peaked resonances.

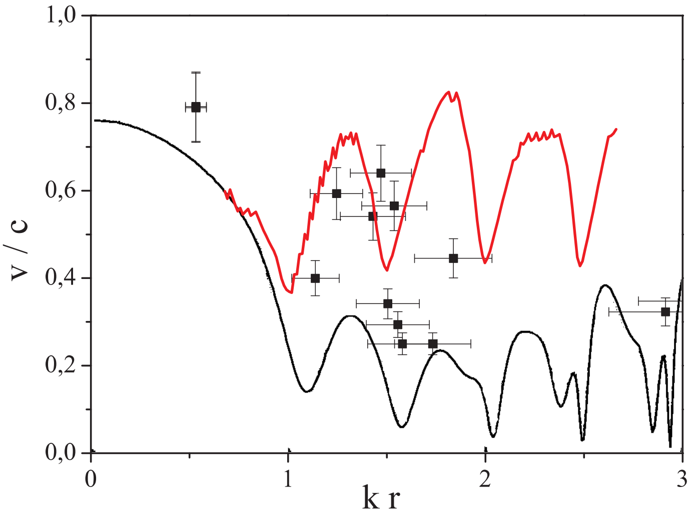

Figure 5.3: The same set of data presented in Fig.5.2 can be compared to theoretical calculations done by van Albada et al. (black) and ECPA (red). The measured data lie between the two curves showing minima consistent with both theoretical approaches. The calculations by van Albada had been carried out for a refractive index of the particles of 2.7 and a volumefraction of 36%. All measurements were performed on samples having volumefractions around 40% which were slightly bigger. The measured data was corrected for those differences.

In order to compare the data with theoretical calculations done by van Albada et al. [84] the same set of data is presented in Fig. 5.3. Here the value of v_T / c is plotted over the size parameter kr where $k = 2\pi/\lambda$ is the wavevector and r the radius of the scatterer. The calculations had been carried out for a refractive index of the particles of 2.73 and a volume fraction of 36%. All measurements were performed on samples having volume fractions around 40% which were slightly bigger. Different volume fractions are expected to lead to a small shift of the whole curve, such that the difference could be canceled out by small corrections[3]

---

[2] The polydispersity of the used particles is about 20% which is considered by the error-bars.

[3] Those corrections become necessary due to the fact that the value for r is theoretically obtained over the volume fraction $r = f^{1/3}/2$ of the system. Therefore we corrected the radii

on the measured data-set. The red curve in Fig.5.3 corresponds to calculations of the refractive index using the energy coherent potential approximation introduced in section 4.6.

One can see that there is qualitative agreement of the measured data with both theoretical curves. The minima for small size parameter have the same position for all three curves. The behavior for bigger size-parameters also matches the tendency given by theoretical calculations. The data of the measurement lies between the values of the calculations done by van Albada and ECPA over the whole range of the graph. The values of ECPA are bigger and the van Albada-curve lies below the measured values. This is probably due to the fact that the theory of van Albada does not take into account that there are correlation effects which start to become important in the limit of high packing fractions. Such correlation effects are expected to increase the transport mean free path in respect to the value obtained by the independent scattering approximation reported by Fraden and Maret [87]. This treatment of the scatterers as independent leads to an overestimation of the effective refractive index of the medium which can be seen in Fig.5.3. A better way to tread the effective refractive index is the ECPA-approach which shows a better agreement to the measured data.

Due to the fact that the data is in reasonable agreement with the theoretical treatment, one can conclude that the reduction of the transport velocity between the resonances is due to the effective refractive index of the medium. Another reason for a quantitative deviation could be due to nonclassical diffusion, which a few samples showed also in the absence of resonances.

In this section direct measurements of the diffusion coefficient and the transport mean free path on various multiple scattering samples show a reduction of the transport velocity for particle diameters having multiples of half the wavelength. The reduction of v_T of up to a factor of five can be interpreted by the dwell time of a standing light wave inside the scatterers. The measurements could be compared with two different theoretical approaches showing a qualitative agreement. The measurements clearly show that resonance scattering can be separated from the effect of Anderson localization and that small values of the the diffusion coefficient [49] cannot be seen as an indication of Anderson localization. A different signature of Anderson localization will be discussed in the next section.

5.2 Nonclassical Diffusion

As already explained in section 2, photons entering a dense medium consisting of scatterers at random positions, are scattered multiply on their way through the medium. The trajectory of a single photon can be described by a random walk, which can be treated as diffusion for many scattering events. The important mea-

---

of out data sets by a factor of $(f/36\%)^{1/3}$ where f is the measured volume fraction in order to compare it to the theoretical curve.

sure one is interested in when looking at photon diffusion is the mean square displacement $\langle r^2 \rangle$ of a photon-cloud. This value grows with time, which was already described by Einstein [50] in 1905. A famous consequence of this is Ohm's law, which describes the transmission of e.g. electrons through a conducting medium. The transmission is inversely proportional to the length of the medium. Taking the wave nature of the photons into account, there is however the possibility that the photons show constructive interference on time reversed paths. Because of this interference, the photons have a higher probability to stay on a closed path, which is expected to reduce the photon transport. In 1958 Anderson suggested the destruction of diffusion to be the origin of the metal-insulator transition, which earned him the Nobel Prize in 1977. For a critical amount of turbidity the number of closed loops is expected to grow, such that more and more photons are localized and do not contribute to diffusion anymore. This critical amount of turbidity is quantified by the Ioffe-Regel criterion, which states that the transport mean free path l^* has to be of the order of the wavelength λ of the scattered photons.

Approaching the Ioffe-Regel criterion, the diffusion coefficient is expected to become scale-dependent, which is explained by Abrahams et al. [6]. For strong localization, the photon cloud stops spreading[4] which is consistent with a diffusion coefficient that decreases towards a value of zero.

Anderson localization was experimentally studied in [88] with electrons, however since electrons are charged, they are able to interact with each other and they can be bound in potential minima, such that they do not contribute to the transport anymore. It is therefore virtually impossible to distinguish between trapped and localized electrons, which makes the study of Anderson localization using electrons open to interpretation. Therefore the use of photons provides many advantages: They are not charged nor can they be bound in potentials. When one is able to measure the amount of absorption, which is always present in measurements, all deviations from classical diffusion which show the expected scale-dependence of the diffusion coefficient have to be due to localization. In addition, measurements using the Faraday-effect to destroy interference on closed loops is able to prove the existence, that the nonclassical Diffusion really is an interference-effect.

5.2.1 Time Resolved Transmission Measurements

In the last twenty years, there were many efforts to observe strong localization using visible [89, 90] and infrared light [91] in order to discover deviations from classical diffusion. Schuurmans et al. were able to produce samples with a value of $kl^* = 3.2$ which were promising to show nonclassical diffusion of photons traveling through them. Unfortunately experiments with those samples mainly focussed on static transmission. Such a transmission measurement performed by Wiersma et al. [41] presented a decay of the photon intensity of a sample with a length L

---

[4] This can be quantified by the mean square displacement, which becomes constant for strong localization.

faster than $1/L$. Unfortunately the effects of absorption, which are always present in multiple scattering samples and show the same reduction of the static transmission as localization, could not be ruled out as pointed out by Scheffold et al. [92, 93] and Chabanov et al. [94].

Time resolved transmission experiments as introduced in section 3.2 allow the separation of the effects of localization and absorption. Such measurements were subsequently carried out on samples with similar values of kl^*. However, they did not show any deviations from classical diffusion [90] further questioning the previous evidence of the existence of Anderson localization.

There were also studies on microwaves, which were scattered on metallic spheres inside a cylinder, where deviations from a classical behavior of the time resolved transmission signal was found [95]. Unfortunately, due to the geometry it was not possible to doubtlessly interpret the very small deviation as an onset of strong localization. The sample had a geometry of 2 x 2 x 20 in units of l^*, which makes it a quasi-one-dimensional medium. As localization is always present in a 1D and 2D geometry [6], the deviations cannot be interpreted in terms of the 3D case, where Anderson localization is a phase-transition, with a critical value of $kl^* \sim 1$. Therefore those quasi one dimensional measurements are not able to unequivocally proof the existence of a transition to Anderson localization.

Here, we use ground TiO_2 powders which form a sample that has the dimensions $10^5 \times 10^5 \times 10^4$ in units of l^*. As already presented in section 4, the extremely small amount of absorption of those powders allows such large samples. Since the samples have huge dimensions, the absorption has to be treated very carefully when comparing the measured data to diffusion theory. Fortunately the values of the diffusion coefficient D and the absorption length can be determined relatively independent. This is because the short-time part of the time of flight measurement is dominated by D, whereas the absorption length has its major contribution in the long time limit of the curve. In addition this procedure is able to detect deviations of time resolved measurements from classical diffusion, because localization and absorption lead to different functional forms of the tail. For a classical diffusion the long time limit is dominated by the exponential decay of the absorption. Localization would lead to a non-exponential form of the tail [97, 99] as already explained in section 2.5.

In order to avoid artificial broadening of the time of flight signal, a measurement without a sample between the laser and the detector is needed. Therefore, one has to be careful not to shine too much laser power into the photomultiplier, which was achieved by using grey-filters such that the count rate has the same value when the filter is replaced by the sample. After the time resolved transmission data are recorded, we deconvoluted them with the calibration measurement in Fourier space. Fig. 5.4 shows the path length distribution for samples consisting of different particles. The full line corresponds to diffusion theory, where the parameters of D and l_a were chosen such that the theoretical curve fits the data best. The dashed line shows the absorption length, obtained from the fit to the data. The values of kl^* were recorded with the same samples using coherent backscattering

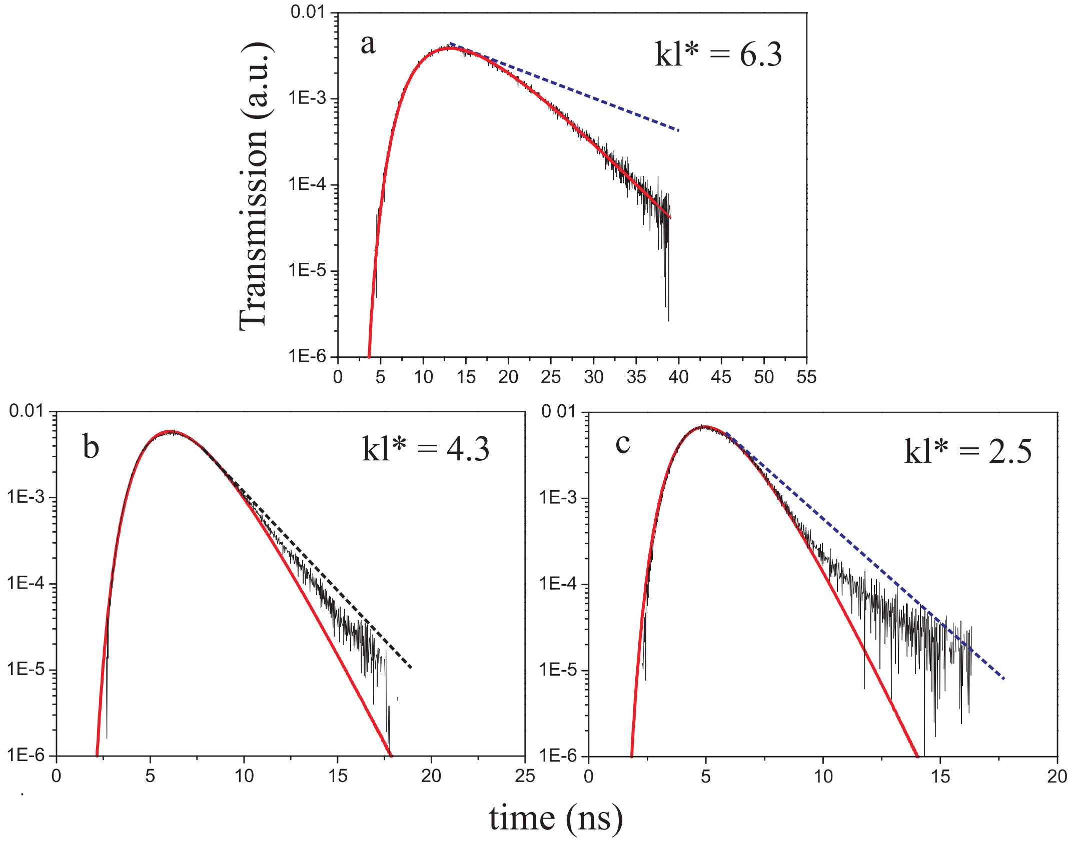

Figure 5.4: Time of flight distribution from a Ti-pure, R902 and R700-sample. The experimental curves were compared with diffusion theory including absorption (red line). In (a) one can see that the measured data of a Ti-Pure sample (L=2.5mm, D=22m^2/s, l_a=2600mm, n$_{eff}$=1.28) closely follows the theoretical fit. The curve presented in (c) represented a R700-sample (L=1.48mm, D=15m^2/s, l_a=340mm, n$_{eff}$=1.55) which shows clear deviations from the exponential decay in the long time limit. This deviation can be interpreted as a time dependence in the diffusion coefficient. An intermediate case in shown in (b) which was obtained from a sample consisting of R902 particles (L=1.51mm, D=13m^2/s, l_a=380mm, n$_{eff}$=1.23), where small deviations from the classical fit can be observed. The respective values of the absorption length obtained by the diffusion fit to the curves are indicated by the dashed lines.

introduced in section 3.1.2.
Ti-Pure (a), which has the largest value of $kl^* = 6.3$, follows the diffusion theory closely, whereas the time of flight curve of R700 (c) shows clear deviations from the theoretical curve in the long time limit. The R700-sample thus shows a non-exponential decay for long times, where the photons stay inside the sample longer than expected for a purely diffusive process. This deviation is consistent with the concept of local scaling theory as proposed by Berkovitz and Kaveh [99]. All time of flight curves are normalized such that the total transmission cannot be read out of Fig. 5.4. In fact, the countrate of each single experiment decreased for a smaller value of kl^* in the same sample geometry, which was compensated for by longer

integration times.

There could be other reasons, which might lead to a non-exponential decay in the long time limit of the path-length distribution. One possibility would be a distribution of l^*-values in the sample, which would lead to a diffusion coefficient that is not constant. In order to eliminate this possibility a time of flight measurement on the same sample was performed, however with the transport in the opposite direction. Such flipped sample would show a different effect if there were a gradient of turbidity leading to a spatially varying D.

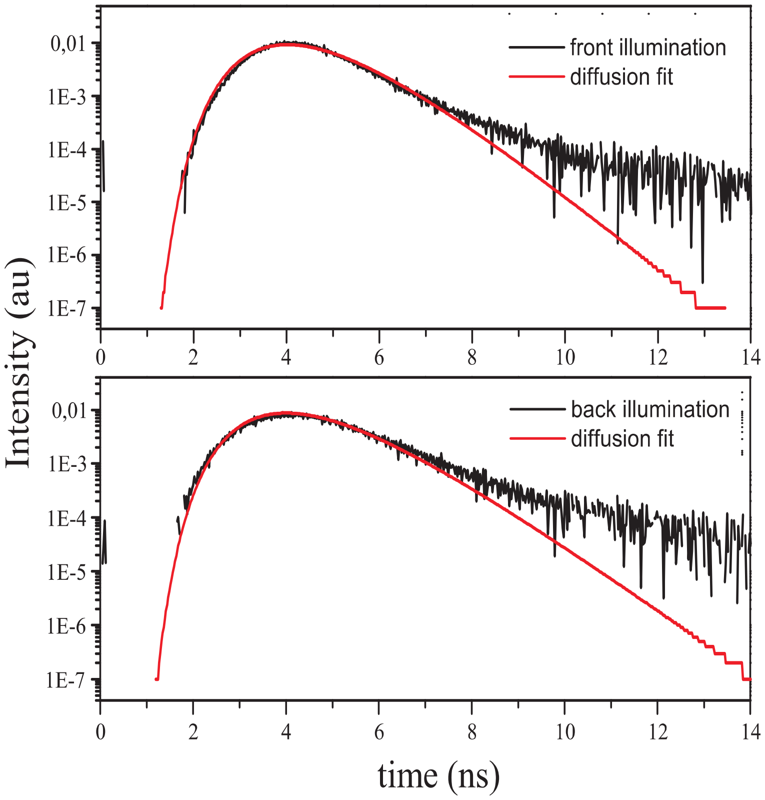

Figure 5.5: Measurements on a R700-sample illuminated on both sides in order to eliminate the possibility that the deviations from the diffusion fit rely on a gradient of the transport mean free path. Such a gradient would be possible for stratifications inside the sample. For a flipped sample, one would expect to measure the opposite effect if there was a gradient in l^*. The fact that both curves show the same longtime behavior indicates that the non-exponential decay is not due to stratifications.

Fig. 5.5 shows the measurements on R700 where the sample is flipped. One can easily see that both curves have the same longtime behavior, such that a stratification can be ruled out for these samples. The differences in the two curves arise from the sample-holder which is not symmetric. The distance to the detector was larger for the lower graph, such that the count rate was slightly smaller due to the loss of photons on their way from the sample-surface to the photomultiplier.

Another possibility to measure such a longtime behavior is simply a high amount of background counts. One can think of photons, which are possibly able to get to the detector without crossing the sample. The effect of such a background illumination in order to create the effect could also be ruled out. Measurements on different sample-thicknesses showed that the nonexponential tail was the same within a range of $L = 1 - 1.5$mm where the count rate changed by a factor of roughly ten.

Finally, fluorescence of the TiO_2-particles might give rise to a long time tail. A small amount of fluorescence could be able to lead to another photon-diffusion behavior, which would be related to the classical photon diffusion. With the right timescales of the diffusion origin from scattering and the delay due to fluorescence one would theoretically be able to create a nonclassical behavior fitting the time resolved transmission measurements. In order to rule out the effect of fluorescence, a time of flight measurement on the most localizing sample R700 was performed with a filter that blocks all wavelengths longer than the initial one. Since the fluorescent light has to have a longer wavelength, the filter is able to block the fluorescent light. The measured time of flight curve shows exactly the same behavior compared to the case without filter behind the sample. Due to the small intensity of the incident laser beam ($\sim$ 10mW cw) a two-photon-process can be ruled out such that fluorescence plays no role in our measurements.

As already explained in section 2.3 the longtime limit of the broadening of a delta-shaped pulse inside a multiple scattering medium is given by

$$I(t) \sim \exp\left(-\left[\frac{\pi^2 D(t)}{L^2} + \frac{c}{nl_a}\right] t\right). \tag{5.1}$$

Any deviation from a non-exponential decay in the longtime limit indicates a temporally varying diffusion coefficient $D(t)$. Now, if Anderson localization reduces the diffusive part of the transmitted photons, one expects that the time of flight measurement is dominated by absorption in its long time limit. This can be seen in Fig. 5.4 where the curves of R902 and R700 approach the dashed lines, which correspond to the behavior when absorption takes place in absence of diffusion.

Considering the long time limit of diffusion, which is given by equation 5.1, it is possible to recalculate the transmission data, such that one ends up with an expression for the temporal behavior of the diffusion coefficient. This can be done by taking the negative derivative of the logarithm of 5.1. The resulting curve is plotted in Fig.5.6. This had to be normalized to $(\pi^2 D(t=0)/L^2 + c/nl_a)$ in order to be able to compare the three different samples presented in Fig. 5.4. Note that all three curves have no direct physical connection to the diffusion coefficient, because 5.1 describes the time resolved transmission only in the long time limit. For times which are twice the time where the most photons leave the sample (t_{max}) the measurement on Ti-Pure approaches unity. This corresponds to a fully diffusive behavior, where $D(t)$ remains constant as indicated by the red line. The other two measurements start to show deviations to the red curve for $t > 2t_{max}$. For R902 and R700 one can see that the value of $D(t)$ becomes smaller than diffusion theory predicts, for bigger values of t indicating a scale-dependence of the diffusion

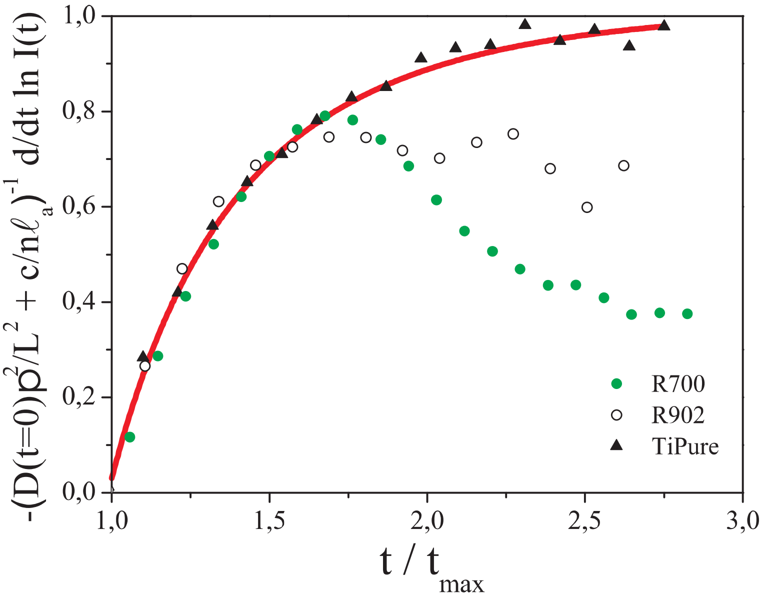

Figure 5.6: Characterization of the dependence of the diffusion coefficient for the three samples presented in in Fig.5.4. The diffusion coefficient was obtained directly from the time of flight distribution by taking the normalized negative derivative of the logarithm of I(t). R700 shows a marked decrease of D in its long time limit in contrast to Ti-Pure, which closely follows the prediction of diffusion theory (red line).

coefficient.

In order to quantify the amount of non-classicality a simple measure is given by the ratio of the experimental data to the diffusion fit. This was done systematically in an interval ranging from t_{max} to $3t_{max}$ and plotted over the value of kl^* taken from the corresponding coherent backscattering measurements. Fig.5.8 clearly shows that the deviations increase when the value of kl^* decreases, which is consistent with the Ioffe-Regel criterion for strong localization.

As already mentioned in the section above, nonclassical diffusion and resonance scattering can clearly be distinguished, because both have different fingerprints. The nonclassical diffusion has its origin in the different path lengths, which are able to form closed loops and not in a reduction of the transport velocity which arises from a dwell time at resonance scattering. Therefore localization changes the functional form of the path length distribution, where the dwell time reduces the value of the diffusion coefficient by shifting the time resolved transmission curve. Furthermore, it turned out that the values of the diffusion coefficients of samples that show nonclassical diffusion are consistent with a value of the transport velocity c/n presented in Fig.5.2.

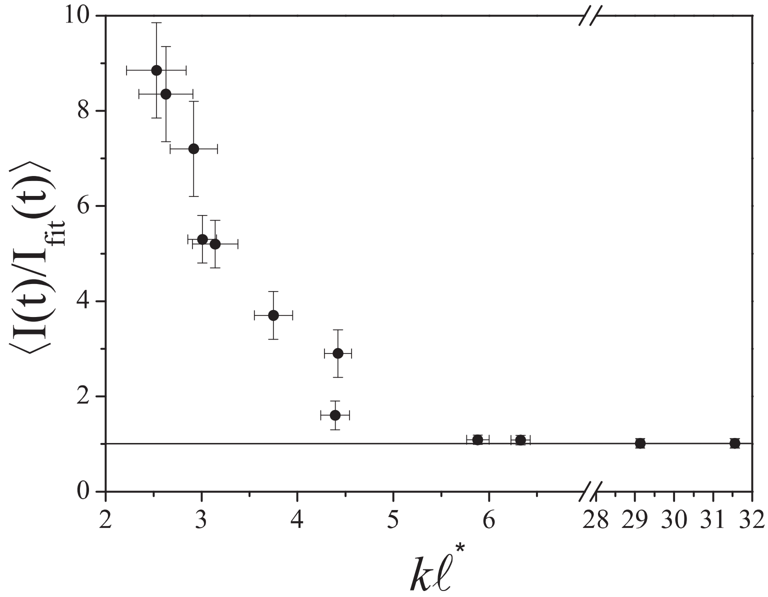

Figure 5.7: Measurements of the deviations from diffusion on several samples with different turbidity (kl^*). The deviation is quantified by taking the ratio of I(t) to the intensity of the classical fit $I_{fit}(t)$. This ratio is plotted over kl^* obtained from coherent backscattering measurements. The result is consistent with the Ioffe-Regel criterion because samples with a smaller value of kl^* show a bigger deviation to the classical fit.

5.2.2 Determination of the Critical Exponents

Given the deviations of different multiple scattering samples, which were presented in the previous section, a more detailed investigation of Anderson localization is possible, as will be presented in this section.

Considering a temporally varying diffusion coefficient to describe the critical regime of Anderson localization, one in interested in the functional behavior of $D(t)$. Since there is no theory which includes sub-diffusive behavior, near field scattering and correlations between the scattering paths, a phenomenological description which gives the possible functional form of D(t) using the concepts of diffusion theory has to be used.

Remembering that the mean square displacement of the photon-cloud is expected to come to rest for strong localization one can use the expression obtained in section 2.3 in order to connect the Diffusion coefficient with the spread of the photon-cloud,

$$\langle r^2 \rangle = D(t)t \equiv \text{const.} \tag{5.2}$$

Doing so, one ends up with a prediction for the limiting behavior of $D(t)$ in the localized state as

$$D(t) \propto \frac{1}{t}. \tag{5.3}$$

The path length distributions show that there is a certain time a photon has to travel inside a multiple scattering medium before it enters a localized state.

This path corresponds to a time where eg. 5.2 is not yet fulfilled, meaning that the photon-cloud is still spreading. Therefore the spread of the photon cloud deceases until it stops growing after t_l. The final spread of the photon cloud can be quantified by

$$L_{loc} = \sqrt{Dt_l}. \tag{5.4}$$

This means that the decrease quantified by the exponent a of $D(t) \sim t^{-a}$ cannot exceed $1/t^{a=1}$ following Berkovits and Kaveh [99, 100]. An experimental determination of the value of a allows a test of the scaling theory of Abrahams et al. [6] for $D(t)$.

As already mentioned in section 2.3 the transmitted intensity through a slab of length L is given by

$$I(t) \sim \exp\left(\frac{-t}{t_{abs}}\right) \sum_n (-1)^{n+1} n^2 \exp\left(\frac{-n^2\pi^2 Dt}{L^2}\right) \tag{5.5}$$

where t_{abs} is the absorption time. In the longtime limit one has to take into account just the first term as shown above. In order to be able to describe the measured data with diffusion theory including a time dependent diffusion coefficient one needs to take more than just the first term into account, because it describes the long time limit only. This was done by Berkovits and Kaveh [99] who obtain

$$I(t) \sim \exp\left(\frac{-t}{t_{abs}}\right) \sum_n (-1)^{n+1} \left(\frac{D(t)}{D_0}\right)^2 n^2 \exp\left(\frac{-n^2\pi^2 D(t)t}{L^2}\right) \tag{5.6}$$

with

$$D(t) = D_0 \left[\frac{t_{loc}^a}{t_{loc}^n + t^n}\right]^{a/n}. \tag{5.7}$$

The value of n has just to be large enough to ensure a fast crossover from the classical to the localizing regime. Therefore we set it to $n = 10$.

This approach is reasonable, as simulations done be Lenke et al. [101] showed such a behavior of the diffusion coefficient by calculating photon-path using a self attracting random walk. A set of simulated data is shown in Fig. 5.8 where the time dependence of the diffusion coefficient is plotted. The Diffusion coefficient stays relatively constant, until a certain time, where its value starts to decrease as $1/t$, illustrated by the dashed lines. The same behavior can be achieved by Eq. 5.7 as presented in Fig.5.9 where the inset shows the temporal behavior of the diffusion coefficient. The graph presented in Fig. 5.9a shows a time of flight distribution of a R700-sample. The theoretical curve fits the data well and provides information on the critical parameter a which is used as a free fit parameter. This parameter turned out to be $a = 1$ indicating that the photons staying inside the sample for such a long time do not increase their mean square displacement and therefore are localized. The data in Fig. 5.9b which is the same data-set as that presented in 5.5b correspond to a R902-sample which follows a fit using a critical exponent of $a = 1/3$. This intermediate regime is consistent for a scaling exponent in the

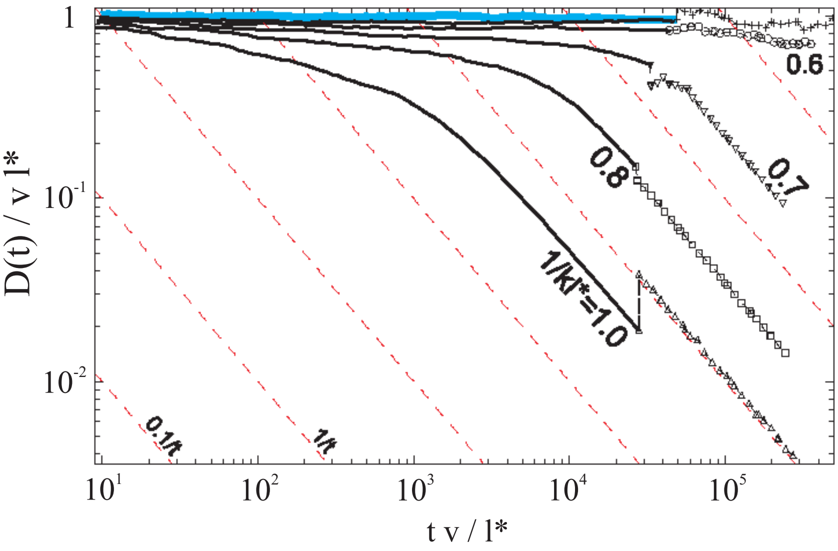

Figure 5.8: Numerical simulation performed by Lenke et al. [101] using a self attracted random walk approach. One can see a dropdown of the normalized diffusion coefficient starting at a certain time, the photons stay inside the multiple scattering medium. This qualitative behavior was used for further characterization of the time resolved transmission measurements in order to include a time dependent diffusion coefficient to diffusion theory.

critical regime [99] towards strong localization.
Analyzing all available samples allows a study of the localization exponent for different values of kl^* for the transition towards Anderson localization. This is presented in Fig. 5.10 which indicated that for a low value of kl^* the localization coefficient approaches its value of one, indicating that the diffusion came to rest in the longtime limit. It can be seen in Fig. 5.9 that the time-dependence of the diffusion coefficient is put in for a time which can be interpreted as a localization time t_{loc}. This time corresponds to a path length L_{loc}, the localization length. The parameter L_{loc} allows a more quantitative description of the critical point. For a critical exponent $a = 1$ the mean square displacement calculates as $\langle r^2 \rangle = Dt_{loc}$ which no longer increase with time. For smaller values of a the localization length is more complicated due to the finite samples, such that the localization length includes the sample thickness L.

$$L_{loc} = \sqrt{Dt_{loc}}^{\,a} L^{1-a} \tag{5.8}$$

This is presented in Fig. 5.11 where L/L_{loc} is plotted over the turbidity of the samples. One can easily see a decrease of the localization length for smaller values of kl^*. In order to obtain a value for the critical turbidity one can linear extrapolate the data points which correspond to a critical exponent of $a = 1$. The extrapolation goes to zero at a turbidity of $kl^*_c = 4.2(2)$, which can be interpreted as the critical value for the transition to strong localization. Since there are not many data points which have a critical exponent of unity, there is still an uncertainty in the value

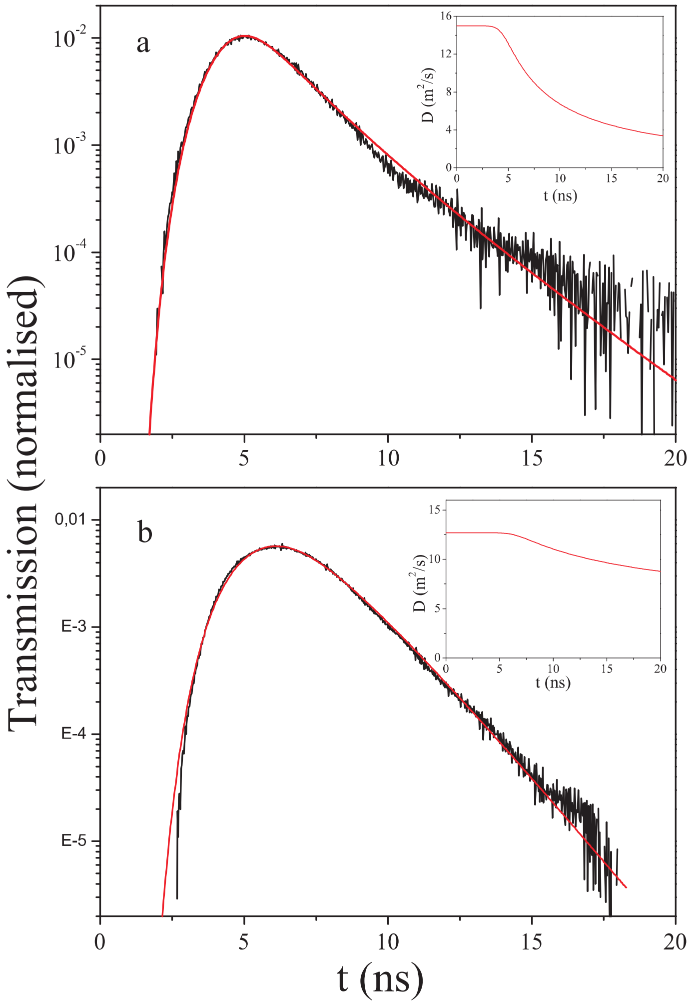

Figure 5.9: Time of flight distribution of R700 and R902-sample, already presented in Fig.5.4c/b. For R700 beyond the localization transition, the distribution can be well fitted assuming a temporarily varying diffusion coefficient as shown in the inset. The assumption of such a time-dependence of D was inspired by numerical results performed by Lenke et al. using a self attracted random walk. The R700 measurement follows a $D(t) \sim 1/t$ for times longer than the localization time t_{loc} where deviations to the classical diffusion start to occur. For R902, which is close to the localization transition the diffusion coefficient $D(t) \sim t^{-1/3}$ fits the data. This scale dependence of the diffusion coefficient is consistent with predictions for the critical regime of Anderson localization.

of kl^*_c. Further measurements on samples which have a higher turbidity would improve this value for the critical turbidity. Furthermore the linear extrapolation is chosen somewhat ad hoc since theoretical predictions are sill lacking. The obtained value of kl^*_c can be used in order to determine the critical behavior of L_{loc} at the transition to Anderson localization. Localization theory predicts that the normalized localization length diverges with a critical exponent $\nu < 1$ quantified

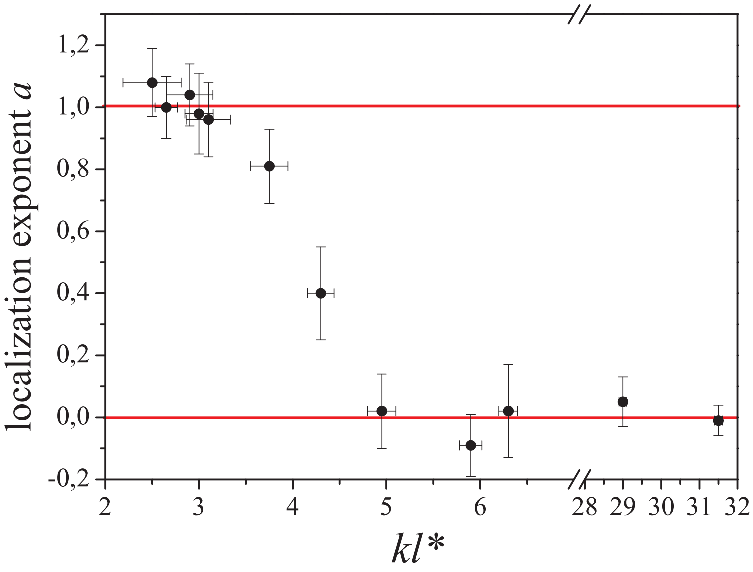

Figure 5.10: Dependence of the localization exponent a plotted against the value of kl^*. For classical samples which do not fulfill the Ioffe-Regel criterion, this parameter is zero. Below the transition, $a = 1$, which corresponds to the case where the spread of a photon-cloud come to an end approaching the localization length L_{loc}. In the critical regime the diffusion coefficient is renormalized, such that it becomes scale dependent.

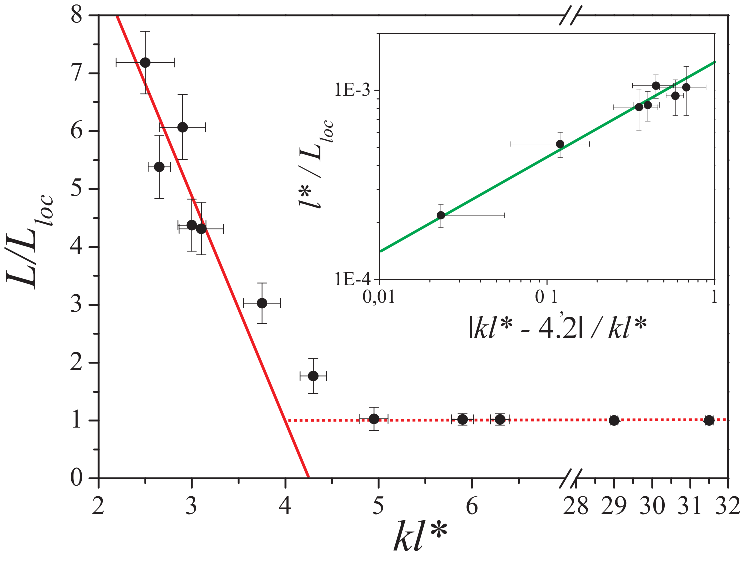

Figure 5.11: The dependence of the inverse localization length on the critical parameter kl^* normalized to the sample length. From a linear extrapolation of the datapoints with a critical exponent $a = 1$ one can obtain a critical value of $kl^*_c = 4.2(2)$. This allows a plot of the normalized localization length over the critical parameter $\frac{|kl^* - kl^*_c|}{kl^*}$ as presented in the inset. The critical exponent is thus determined to be $\nu = 0.45(10)$. The straight line in the figure indicates a exponent of $\nu = 0.5$.

by

$$\frac{l^*}{L_{loc}} \sim \left[\frac{|kl^* - kl_c^*|}{kl^*}\right]^{\nu}. \qquad (5.9)$$

This normalized l^*/L_{loc} is presented in the inset of Fig.5.11. A fit to the data points gives a value of $\nu = 0.45(10)$ which is consistent with theoretical prediction for Anderson localization where a critical exponent $\nu = 0.5$ can be obtained on the basis of a mapping of localization to the dirty XY-model [102]. The fitted exponent in Fig.5.11 is consistent with the value obtained from the inverse slope of the scaling function as presented by Abrahams et al. [6]. An estimate of the slope can be obtained from Fig.1 in [6], which yields a value of $\nu = 0.4$

5.2.3 Static Transmission

As mentioned at the beginning of this section, static transmission through a multiple scattering medium has been performed in order to prove the existence of Anderson localization. Unfortunately, the fact that absorption and localization have the same effect on the signal of static transmission means that those measurements were not capable to unequivocally prove the existence of strong localization.
Time resolved transmission measurements allow the determination of the absorption length l_a of the samples as explained in detail in the sections above. Similarly, the above fits to non classical diffusion allow a determination of the localization length L_{loc}. Now that the values of the absorption- and the localization lengths are measured, one is able to describe static transmission through a multiple scattering medium without any adjustable parameters. Measurements of the static transmission are presented in Fig. 5.12 for the most localizing sample (R700). For sample thicknesses ranging from 0.2mm to 2.5mm an exponential decay of twelve orders of magnitude can be observed. Since the absorption length is measured by time resolved transmission and the value of the transport mean free path is known from coherent backscattering, it is possible to calculate the expected decay including diffusion and absorption. This calculation corresponds to the dashed line in Fig.5.12, which lies above the measured data over the whole range of the measurements.
Including the exponential decay due to localization, quantified by the localization length L_{loc}, the theoretical curve is in very good agreement with the measured intensity. Note that the calculations were performed with values originating from different measurements on the sample, such that there are no adjustable parameters used for the theoretical curve. This provides another indication that the effect we have observed is consistent with the predictions of localization theory [28].

5.3 Faraday Effect

In order to prove the interference nature of Anderson localization of photons, time reversal symmetry has to be broken. Besides relativistic effects and inelastic scat-

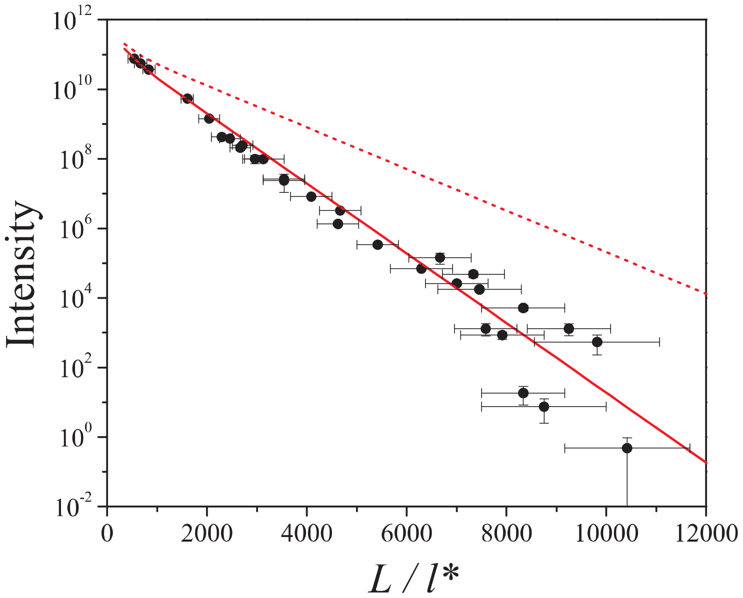

Figure 5.12: Static transmission of R700 samples as a function of the sample thickness. The transmission strongly decreases over twelve orders of magnitude within a range of L=2mm. Using the absorption length obtained from the fit to the time resolved transmission measurements one would expect the data to follow the dashed line. Including the decrease which is expected to arise from the localization length which is also determined by the time of flight measurements, the full line is obtained ,which follows the measured data-points without any adjustable parameters. The error bars correspond to slight differences in the filling fractions which lead to an uncertainty in the value of l^* of the samples.

tering, this is achievable by using the Faraday-effect. As introduced in section 2.6, the Faraday-effect in a multiple scattering medium is able to destroy the interference on time reversed paths. If this interference is the origin of the coherent backscattering enhancement this implies that enhanced backscattering can be reduced. Experiments on coherent backscattering [103] showed that this is indeed the case. In these studies, a high magnetic field (up to 23 Tesla) was required.
In this section time resolved transmission measurements on mixtures of TiO_2 and the Faraday-active CeF_3 will be presented. At the time this thesis was written, first measurements on those samples were performed, such that the presented results show a qualitative effect. Future experiments using an improved setup are expected to provide quantitative data on the Faraday-effect in this particular type of sample.

5.3.1 The Faraday Active Multiple Scattering Sample

The used samples consist of a mixture of commercially available TiO_2 and custom made CeF_3 particles. The used titania particles (R700) which were introduced in section 4.4 have a mean diameter of 249nm, whereas the CeF_3 particles are $\sim$ 10nm in diameter. Because of their small size, it is not expected that the CeF_3

particles significantly scatter the light, whose wavelength is an order of magnitude larger than the diameter of those particles. However, the mixing of the two different particles can influence the turbidity of the sample. The CeF_3 particles have a refractive index of 1.6 and fill the space between the scatterers which in turn increases the effective refractive index of the matrix, such that the value of l^* increases. Another change of the mixture with respect to pure TiO_2 is in the absorption length. Although the CeF_3 powder looks white, it does have a slightly higher amount of absorption than TiO_2 and thus affects the time resolved transmission measurements. The challenge in sample preparation is to find the right amount of added CeF_3 in order to have a high Verdet constant which leads the other sample properties unaffected.

5.3.2 Time resolved Transmission Measurements on Faraday-Active Multiple Scattering Samples

As discussed above, with all the different changes induced by the addition of CeF_3, the first thing to achieve is a sample consisting of a mixture of R700 and CeF_3 which shows nonclassical diffusion inside the experimental setup introduced in section 3. It turned out that a mass ratio of 7% CeF_3 leads to such a sample, ac can be seen in Fig. 5.13. The transmission of this sample is high enough, such that the expected count rate decrease due to the magnetic field and the fact that the detector is further away from the sample, is still acceptable for good measurements.

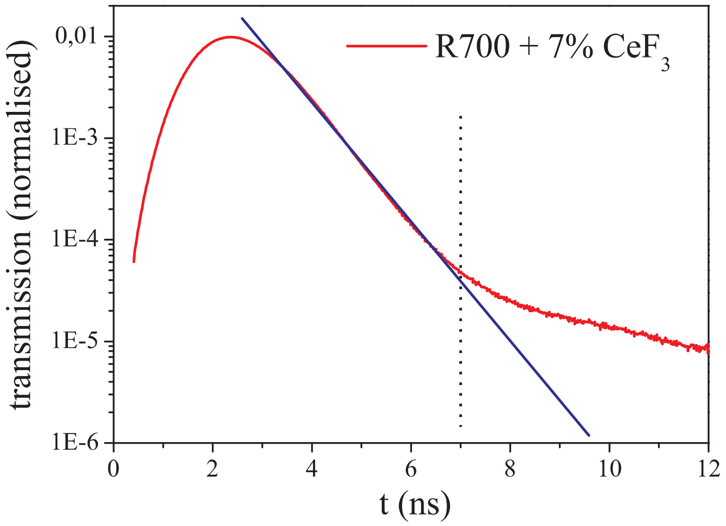

Figure 5.13: Time of flight measurement on a sample of a mixture consisting of TiO_2 particles (R700) of 4.9% CeF_3 particles by volume. This sample shows clear deviations from classical diffusion and is expected to have a Verdet constant high enough, such that the Faraday effect should be able to destroy localization.

The observed change in l^* and τ_{abs} is of the order of 10-20% and therefore the sample still shows the non-exponential tail indicative of localization. One can clearly see deviations from the exponential decay for long times as illustrated by the straight line. Given the time where the non-exponential deviation begins, one can estimate the required magnetic field that should be able to destroy the coherence on paths corresponding to this time. As introduced in section 2.6 this required magnetic field is given by

$$s_f = \frac{3}{l_f^*} \frac{1}{(2VB)^2}. \tag{5.10}$$

Since the values of the Faraday-transport l_f^* mean free path and the Verdet-constant of the sample are not known exactly, one can only get the order of magnitude of the required magnetic field out of (5.10). The value of l_f^* is expected to be about the same as the transport mean free path l^*. Therefore we estimate it as l_f^*=500nm. The Verdet-constant of CeF_3 is V=17500$\frac{\circ}{Tm}$ whereas the Faraday-effect of TiO_2 was neglected. The effective Verdet-constant of the sample is expected to be the volume-ratio of the two species used. Taking the densities of Rutile-TiO_2 (4.3 g/cm^3) and CeF_3 (6.16 g/cm^3) the volume-ration is 4.9%. With this 4.9% CeF_3 the value then would turn out to be V=855$\frac{\circ}{Tm}$. Although this is a very crude approximation it should sill give the right order of magnitude of magnetic field required to destroy the phase relation of reciprocal paths.

Given these parameters, the path length on which the localization effect starts to be observable, has to be calculated. The time, where the transmission curve presented in Fig.5.13 shows a non-exponential slope is 7ns. From this time the path length inside the sample can be calculated via $s_f = t_f c/n_G$, where n_G is the effective refractive index obtained by Garnett's[5] theory. Thus, the pathlength of a photon whose phase will be affected is $s_f \geq 1.13$m. The required magnetic field required to destroy the coherence on such a pathlength is

$$B = \sqrt{\frac{3}{l_f^* s_f}} \frac{1}{2V} = 1.35 \text{ Tesla}. \tag{5.11}$$

This magnetic field is small enough to be shielded from the photomultiplier. Given this estimate, a first measurement with a magnetic field of 1.2 Tesla was performed. Although it is a bit smaller compared to the calculated field, it is expected that deviations should be observable.

The resulting time of flight distribution is shown in Fig. 5.14, where one can clearly see that the nonclassical diffusion is reduced by the Faraday-effect inside the sample. For comparison, the reference measurement of the same sample obtained inside the magnet but without a magnetic field is plotted over the transmission at a field of 1.2 Tesla. This first measurement on the influence of the Faraday-

---

[5] The value of the effective refractive index is presented here is the Garnett's refractive index $n_G = 1.5$ corresponding to a volumefraction of 42%. However the CeF_3 particles increase this value further. This increase was estimated to be of the order of the relative mass-fraction of CeF_3. Therefore the effective refractive index was increased by 7%

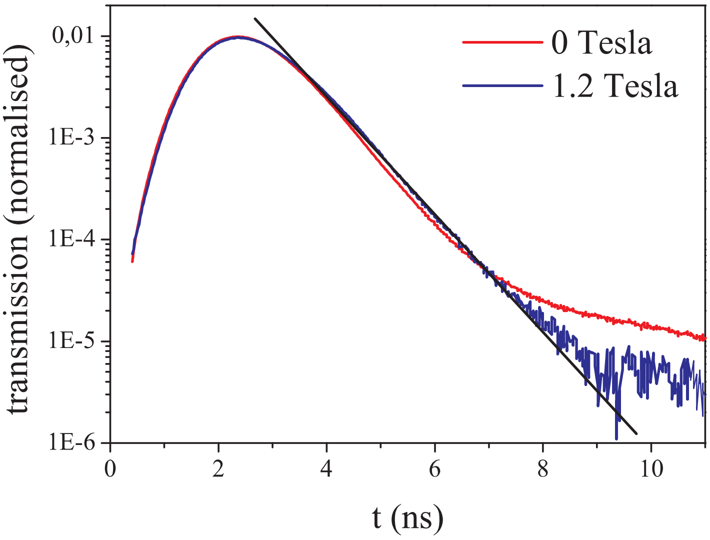

Figure 5.14: Comparison of the time of flight measurements with the sample presented above for two different magnetic fields. One can clearly observe a difference in the two transmission histograms, such that at a magnetic field of 1.2 Tesla the coherence on a path length of s_f=1.13m is destroyed. This measurement provides evidence that the concept of interference on reciprocal paths is right in order to explain Anderson localization.

effect on a strongly localizing sample provides evidence that the mechanism of Anderson localization is indeed due to constructive interference on time reversed photon-paths. The required magnetic field lies in the order of magnitude expected from an approximation using the spin-flip model. Higher fields would decrease the count rate in a way that the integration time would become higher. So the magnetic field was chosen as small as possible in order to increase the signal in respect to the noise-background of the detector.

In a next step, further measurements will be performed in order to be able to make quantitative statements on the interference of the Faraday-effect on localizing samples. For this purpose, however the setup has to be improved because at the time this experiment was planned it was not obvious that such low fields are sufficient to destroy the non-exponential tails. The stray-field at the position of the photomultiplier is high because of the geometrical proportions of the coil of the 20 Tesla magnet, which has a small gradient of the magnetic field. The future Faraday-experiments on time resolved transmission will be performed inside a magnet with a larger gradient, which is expected to reduce the stray-field at the position of the detector. Thanks to this the distance of the detector with respect to the sample can be greatly reduced, thus increasing the count rate. Another advantage will be the use of a avalanche photodiode instead of the photomultiplier which is expected to show a smaller dependence on the magnetic field. With a combination of these advantages, one expects an increase in the count rate by a factor of up to 10. Therefore the sample lengths can be increased, in order to increase the signature of localization. For these reasons, future measurements inside a magnetic field, hold much promise compared to the one shown here.

Chapter 6

Summary and Outlook

In the thesis summarized here, the goal was to provide experimental evidence for the existence of Anderson localization of visible light. The main focus was on time resolved transmission measurements, because unlike in static transmission, the effects of localization and absorption can be separated. Using these methods on samples consisting of titania particles, combining a small amount of absorption with a very high refractive index, we were able to observe a slowing down of photon transport. This slowing down can theoretically be described by a scale dependence of the diffusion coefficient, consistent with the prediction by Abrahams [6]. Systematic measurements on various samples with different particle sizes allowed us to distinguish the effect of Anderson localization from resonance scattering, where the dwell-time leads to a reduction in transport speed through the medium. However this reduced transport cannot lead to the non-exponential form of the transmission data in its long time limit.

We could also rule out several other possibilities, which were theoretically able to show such a deviation from classical diffusion of photons: Stratification, fluorescence, background illumination and several other artifacts arising from the technical setup could be ruled out as a source of such an effect.

For a smaller value of the measured transport mean free path the deviation of the longtime behavior increases, such that below a critical value of $kl^* = 4.2(2)$ the diffusion coefficient shows a 1/t behavior indicating that diffusion came to rest. We succeeded to extract a characteristic length corresponding to the localization length out of the measured transmission data. With this and the independently determined absorption length it is possible to theoretically describe the measured thickness dependence of static transmission of a sample over 12 orders of magnitude without any adjustable parameters.

Preliminary measurements of time resolved transmission inside a magnetic field show promising results of the Faraday effect in strongly localizing media. It is expected that Faraday rotation leads to a destruction of the coherence on time reversed paths, such that the signature of nonclassical diffusion vanishes. Therefore we performed time of flight measurements on a mixture of TiO_2 particles with small CeF_3-spheres with a high Verdet constant. For a mass-fraction of 7%

we were able to discover a breakdown of the non-exponential long time behavior, consistent with theoretical estimates. This measurement indicates that the nonclassical diffusion does in fact have its origin in constructive interference on reciprocal multiple light-scattering paths.

These results have to be confirmed using an improved setup. Therefore a new time of flight experiment inside a super conducting magnet with smaller geometric proportions is planned. The new setup is expected to allow an easier alignment and a higher signal to noise ratio, which will allow a clear observation of the effect.

For strongly localizing media, transmission experiments are becoming less feasible due to the exponential decay of the total transmission over the length of the medium. Therefore a time resolved reflection experiment is planned. This setup consists of a pulsed light source delivering fs-pulses, where interference of the reflected pulse and a delayed pulse will provide information on the penetration depth of the photons. It is expected that the temporal behavior of the reflection in the diffusive regime following a $t^{-3/2}$ approaches the slope of t^{-2} expected for a strong localizing medium.

Chapter 7

Zusammenfassung und Ausblick

Das Ziel der hier vorgestellten Arbeit war der experimentelle Nachweis der Existenz starker Lokalisierung von sichtbarem Licht. Hierbei galt das Hauptaugenmerk zeitaufgelösten Transmissionsmessungen. Im Gegensatz zu Messungen der statischen Transmission ist diese Methode in der Lage die Effekte der Absorption und Lokalisierung zu trennen. Flugzeitmessungen an Proben bestehend aus Titanoxid, welche eine niedrige mittlere freie Weglänge mit einem äußerst geringen Maß an Absorption vereint, erlauben uns erstmalig, eine Verlangsamung des Photonentransports zu messen. Diese Verlangsamung kann mit Hilfe der Skalenabhängigkeit des Diffusionskoeffizienten theoretisch erklärt werden. Dies ist konsistent mit den Vorhersagen von Abrahams et al. [6] für starke Lokalisierung. Systematische Messungen an einer Vielzahl von Proben, welche sich durch ihre Teilchengrößen unterscheiden, erlauben uns den Effekt der Lokalisierung von Resonanzstreuung zu unterscheiden. Hier sorgt die durch Resonanz erhöhte Verweilzeit der Photonen in einem Streuer für einen reduzierten Photonentransport durch das Medium. Jedoch stimmen unsere Daten mit der Annahme überein, dass dieser reduzierte Transport keineswegs zu einer Abweichung der zeitaufgelösten Transmissionsdaten in deren Langzeitlimes führt.

Es gelang uns verschiedene Effekte auszuschließen, die möglicherweise in der Lage sind, solch einen Effekt hervorzurufen. Zum Beispiel einen Dichtegradienten innerhalb der Probe, die Fluoreszenz des Materials wie auch Hintergrundbeleuchtung und Artefakte, welche ihren Ursprung im technischen Aufbau haben, wurden überprüft und eindeutig nicht als Quelle der gemessenen Abweichung identifiziert. Für kleinere Werte der mittleren freien Transportweglänge konnten größere Abweichungen zur klassischen Diffusion beobachtet werden, sodass der Diffusionskoeffizient eine $1/t$-Abhängigkeit unterhalb eines kritischen Wertes von $kl^* = 4.2(2)$ aufwies. Dieses Verhalten bedeutet, dass der Photonentransport zum Stillstand kommt. Es gelang uns, aus den Messungen eine charakteristische Länge, die als Lokalisierungslänge verstanden werden kann, zu extrahieren. Hiermit, und mit Hilfe der unabhängig gemessenen Absorptionslänge gelang es uns erstmalig, eine Dickenabhängigkeit der statischen Transmission eines stark lokalisierenden Mediums ohne freie Parameter über 12 Größenordnungen zu beschreiben.

Erste Messungen zeitaufgelöster Transmission innerhalb eines Magnetfeldes zeigen vielversprechende Ergebnisse bezüglich des Faraday-effekts auf stark lokalisierende Medien. Es wird erwartet, dass die Faradayrotation der Polarisation zu einer Zerstörung der Kohärenz auf zeitumkehrbaren Pfaden führt. Dies hat zur Folge, dass die Anzeichen nichtklassischer Diffusion verschwinden. Aus diesem Grund führten wir zeitaufgelöste Transmissionsexperimente an einer Mischung bestehend aus TiO_2 Teilchen und kleinen CeF_3-Kugeln, welche eine sehr hohe Verdetkonstante haben, durch. Bei einem Massenverhältnis von 7% CeF_3 waren wir in der Lage eine Abnahme des nichtexponentiellen Langzeitverhalten zu beobachten. Diese Messung ist konsistent mit den theoretischen Annahmen und erlaubt die Interpretation, dass die gemessene Abweichung der klassischen Diffusion ihren Ursprung in der Tat in konstruktiver Interferenz auf zeitumgekehrten Pfaden hat.

Diese ersten Ergebnisse müssen nun mit Hilfe eines verbesserten experimentellen Aufbaus bestätigt werden. Hierfür ist ein neues Flugzeitexperiment innerhalb eines supraleitenden Magneten, welcher kleinere Proportionen aufweist, geplant. Der Vorteil dieses neuen experimentellen Aufbaus liegt in dessen leichteren Justage und einem höheren Signal zu Rausch Verhältnis, das uns eine klare Messung des Faradayeffekts erlauben wird.

Für Studien stark lokalisierender Medien sind Experimente, die auf Transmission beruhen sehr schwer durchführbar, da das Signal exponentiell mit der Dicke des Mediums abnimmt. Aus diesem Grund ist ein Flugzeitexperiment in Reflexion geplant. Der Aufbau besteht aus einer gepulsten fs-Lichtquelle, welche über Interferenz mit einem Referenzpuls Informationen über die Eindringtiefe der Photonen liefert. Es wird erwartet, dass das zeitliche Verhalten der reflektierten Intensität im diffusiven Regime einem $t^{-3/2}$-Verlauf folgt, welcher sich an das für starke Lokalisierung erwarteten t^{-2}-Verhalten annähert.

Chapter 8

List of Publication

- Observation of the critical regime in the approach to Anderson localization of light
  M. Störzer, P. Gross, C.M. Aegerter, and G. Maret
  Phys. Rev. Lett. **96**, 063904 (2006)

- Reduced transport velocity of multiply scattered light due to resonant scattering.
  M. Störzer, C.M. Aegerter, and G. Maret
  Phys. Rev. E **73** 065602R (2006)

- Experimental determination of critical exponents in Anderson localization of light.
  C.M. Aegerter, M. Störzer, and G. Maret
  Europhys. Lett. **75** 562 (2006)

- A precise method to determine the angular distribution of backscattered light to high angles.
  P. Gross, M. Störzer, M. Clausen, C.M. Aegerter, and G. Maret
  to be submitted to Rev. Sci. Instr. (2006)

Chapter 9

Danksagung

Die wissenschaftliche Arbeit, die ich hier präsentiere, wäre nicht möglich gewesen, wenn ich keine Unterstützung von meinen Kollegen und Freunden gehabt hätte. An dieser Stelle möchte ich mich bei denen bedanken, die mir das Leben in den letzten drei Jahren erleichtert haben.
Als Erstem gebührt mein Dank meinem Doktorvater, Prof. Dr. Maret, der mich als Doktorand eingestellt hat und alle nötigen Formalitäten regelte, sodass ich mich einzig und allein auf meine Forschung konzentrieren konnte. Ich genoss während meiner Zeit an seinem Lehrstuhl ein hohes Maß an Vertrauen, was die zeitliche Planung der Experimente betraf. Zudem hatte er jederzeit ein offenes Ohr für Fragen, Ideen und Diskussionen. Er gab mir die Möglichkeit, an einem gleichermaßen herausfordernden, wie auch interessanten Experiment zu arbeiten. Mein Ex-Chef Prof. Dr. Oberthaler, der selbst am experimentellen Nachweis der Anderson Lokalisierung arbeitete, bezeichnete dieses Vorhaben damals als "high risk - high win" - Experiment. "I würd des mache, aber des muscht scho Du wissa" - nach dem ersten Gespräch mit Herrn Maret war mir klar, wo ich meine nächsten drei Jahre verbringen wollte. Obwohl ich aus dem Gebiet der Atomoptik kam, vertraute mir Herr Maret dieses Projekt an, welches anfangs ohne Betreuung angegangen werden musste.
Nach einem Jahr, indem ich mich mit Teilchen-Synthese beschäftigt hatte, wuchs die Einmann-Gruppe Störzer. Hinzu kam Christof Aegerter, den ich gern unter meine Fittiche nahm. Ein wahrer Glücksgriff, wie sich herausstellen sollte. Nach kurzer Zeit am Lehrstuhl Maret nahm Christof mich dann wiederum unter seine Fittiche und zeigte sich als sowohl wissenschaftlich als auch menschlich hervorragender Betreuer meiner Arbeit. Er verstand es, meine Motivation in die richtigen Bahnen zu leiten, und wenn diese Motivation durch Probleme, welcher Art auch immer, aufgebaut werden musste, so fand er die richtige Mischung bestehend aus "Peitsche-schwingen" und "in Ruhe lassen". Ich genoss die ungezwungene Atmosphäre in seiner "Subgroup" und freue mich, ein "Aegi" zu sein. Nach kurzer Zeit in Konstanz gelang es, dank seines wissenschaftlichen "Händle", in unseren Daten tatsächlich ein Anzeichen nichtklassischer Diffusion zu erkennen. Zu der Zeit lernte ich viel Neues über logarithmische Skalen. Beinahe alles Wissenschaftliche, was

über das Justieren von Optik hinausgeht, weiß ich von Christof. Unsere Teamarbeit, die mir sehr viel Spaß an meiner Arbeit bereitet hat, stand stets unter dem Leitspruch "...bis mr's kennat...". Ein sehr guter Leitspruch wie sich herausgestellt hatte.

Zur selben Zeit zu der Christof nach Konstanz kam, verpflichtete sich auch Peter Groß zu seinem Dienst als Diplomand an meiner Seite. Seine Aufgabe war es, die Hirngeburt eines neuartigen Rückstreuexperiments auszutragen. Zusammen mit Martin Clausen, übernahm Peter Groß den Zusammenbau des Apparates. Hierzu waren 10000 (gute) Lötstellen zu machen - somit musste der Kolben circa 15000 mal die Platinen berühren. Beiden möchte ich für ihr unermüdliches Engagement danken. Ihre Mühe hat sich gelohnt, denn dadurch besitzt die Gruppe Maret die breitesten Konen der ganzen weiten Welt. Ebenfalls Christian Ortholf möchte ich danken, dass wir dieses Spielzeug unter seiner kompetenten Aufsicht in seiner Werkstatt aufbauen durften.

Stefanie Eiden und Johanna Widoniak, wie auch Ina Seufert, die mich in ihrem Labor Chemiker spielen ließen, danke ich ebenfalls herzlich. Ihre Geduld in der Zusammenarbeit mit einem Physiker wusste ich sehr zu schätzen. Den Hiwis in der Chemie, Christiane und Monika möchte ich ebenfalls danken. Schade, dass ihre unermüdlichen Kochansätze letztendlich nicht die vorhergesagten Erfolge zeigten - wäre es vom Aufwand und Engagement abhängig gewesen, den sie alle fünf zusammen getrieben haben, hätten wir sicherlich die trübsten Proben auf dem Planeten gehabt.

Den guten Geistern Doris und Sabine möchte ich danken, dass sie mir die Bürokratie, so weit es ihnen möglich war, fern gehalten haben. Trotz der vielen wichtigen Arbeiten fand sich immer Zeit für Fragen bis hin zur Buchung von ganzen Dienstreisen. Vielen Dank dafür, ich werde den Service vermissen. Er wird dies bereits gewohnt sein, aber ein weiterer Dank gebührt Stefan Hahn, der nach meinem Umzug in den 10. Stock immer noch als Berater in technischen Fragen herhalten musste. Seine Kenntnis über: "Wo bekommt man was schneller, billiger, besser... her" halfen mir stets weiter - besonders, wenn es schnell und unkompliziert über die Bühne gehen sollte.

Ich musste zum Glück nicht allein im Labor arbeiten. Schon bei unserem ersten treffen - wusste ich schon, dass ein Labor mit Gerd zu teilen ein Spaß werden würde. So war es! Ich kenne keinen, der so schnell in Deckung gehen kann, wenn ein Laserstrahl durch den Raum schießt (ich hoffe, dies hielt sich in Grenzen). Es ist schön, wenn man Gesprächsthemen, Musikgeschmack und gleichzeitig den Arbeitsplatz teilt. Den restlichen Kollegen (in Reihenfolge gemäß der Hompage - copy und paste sei Dank): Thomas Gisler, Franck Jaillon, Jun Li, Alexander Andr, Wolfgang Bührer, Gregor Dietsche, Patrick Dillmann, Florian Ebert, Susanne Fiebig, Corinna Maaß, Kirill Sandomirski, Andrej Grimm, Nathan Isert, Ralf Weissenborn, Christof Eisenmann, Urs Gasser, Peter Keim, Michael Reichert und meinem "Roomie" Stephen Martin möchte ich für drei schöne Jahre danken. Sie, zusammen mit den Leuten der Arbeitsgruppen Schatz und Scheer, haben alle zu einer gleichermaßen produktiven, unterhaltsamen und entspannten Arbeitsat-

mosphäre beigetragen.
Da meine Freundin Nicole Wild nicht namentlich erwähnt werden will, werde ich ihrem Wunsch entsprechen, und mich an anderer Stelle bei ihr bedanken, dass sie in den "hellen" wie auch "dunkleren" Stunden der letzten und hoffentlich kommenden Jahre an meiner Seite war und sein wird.

Bibliography

[1] P.E. Wolf and G. Maret, Phys. Rev. Lett. **55**, 2696 (1985).

[2] M.P. van Albada and A. Lagedijk, Phys. Rev. Lett. **55**, 2692 (1985).

[3] G. Maret, P. E. Wolf, Z. Phys. **65**, 409 (1987).

[4] D. J. Pine, D. A. Weitz, P. M. Chaikin, and E. Herbolzheimer, Phys. Rev. Lett. **60**, 1134 (1988).

[5] A. F. Ioffe, A. R. Regel, Progress in Semiconductors **4**, 237 (1960).

[6] E. Abrahams, P. W. Anderson, D. C. Licciardello, T. V. Ramakrishnan, Phys. Rev. Lett. **42**, 673 (1979).

[7] H. C. van de Hulst, Volume1/2, Academic Press, New York (1980).

[8] C. F. Bohren, D. R. Huffman, Wiley Science Paperback Series, (1998).

[9] Ed. D. W. Schuerman, Plenum, New York (1979).

[10] P. W. Barber, S. C. Hill, Word Scientific, London (1990).

[11] G. Mie, Ann. d. Physik **25**, 377 (1908).

[12] P. Debye, Ann. d. Physik **30**, 57 (1909).

[13] M. Born, E. Wolf, Pergamon Press Ltd., Oxford (sixth edition 1980).

[14] ”LightLab: Far Field Mie Scattering” (Valley. Scientific, 1998).

[15] R. Klein, Int. School of Physics ”E. Fermi”, IOS Press Amsterdam, 394 (1997).

[16] J. K. Percus, G. Yevic, J. Phys. Rev., **110**,1 (1958).

[17] J. D. Jackson, (1999).

[18] E. N. Economou, Springer, Berlin (1990).

[19] R. Lenke, G. Maret, Gordon and Breach Scientific (2000).

[20] D. Bicout and G. Maret, Physca A, **210**(1-2),87 (1994)

[21] M. Heckmeier and G. Maret, J. Opt. Soc. Am. A 14(1):185 (1997).

[22] P. E. Wolf, G. Maret, R. Maynard, J. Phys. France **49**,1 63 (1988).

[23] E. Akkermanns, P. E. Wolf, R. Maynard, G. Maret, J. Phys. France **49**,1 77 (1988).

[24] E. Amic, J. M. Luck, Th. M. Nieuwenhuizen, J. Phys. A, **29**, 4915 (1996).

[25] J. X. Zuh, D. J. Pine, D. A. Weitz, Phys. Rev. A **44**, 3948 (1991).

[26] C. M. Soukoulis, S. Datta, Phys. Rev. B **49**, 3800 (1994).

[27] P. W. Anderson, Phys. Rev. **109**, 1492 (1958).

[28] P. W. Anderson, Pilosophical Magazine B **52**, 505 (1985).

[29] D. C. Licciardello, D. J. Thouless, Phys. Rev. Lett. **35**, 1475 (1975).

[30] B. A. van Tiggelen, Phys. Rev. Lett. **84**, 4333 (2000).

[31] S. Skipetrov, B. A. van Tiggelen, Phys. Rev. Lett. **92**, 113901 (2004).

[32] S. Skipetrov, B. A. van Tiggelen, Phys. Rev. Lett. **96**, 043902 (2006).

[33] D. Vollhardt, P. Wölfle, Phys. Rev. B, **22**, 4666 (1980).

[34] D. Vollhardt, P. Wölfle, Elsevier Science, Amsterdam (1992).

[35] F. C. Mackintosh, S. John, Phys. Rev. B, **37**, 4 1884 (1988).

[36] A. A. Golubentsev, Sov. Phys. JETP **59**, 1 26 (1984).

[37] F. C. Mackintosh, J. X. Zhu, D. J. Pine, D. A. Weitz, Phys. Rev. B, **40**, 9345 (1989).

[38] F. C. Mackintosh, S. John, Phys. Rev. B, **40**, 2383 (1989).

[39] R. Lenke, G. Maret, Physica Scripta, **49** 605 (1993).

[40] R. Lenke, Dissertation, Universit*é* Joseph Fourier Grenoble (1992).

[41] D.S. Wiersma, P. Bartolini, A. Lagendijk and R. Righini, Nature **390**, 671 (1997).

[42] B. A. van Tiggelen, A. Lagendijk, and D. S. Wiersma, Phys. Rev. Lett. **84**, 4333 (2000).

[43] R. Tweer, PhD thesis, Fachbereich Physik Universität Konstanz, (2002).

[44] R. Lenke, R. Tweer, and G Maret, J. Opt. A **4**, 293 (2002).

[45] D.S. Wiersma, M.P. van Albada, and A. Lagendijk, Rev. Sci. Instr. **66**, 5473 (1995).

[46] P. Gross, Diploma Thesis, University of Konstanz, unpublished (2005).

[47] M. Clausen, private communications (2005).

[48] G.H. Watson, P.A. Fleury, and S.L. McCall, Phys. Rev. Lett. **58**, 945 (1987).

[49] J.M. Drake and A.Z. Genack, Phys. Rev. Lett. **63**, 259 (1989).

[50] A. Einstein, Annalen der Physik, **17**, 549 (1905).

[51] S. Fraden, G. Maret, Phys. Rev. Lett. **65**, 519 (1990).

[52] J. C. M. Garnett, Philo. Tans. R. Soc. **A203**, 385 (1904).

[53] K. Busch, C. M. Soukoulis, E. N. Economou, Phys. Rev. B **50**, 93 (1994).

[54] K. Busch, PhD thesis, Fakultät für Physik, Universität Karlsruhe, (1996).

[55] K. Busch, C. M. Soukoulis, Phys. Rev. B **54**, 893 (1996).

[56] B. J. Berne, R. Pecora, Robert E. Krieger Publishing Company, Malabar Florida, (1990).

[57] G. Bryant, S. Martin, A. Budi, W. van Megen, Langmuir **19**, 616 (2002).

[58] E. A. Barringer, H. K. Bowen, Communications of the American Ceramic Society, **199**, (1982).

[59] J. L. Look, G. H. Bogush, C. F. Zukoski, Faraday Discuss. Chem. Soc., **90**, 345 (1990).

[60] J. L. Look, C. F. Zukoski, Journal of Colloid and Interface Science, **153**, 461 (1992).

[61] T. E. Mates, T. A. Ring, Colloid and Surfaces **24**, 399 (1987).

[62] J. H. Jean, T. A. Ring, Langmuir **2**, 251 (1986).

[63] J. H. Jean, T. A. Ring, British Ceramic Proceedings **38**, 11 (1986).

[64] J. H. Jean, T. A. Ring, Colloid and Surfaces **29**, 273 (1988).

[65] J. Widoniak, Diploma Thesis, Universität Konstanz (2002).

[66] J. Widoniak, S. Eiden-Assmann, G. Maret, Chemistry of Materials **16**, 6 (2004).

[67] X. Jiang, T. Herricks, Y. Xia, Adv. Mater. **15**, 1205 (2003).

[68] J. Widoniak, PhD Thesis, Universität Konstanz (2005).

[69] W. P. Hsu, R. Yu, E. Matijevic, J. of Colloid and Ineterface Sci., **156**, 56 (1993).

[70] W. Stoeber, A. Fink, E. Bohn, Journal of Colloid and Interface Science **26**, 62 (1968).

[71] S. Eiden and G. Maret, Journal of Colloid and Interface Science **250**, 281 (2002).

[72] S. Eiden, Habilitaionsschrift, Universität Konstanz (2003).

[73] E. P. Wigner ,Phys. Rev. **98**, 145 (1955).

[74] L. V. Hau, S. E. Harris, Z. Dutton, C. H. Behroozi, Nature (London) **397**, 594 (1999).

[75] G. Labeyrie, E. Vaujour, C. A. Müller, D. Delande, C. Miniatura, D. Wilkowski, and R. Kaiser, Phys. Rev. Lett. **91**, 223904 (2004).

[76] M. L. Gorodetsky, A. A. Savchenkov, and V. S. Ilchenko, Optics Letters **21**, 453 (1996).

[77] Y. Yamamoto, and R. E. Slusher, Optical processes in microcavities, Phys. Today **46**, 66 (1993).

[78] J. C. Knight, N. Dubreuil, V. Sandoghdar, J. Hare, V. Lefevrè-Seguin, J. M. Raimond and S. Haroche, Optics Letters **21** 698 (1996).

[79] V. Sandoghdar, F. Treussart, J. Hare, V. Lefèvre-Seguin, J.-M. Raimond, and S. Haroche, Phys. Rev. A **54**, R1777 (1996).

[80] F. Vollmer, D. Braun, A. Libchaber, M. Khoshsima, I. Teraoka, and S. Arnold, Appl. Phys. Lett. **80**, 4057 (2002).

[81] H. Gersen, T. J. Karle, R. J. P. Engelen, W. Bogaerts, J. P. Korterik, N. F. van Hulst, T. F. Krauss, and L. Kuipers, Phys. Rev. Lett. **94**, 073903 (2005).

[82] S. John, Phys. Rev. Lett. **58**, 2486 (1987).

[83] Y. Akahane, T. Asano, B. S. Song, S. Noda, Nature **425** 944 (2003).

[84] M.P. van Albada, B. A. van Tiggelen, A. Lagendijk, and A. Tip, Phys. Rev. Lett **66**, 3132 (1991).

[85] B. A. van Tiggelen, PhD thesis, Univ. of Amsterdam (1992).

[86] A. Lagendijk and B.A. van Tiggelen, Phys. Rep. **270**, 143 (1996).

[87] S. Fraden, and G. Maret, Phys. Rev. Lett. **65**, 512 (1990).

[88] B. L. Altshuler, P. A. Lee, R. A. Webb, Eds, North-Holland, Amsterdam (1991).

[89] F. J. P. Schuurmans, M. Megens, D. Vanmaekelbergh, and A. Lagendijk, Phys. Rev. Lett. **83**, 2183 (1999).

[90] P. M. Johnson, A. Imhof, B. P. J. Bret, J. Gomez Rivas, and A. Lagendijk, Phys. Rev. E **68**, 016604 (2003).

[91] J. Gómez Rivas, R. Sprik, and A. Lagendijk, Phys. Rev. E **62**, R4540 (2000).

[92] F. Scheffold, R. Lenke, R. Tweer and G. Maret, Nature (London) **398**, 206 (1999).

[93] D.S. Wiersma et al., reply Nature (London) **398**, 207 (1999).

[94] A.A. Chabanov, M. Stoytchev, and A.Z. Genack, Nature (London) **404**, 850 (2000).

[95] A.A. Chabanov and A.Z. Genack, Phys. Rev. Lett. **87**, 153901 (2001).

[96] A.A. Chabanov, Z.Q. Zhang, and A.Z. Genack, Phys. Rev. Lett. **90**, 203903 (2003).

[97] S.E. Skipetrov and B.A. van Tiggelen, Phys. Rev. Lett. **92**, 113901 (2004).

[98] S. K. Cheung et al., Phys. Rev. Lett. **92**, 173902 (2004).

[99] R. Berkovitz and M. Kaveh, J. Phys. C: Cond. Mat. **2**, 307 (1990).

[100] R. Berkovitz and M. Kaveh, Phys. Rev. B **36**, 9322 (1987).

[101] R. Lenke, R. Tweer, and G. Maret, Europ. Phys. J. B **26**, 235 (2002).

[102] H. G. Schuster, Z. Phys. **31**, 99 (1978).

[103] F. Erbacher, R. Lenke and G. Maret, Europhys. Lett. **21**, 551 (1993).